Red Blood Cell Aggregation Characterization

Using Norland Optical Adhesive Microfluidic Chips for a Reduction in Compliance

by

Curtis James Karns Armstrong

Thesis submitted to the University of Ottawa

In partial Fulfillment of the requirements for

M.A.Sc. Degree in

Biomedical Engineering

Ottawa-Carleton Institute of Biomedical Engineering

Faculty of Engineering

University of Ottawa

Acknowledgements

I would like to thank every person who played a role in helping me to complete this project and make it a reality. To start, I would like to extend a sincere thank you to the members of the University of Ottawa, Faculty of Engineering, for their expertise supporting my project and my education. An enormous thank you to my supervisor Dr. Marianne Fenech, for her countless hours spent devoted to supporting this project. Thanks to her, I have had so many priceless experiences and opportunities that I cherish and will forever be grateful for. She is a mentor and a dear friend. A heartfelt thank you to the individual members of Dr. Fenech's Laboratory group; special thanks to Andy Vinh Le for his innumerable hours of insight, encouragement and knowledge that helped me to complete this research. A sincere thank you to Nikko Lee-Yow, Erfan Niazi, and Rym Mehri for all their help and contributions including technical expertise in microfluidic techniques, image processing, microfluidic fabrication and experimental procedures.

I would like to express my appreciation and gratitude to Dr. Emilie Franceschini and the members of her lab in Marseille (The Laboratoire de Mécanique et d'Acoustique (LMA, UMR 7031)); Eric Debieu and Lenin Chinchilla for all of their guidance and contributions to this project, especially in the fields of quantitative ultrasound techniques and ultrasound backscattering. I would also like to thank Dr. Manouk Abkarian and the team at the lab in Montpellier for all their help and expertise in microfluidic experimentation and fabrication. A special thanks to Viviana Claveria for her many long days spent helping me in the laboratory.

This work was funded by the National Science and Engineering Research Council of Canada (#RGPIN-2015-06188). This work was also supported by the Canada Foundation for Innovation (#31112), the Faculty of Engineering International Experience Scholarship at the University of Ottawa.

Lastly, I would like to thank my family for their continued support throughout this journey. They have always been a beacon of undying support. In particular, I would like to thank my dad (Dave), my sisters (Courtney and Brittany), my partner and best friend (Kyla), and our dog (Jax). A special thank you goes out to my mother (Kim), for making me the person I am today.

Statement of Ethics

The research conducted involving human subjects was done with the approval of the ethics committee of the University of Ottawa (H-03-19-3441).

Abstract

Abstract **-** The presence of red blood cell (RBC) aggregation is confirmed to be a rheological phenomenon implicating abnormal physiological conditions *in vivo*. However, there is presently no existing technology able to analyze, characterize and detect aggregation *in vivo*. The Laboratoire de Mécanique et d'Acoustique (LMA, UMR 7031), Centre National de la Recherche Scientifique (CNRS) at Aix-Marseille Universite (AMU) is developing a technology to measure blood aggregation *in vivo* using ultrasound backscattering techniques. In doing so it aims to allow disease prevention and disease recognition. The methodology developed at LMA is currently being compared to previous methodologies used to quantify RBC aggregation. Further study is needed to compare the methodologies used in LMA to microscopic imaging techniques, which are considered the gold standard in aggregation characterization. This thesis focuses on the development of a microfluidic device dedicated to the visualization of RBC aggregation. The device is capable of low compliance to ensure repeatability of the flow rate, with good optical clarity. The device's co-flow properties and capabilities were tested and analyzed to ensure a proper comparison of methodologies could be conducted. Once completed, the incorporation of an ultrasound transducer to the setup, will be done in France to directly compare the methodologies developed by LMA and confirm the models derived by Franceschini et al. In order to develop the microfluidic chip, this thesis considers an overview of the methodology for characterizing RBC aggregation, the fabrication and compliant verification of a novel Norland Optical Adhesive microfluidic chip, and the shear rate calibration of the microfluidic device using Dextran 70 and Dextran 500. The NOA63 microfluidic device was calibrated to flow factors based on a shearing flow ratio of 25:1. The Norland Optical Adhesive microfluidic device had a much lower level of compliance in comparison to the gold standard of PDMS. The NOA63 device was found to be 51% less compliant than its counter part of PDMS. The device was calibrated to control shear rates from around $60s^{-1}$ to $0.01s^{-1}$. Multiple concentrations of Dextran 70 and Dextran 500 in human blood samples at 10% hematocrit were tested to characterize the shear rate in the blood layer. Aggregates were

found to align themselves parallel to the flow and were observed to haven anisotropic shapes. All results from this thesis are being used to support the development of an ultrasound device capable of measuring blood aggregation *in vivo*.

Keywords: red blood cell aggregation, erythrocytes, NOA63, aggregation characterization, microfluidic device, shear rate, ultrasound backscattering, μPIV, blood.

Table of Contents

List of Tables

List of Figures

List of Symbols

a	Semi-minor axis of ellipse [µm]
a	Characteristic length in micro-channel simulation
a_c	Normalizing value for size of semi-minor axis
b	Semi-major axis of ellipse [µm]
BSC_{EMTSFM}	Backscatter coefficient calculated using the EMTSFM
C	Compliance of material
$C_{x,y}$	Cross correlation function
CF	The compliance factor
CO_2	Carbon di-oxide gas
dt	The time between two frames [µs]
$I_1(x)$	Image intensity of frame 1
$I_2(x)$	Image intensity of frame 2
n_{ag}	number density of aggregates in relation to the effective volume fraction of aggregates
O_2	Oxygen gas
p_0	Initial pressure
$p_{z,\varphi}(x)$	The Gamma distribution PDF
Q	Flow rate [µl/hr]
Q_c	Rate of storage of the system [µl/hr]
Q_{in}	inflow to the system [µl/hr]
Q_{out}	Outflow to the system [µl/hr]
R_h	The hydrodynamic resistance
R_s	The system resistance
R(s)	the image displacement
S_{ag}	the structure factor
u	Velocity of the fluid
Y_{int}	PBS interface
Y_{wall}	Interface between blood layer and the wall

z	Shape Parameter (Gamma distribution)
Γ	Gamma function
$\dot{\gamma}$	Shear rate [s^{-1}]
Δp	Change in pressure
θ	Orientation Angle
λ	Wavelength [nm]
λ_{abs}	Absorption wavelength of fluorescent particle [nm]
$\lambda_{emission}$	Emission wavelength of fluorescent particle [nm]
μ	Mean (Gamma distribution)
σ_{ag}	the backscattering cross section of an effective single sphere
τ	Characteristic time [s]
φ	Scale Parameter (Gamma distribution)

List of Acronyms

AMU	Aix-Marseille Université
BSC	Backscatter Coefficient
CCD	Charged-Coupled Device
CFL	Cell Free Layer
CNRS	Centre National de la Recherche Scientifique
DOC	Depth of Correlation
DOF	Depth of Field
EDTA	Ethyleneiaminetetraacetic
EMT	Effective Medium Theory
EMTLMA	Effective Medium Theory and Local Monodisperse Approximation
EMTSFM	Effective Medium Theory and the Structure Factor Model
ESR	Erythrocyte Sedimentation Rate
GM	Gaussian Model
HS	High Speed
JASA	the Journal of Acoustical Society of America
LMA	Laboratoire de Mécanique et d'Acoustique
LT	Light Transmission
MAI	Microscopic Aggregation Index
NOA	Norland Optical Adhesive
PDF	Probability Density Function
PDMS	Polydimethylsiloxane
PFOTS	Trichloro (1H 1H 2H 2H-perfluorooctyl) Silane
PGMEA	Propylene Glycol Methyl Ether Acetate
PIV	Particle Image Velocimetry
RBC	Red Blood Cell
RF	Radio Frequency
SFM	Structure Factor Model
SFSE	Structure Factor Size Estimator
STD	Standard Deviation

UB	Ultrasound Backscatter
UV	Ultraviolet
WBC	White Blood Cell
ZSR	Zeta Sedimentation Ratio
2D	Two Dimensional
3D	Three Dimensional
µPIV	Micro Particle Image Velocimetry

Chapter 1

1 Introduction

This chapter introduces the motivation for the research conducted in this thesis, the thesis topic and summarizes the background information in the form of a literature review. It also outlines the research goals of this thesis.

1.1 Research Motivation

Blood is a critical component of biological life. The composition of blood can be broken down into three components: red blood cells (RBC) or erythrocytes, white blood cells (WBC) or leukocytes, and blood plasma (consisting of suspended platelets). Blood is made up of around 45% RBCs, 1% WBCs, and 55% plasma [1]. It is responsible for the transportation and delivery of nutrients and oxygen throughout the body, as well as the removal of carbon dioxide. Understanding blood behaviour throughout the human body is of great interest to many researchers as it would allow insight into many diseases as well as the basis of how the human body functions [2]–[6].

Hemorheology is the study of blood and its flow properties. A big factor in understanding blood flow mechanics is the understanding of the flow properties surrounding RBCs. Rheological studies of blood focus on RBCs and their impact on the flow properties. Due to the behaviour of RBCs, blood can be classified as a non-Newtonian fluid. This makes blood quite challenging to study. Its non-Newtonian properties stem from the aggregation of RBCs in low shear flow environments, and the deformation of RBCs whilst adapting to varying vessel dimensions and shear environments. Figure 1-1 clearly depicts the aggregation phenomena of RBCs.

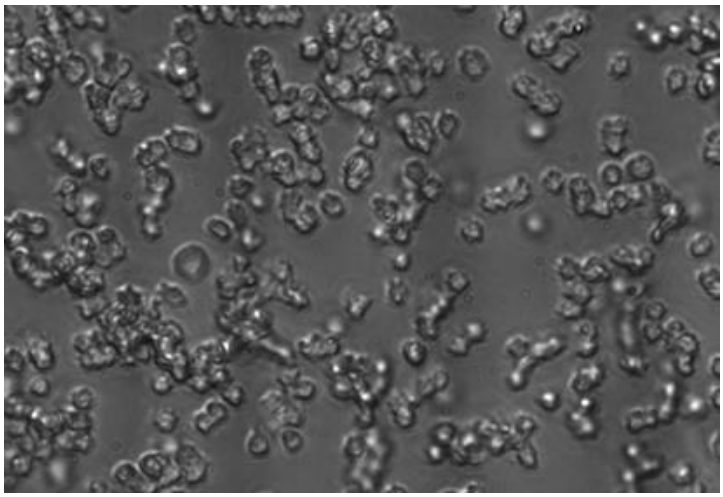

Figure 1-1: *Human RBC aggregates at 10% hematocrit, in vitro aggregation induced by dextran 70 (3g/100ml concentration).*

The aggregation phenomenon seen in blood (RBCs) is not fully understood, making it a major topic of hemorheological studies. Although it is not known definitively what causes RBCs to aggregate, it is known that aggregation of RBCs occurs in a very low shear flow. They subsequently disaggregate under shear rates varying from 20 to 40 s^{-1} [7]–[9]. It is also recognized that the appearance of aggregates coincides with some hemorheological disorders that could lead to microvascular dysfunctions and venous thrombosis [1]. This emphasizes the need to study and understand aggregation in RBCs.

Some studies have looked into the relationship between aggregation and human disease [10]–[14]. Since the presence of aggregation is confirmed to be a rheological phenomenon implicating abnormal physiological conditions *in vivo*, it can be considered important to analyze, characterize and detect aggregation *in vivo*. In doing so it aims to allow disease prevention and disease recognition.

Promising studies at Laboratoire de Mécanique et d'Acoustique (LMA, UMR 7031), Centre National de la Recherche Scientifique (CNRS) at Aix-Marseille Université (AMU) have looked into measuring blood aggregation *in vivo* using ultrasound backscattering techniques. The methodology developed at LMA is currently being evaluated against previous methodologies used to quantify RBC aggregation. Further study is needed to compare the methodologies used in LMA to those of microscopic imaging techniques which are considered the gold standard in aggregation characterization. To do so a microfluidic device capable of

low compliance, in order to get a predictable flow rate, with good optical clarity needs to be developed. The device co-flow properties and capabilities would need to be tested and analyzed to ensure a proper comparison of methodologies could be conducted. Finally, the incorporation of an ultrasound transducer to the setup would be necessary to directly compare the methodologies developed by LMA and confirm the models derived by Franceschini et al [15].

1.2 Literature Review

In this section, a detailed background into relevant research from the fields of hemorheology, microfluidics, image processing, Particle Image Velocimetry (PIV), and ultrasound backscattering techniques are presented. This is done to highlight gaps in the literature and provide motivation for this thesis.

1.2.1 Hemorheology

Hemorheology is the study of blood, its components and its flow properties. Blood itself is comprised of three main elements. These include RBCs (also called erythrocytes), WBC (also called leukocytes), and platelets (or thrombocytes). These elements are suspended in a non-Newtonian fluid called plasma. Blood, with all its components, acts as a non-Newtonian fluid. This is due to the membrane mechanics and deformation characteristics of RBCs.

1.2.1.1 RBC Shape and Function

When healthy, RBCs have a bi-concave shape in the form of discs which can be seen in Figure 1-2 [16], [17]. The diameter is around 7-8um on average, with a thickness of around 2um. The surface of the cell membrane is around 140μm^2, with a cell volume of 90μm^3 [18]–[20]. RBCs have a large surface area to volume ratio. This is to increase the transfer of resources and waste to and from the cell. The main function of RBCs however, is the transfer of oxygen (O_2) throughout the body, while simultaneously removing carbon dioxide (CO_2) from the body. This is done by utilizing the pigment haemoglobin, which can bind four oxygen molecules creating Oxyhaemoglobin. This transformation occurs in the lungs, from

there, the heart pumps the blood through the circulatory system. The RBCs then deliver the oxygen to different areas of the body, whilst retrieving CO_2 molecules. Since RBCs do not need to consume the O_2, the RBCs are able to maintain a bi-concave shape with the large surface to volume ratio [20]–[24]. The ratio provides a more efficient diffusion of O_2. Once the O_2 has been delivered, CO_2 can be carried by the RBCs. For example the CO_2 can bind to the haemoglobin of the RBC forming carbaminohaemoglobin (around 10% of CO_2 transfer), it can dissolve directly into the plasma (around 5% of all CO_2 transfer), or it can diffuse into the RBC and be carried as bicarbonate ions (around 85% of all CO_2 transfer) [21]–[23].

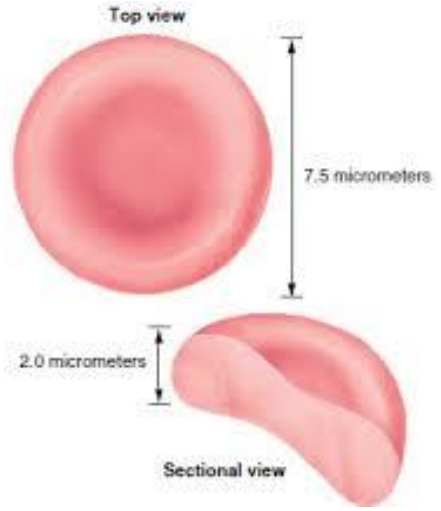

Figure 1-2: *Dimensions of human RBCs [16], [17].*

The life span of an RBC is around 115 days. Throughout this time the RBC will perform its main functions and then be consumed by macrophages within the blood. The iron (responsible for the red colour of RBCs) leftover is then used by the bone marrow to generate new RBCs through a process called erythropoiesis.

1.2.1.2 RBC Deformation

Due to the function of RBCs they need to travel through all areas of the body using the existing circulatory system. This means the RBC needs to deform to fit into vessels as small as 5-10um in diameter [18]. They can accomplish this feat thanks to their bi-concave shape and their strong, yet flexible, cell membrane. The bi-concave shape permits the cells to bend and deform, while the cell membrane is strong enough and elastic enough to resist tears or rupture. The cell membrane is composed of a lipid bi-layer,

transmembrane proteins, and a cytoskeletal network. The lipid bilayer is semipermeable and incompressible. It separates the components from within the cell from the extracellular medium. The transmembrane proteins exist in the bilayer, while the cytoskeletal network (the inner most layer) gives the cell its flexibility and strength [25], [26]. The cytoskeletal network is an irregular hexagonal lattice composed of spectrin protein molecules, which are tied together with actin protein molecules. These proteins give the skeletal structure its elasticity as well as its strength. The RBC membrane is recorded to be 100 times more elastic than latex of the same thickness [27]. At the same time the membrane is stronger than steel, in terms of resistance, as a normal RBC can deform linearly up to 250% [27]. The membrane has also been found to have viscoelastic properties. The surface viscosity of RBC membranes is in the order of magnitude of 10^{-4} dyn*s/cm (10^{-4} Pa*s) [28], [29].

1.2.2 Aggregation

Aggregation is a phenomenon that occurs in blood under appropriate low shear conditions. These aggregates consist of multiple RBCs stacked on top of each other. Each stack is called a rouleau (with rouleaux being plural). Sizing of aggregates can be quantified based on the number of RBCs present in the aggregate in question. The rouleaux can form three dimensional aggregates as well, thus creating larger aggregates with more complex structures. It is important to note the difference between RBC aggregation and blood coagulation. Blood coagulation occurs when the plasma protein fibrinogen forms a network of strands that can encapsulate blood constituents, including RBCs. Coagulation can be triggered when the body undergoes an injury as its formation helps to slow down blood loss [1], [18]. Although fibrinogen plays a role in RBC aggregation, it remains soluble which results in the reversible nature of RBC aggregation. Aggregation can occur *in vivo* due to pathological and physiological conditions. This includes physiological conditions such as inflammation or infections, as well as various pathological diseases including (not limited to) hypertension, atherosclerosis, stroke and diabetes. The rate of aggregation, defined as aggregability, in normal conditions is an area of study that is of much interest to the field. Aggregability can vary *in vivo*, not just for pathological conditions, but also for conditions such as age,

gender, and pregnancy [1]. Abnormally large amounts of aggregation are defined as hyper-aggregation and are consistent in various pathological conditions. With all these factors affecting aggregation, quantifying aggregation in terms of size, aggregability, and orientation could help to understand the function of aggregation at a clinical level.

Aggregation has been studied as early as the 1920's. Robin Fahraeus first described aggregation when studying blood sedimentation. From his work he was able to determine that the varying degree of aggregation determined the sedimentation rate [30]. Fahraeus' work allowed a clear distinction between RBC aggregation in healthy and diseased individuals [30]. His work focused on stationary RBC samples. Other researchers, such as Melvin Knisley, attempted to study blood aggregation *in vivo* under normal flow conditions [31], [32]. These studies found that aggregation, in capillary vessels, does not occur in healthy conditions. His team found that RBCs flowed as individual cells *in vivo*. He did, however, find that aggregation was more prominent in pathologically affected subjects [31]–[33].

The cause of aggregation is still a topic of scientific and clinical interest. The factors affecting aggregation are linked to the forces that cause the RBCs to aggregate. These forces include the forces causing aggregation and the forces causing dis-aggregation. An imbalance of these forces will cause RBCs to aggregate or dis-aggregate.

1.2.2.1 Clinical occurrence

Researchers have been trying to define the "normal" range of aggregation. The difficulty of this definition stems from the varying approaches and varying instruments used to obtain data. Aggregation varies based on biological and physiological conditions of the individual. For example, the sex or age of the individual will alter the aggregation levels of the sample. Women have been found to have higher aggregation rates, while elderly individuals also have increased aggregation rates [34]–[36]. It has also been found that aggregability of blood will increase during normal pregnancy [37]. The biological factors affecting RBC aggregability also include individual's hydration levels, hormone levels, and even the site

of sampling the blood is taken from [38]–[40]. For example, Mokken et al. found that venous blood shows slightly higher aggregation rates than arterial blood [38].

Pathological conditions may also cause RBC aggregation rates to change, usually with increased aggregability of RBCs in pathologically affected individuals. These include inflammatory conditions, infections, sepsis or shock, cardiovascular diseases, metabolic disorders, and hematological disorders [1].

1.2.2.2 Causes of Aggregation

The mechanism(s) resulting in aggregating forces are not yet fully understood. There are currently two models that attempt to explain this phenomenon. The bridging model presented by D. E. Brooks (Brooks 1988) and the depletion model presented by Baumler et al. (Baumler et al. 1996; Baumler et al. 2001) [41]–[43]. The bridging model describes the occurrence of RBC aggregation due to the presence of large macromolecules [1], [41]. The cross linking of macromolecules can cause the bridging of cells, leading to the formation of aggregates if the bridging forces exceed the forces from electrostatic repulsion, membrane strain, and mechanical shearing [1], [41]. The depletion model explains RBC aggregation due to a lower localized protein or polymer concentration near the cell membrane compared to the suspending medium [1], [42], [43]. An attraction force between the cells is caused through the osmotic gradient, thus leading to aggregation.

1.2.2.3 Causes of Dis-aggregation

The causes of dis-aggregation of RBCs are more uniformly accepted in the field. There are three main dis-aggregating factors: 1) Shear forces, 2) Surface charge density, and 3) Membrane strain. First, shear forces are mechanical forces that develop due to unaligned forces applied to a body. These forces prevent the formation of aggregates in blood and can cause the dis-aggregation of blood that has already aggregated. In healthy individuals, blood will not aggregate at shear rates as low 20-40 s^{-1} [8], [9]. In pathologically affected blood however, the attractive forces causing aggregation can require higher shear rates to disperse. Secondly, RBCs have a natural repulsive electrostatic force that causes individual RBCs

to stay apart. Lastly, the membrane strain of the RBC can prevent aggregation from occurring. An RBC needs to deform to allow other RBCs to get close. The strain then imposed through the membrane directly attempts to prevent RBC aggregation.

1.2.2.4 Other Factors Affecting RBC Aggregation

The following subsections, 1.2.2.4.1, 1.2.2.4.2, 1.2.2.4.3 include other factors affecting RBC aggregation. These include the effects of shape, hematocrit, and polymers respectively, on RBC aggregation.

1.2.2.4.1 Shape

Studies have shown that the bi-concave disk shape of RBCs plays a huge role for the formation of aggregation. A study by Windberger and Baskurt in 2007, showed the need for the bi-concave shape in relation to aggregation [44]. The study depicted an analysis of RBC samples from varying animals all with different cell sizes and shapes. It was found that animals with RBCs that have high deformability and a bi-concave disk like shape aggregated more than others. For example camelids had no aggregation due to their oval RBC shape [44]. Other studies have looked into the aggregability of RBCs after alterations to their shapes have occurred. Cicha et al. found that changing the spherical shape of RBCs in more acidic pH, prevented stable rouleaux formation [45]. Morphologies of RBCs have been shown to decrease aggregability as well (i.e. echinocytes) [46], [47].

1.2.2.4.2 Hematocrit

The hematocrit (volume fraction) of RBCs can play an important role in aggregability as well. If the hematocrit is too low for RBCs to come in contact it will reduce the aggregability of the blood [48]. Deng et al. found that RBC hematocrit had a strong non-linear effect on aggregation levels. The study showed aggregation in RBCs plateaued at around 40% hematocrit, with both the higher and lower ends showing lower levels of aggregation (70% and 10% respectively).

1.2.2.4.3 Artificially Induced by Polymer

The aggregability of RBCs can be altered using an assortment of polymers not found in blood plasma. The most common one used to induce aggregation is Dextran. Dextran is a complex branched glucan that can induce or inhibit RBC aggregation [1]. A study done by Chien et al. concluded that Dextran of increasing molecular weight had an increase of aggregability [49]. They also showed that the concentration of Dextran below a molecular mass of 40kDa had no substantial effect on RBC aggregation. Studies have attempted to find the ideal Dextran molecular mass and concentration for inducing RBC aggregation. Multiple studies completed have looked into the relationship between the molecular mass of Dextran and the aggregability of blood [50], [51]. All research points towards increased aggregation with increased molecular mass of Dextran. A study by Neu et al. contradicts previous findings by comparing a wide range of Dextran molecular mass [52]. They showed that a molecular mass of between 200-500 kDa is ideal for aggregation [52].

Though the molecular mass-aggregation relation shows semi consistent results, Armstrong et al. propose that the hydrodynamic size of polymers is a better distinguishing criterion for inducing aggregation via polymer [53]. Their results indicated a threshold of 4nm for the hydrostatic radius; i.e. polymers with radii higher than 4nm increased aggregation while polymers with radii less than 4nm decreased or had no effect on aggregability [53].

A comparison of Dextran concentrations is necessary to determine the ideal concentration for RBC aggregability. A study by Neu et al compares the polymer concentration levels of Dextran 70 (70 kDa) and Dextran 500 (500 kDa). The studies results are consistent with other studies of aggregation and polymer concentration relations. Figure 1-3 shows the RBC aggregation levels of Dextran 70 and Dextran 500 in relation to the concentration of Dextran used in isotonic solutions [54]–[56].

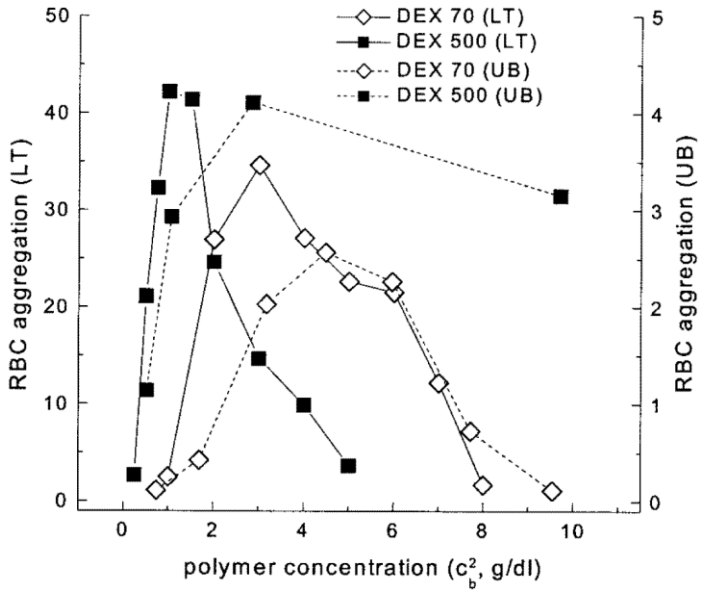

Figure 1-3: *Aggregability of RBCs suspended in Dextran 70 and 500 solutions, comparing the polymer concentration to aggregation rate. (Light transmission data (LT), Ultrasound backscatter data (UB)) [54].*

The ideal concentrations of Dextran 70 and Dextran 500 are consistent with results from the study in terms of interactional energy. Thus, an increase of interactional energy will cause an increase in aggregation, likewise a decrease in interactional energy will cause a decrease in aggregation. The ideal concentration of Dextran 70 and Dextran 500 for RBC aggregation is around 3g/dL and 1.5g/dL respectively.

1.2.2.5 Effect of Aggregates on the Flow

RBC aggregation plays a major role in blood rheology. The formation of aggregates is one of the main reasons blood acts as a Non-Newtonian fluid. The viscosity of blood is considerably altered depending on the aggregation level of the blood ranging from 3cP to 1.3cP [18]. The viscosity changes based on the vessel size, with viscosity decreasing as vessel diameter decreases. For this reason, the factors that affect blood aggregability also affect the viscosity. These factors need to be kept in consideration when studying blood flow *in vitro*.

A study done by Harry L. Goldsmith shows that RBCs and rod like rouleaux spend most of their time aligned with the flow direction [57]. He also saw that rod like structures in flow that are rotating are

subjected to compressive forces from alternate quadrants called springy orbits. This leads to the rod like structures tending to align themselves in ways where they are under tensile stress. Goldsmith found that rouleaux consisting of 10 or more cells demonstrated the existence of springy orbits, thus aligning themselves parallel with the flow direction [57].

1.2.2.6 Quantifying RBC Aggregation

There are many ways to quantify RBC aggregation. The oldest way to do so is observing the phase separation of blood. This was first published by Edmund Faustyn Biernacki in 1897 [58], [59]. The process was coined erythrocyte sedimentation rate (ESR). He, like Fahraues (Fahraeus 1929), also noticed that ESR increased in patients with diseases [30], [58], [60]. Even though this method is currently still being used in clinical settings it is seen as an indistinctive method for indicating inflammation [61], [62]. Since the introduction of ESR methods, there have been many other ways of quantifying and classifying RBC aggregation. These include the Zeta sedimentation ratio (ZSR), low shear viscometry, microscopic techniques, image processing and ultrasound backscattering techniques [1]. More detail into microscopic techniques, image analysis and backscattering techniques are found in the following sections of this chapter.

1.2.2.6.1 Aggregation Index and Microscopic Techniques

Microscopic observation techniques of aggregation were refined by Chien et al. in 1973, where they estimated the average number of RBCs in each aggregate [63]. The Microscopic Aggregation Index (MAI) is calculated by dividing the number of cellular units in the suspension of RBCs. For example, in the absence of aggregation, the MAI has a value of 1, with increasing values as RBC aggregation increases [1]. This method is simple and allows a good estimation of degree of aggregation in the sample. However, the disadvantages of MAI include the time-consuming nature of counting the cells as well as the lack of information considering time as a variable. From MAI more detailed and complicated procedures have come to light incorporating image analysis techniques.

1.2.2.6.2 Image Processing Techniques for Characterizing Aggregation

Visually analyzing RBC aggregates was one of the first methods used [30]. Since then a grading system was adopted and presented by Engeset et al. which graded aggregates from 0 to 4 based on the shape and size of the aggregate [64]. Adaptations of Engesets method were used to estimate the number of RBC in each rouleaux [63]. These methods were time consuming and tedious so more advanced and automated methods have been developed to streamline the procedure. One of these methods was developed by Erfan Niazi et al. [65], [66]. Niazi et al. developed an image processing algorithm capable of detecting RBC aggregates and quantifying them based on size, shape, and orientation. To find the size and shape of the aggregate, the algorithm uses filters and binary operators applied to the image. These processes help improve accuracy of particle detection and enhance the capability of detecting aggregates in a denser environment. It is important to note that the software does assume the aggregates to be moving in two dimensions. RBC aggregates will travel in three dimensions throughout the flow, so to ensure accuracy, thin rectangular channels are recommended. This promotes less overlap of aggregates *in vitro*. The aggregate orientation is measured using ellipses fitted to the shape of the aggregate. The angle of the ellipse is measured from the horizontal axis. The ellipse is then resized to match the overall area of the aggregate. Figure 1-4 shows examples of these steps from the algorithm. The algorithm was verified against manual methods using ImageJ software and was found to have errors of 2-4% with respect to the manual methods [65], [66].

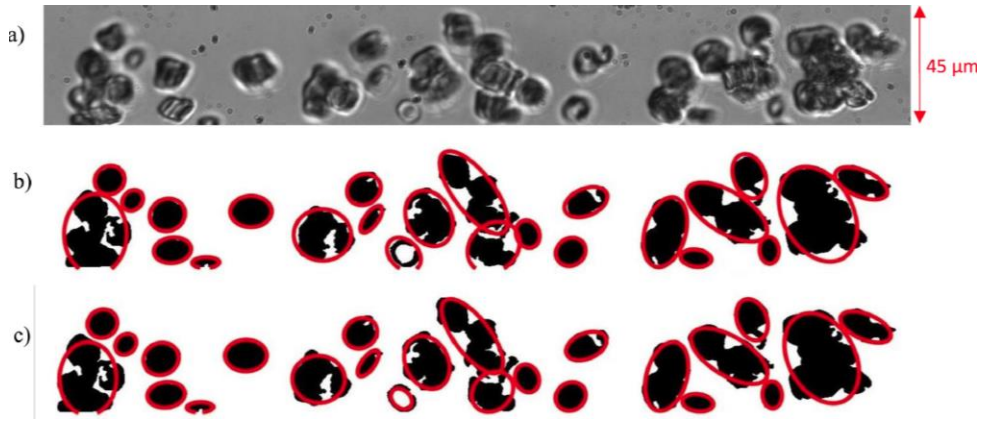

Figure 1-4: *Images depicting the steps used by the algorithm developed by Niazi et al. where a) is the original image, b) is the first step the algorithm takes in fitting ellipse to the aggregates, and c) is the second step, where the ellipse are resized to match the size of the aggregate [66].*

1.2.2.6.3 Ultrasound Backscatter Techniques

Ultrasound backscattering techniques are utilized to determine the relative size of the scatterer in question; i.e. the size and concentration of the RBC aggregate. The basis of these techniques is to analyze the power spectra of the radio frequency (RF) data. Once obtained from a working ultrasound device, the RFs can then be subjected to normalization procedures and the backscatter coefficient (BSC) can be obtained. The BSC is defined as the power backscattered by a unit volume of scatters per unit incident intensity per unit solid angle [67]. From the BSC, researchers have deduced information about the shape, size, concentration and acoustic impedance of the objects. The BSC itself is obtained by fitting experimental data to analytical models.

Backscattering techniques were derived from the works of Rayleigh et al. in 1945 where he determined a scattering theory where scattering was dependent on the ultrasound signal [68]. Around this time in history, diagnostic ultrasound devices were being developed by people, such as the Dussik brothers, using a through-transmission differential attenuation method to image the brain, or Firestone's development of pulse-echo imaging used in clinics [69]–[74]. Not long after the development of RADAR and SONAR, which utilized the understanding of pulse-echo principles from Firestone, the understanding of acquiring reflected ultrasound echos using water or direct contact methods was formalized. From these advancements modern backscattering techniques were developed and used for quantifying RBC aggregation.

To use the BSC to quantify RBC aggregates, theoretical advancements needed to be made. Twersky et al. developed an expression for the backscattered intensity in terms of a single particle backscattering cross section, the density of particles, and the packing factor [75]. This proposed model explained the relationship between the backscatter amplitude and the RBC hematocrit level but failed to consider RBC aggregation and only focused on single RBCs. Savery et al. took the packing factor theory and applied it to the aggregability of RBCs [76]. They proposed the frequency dependent structure factor which was later named the Structure Factor Model (SFM). The SFM was one of the first models used to fit experimental data on RBC aggregates [67]. From this model others have been developed to better represent RBC aggregates. One of the most recent models was developed by combining the SFM and the Effective Medium Theory (EMT). EMT was originally theorized by Kuster et al. when studying seismic waves in the scientific field of Geophysics [77], [78]. The combination of these two theories was proposed by Franceschini et al. to create the EMTSFM (2011), which assumes that RBC aggregates can be treated as homogenous scatterers [79]. Each of these scatterers have effective properties which can be determined by acoustical characteristics and RBC concentration. Franceschini et al. comparatively studied their theory against the Gaussian Model (GM) and the Structure Factor Size Estimator (SFSE) and found that EMTSFM was more suitable for characterizing RBC aggregation [80]. The expression for the BSC within the EMTSFM as seen in Equation (1.1)

$$BSC_{EMTSFM}(-2k) = n_{ag}\sigma_{ag}(-2k)S_{ag}(-2k) \quad (1.1)$$

where n_{ag} is the number density of aggregates in relation to the effective volume fraction of aggregates, σ_{ag} is the backscattering cross section of an effective single sphere, S_{ag} is the structure factor. The difficulty of applying EMTSFM or SFSE to *in vivo* studies is the attenuation caused by the tissue layers between the ultrasound probe and the blood flow. One model was recently developed to account for the attenuation by Franceschini et al. which was called the Structure Factor Size and Attenuation Estimator (SFSAE), adapted from the SFSE [81], [82]. SFSAE has been shown to be able to estimate blood structural properties *in vivo* and in-situ [81], [82]. Future improvements of these models include accounting for the aggregate anisotropy

shape and in the development of EMTSFM specifically, accounting for the attenuation of tissue [67]. Recently Chinchilla et al. have developed a new model adapted from the EMTSFM called the Effective Medium Theory and Local Monodisperse Approximation (EMTLMA). This model takes into consideration the anisotropic nature of RBC aggregates and is currently submitted for review to the Journal of the Acoustical Society of America. A more detailed summary of quantitative ultrasound techniques can be found in the *Quantitative Ultrasound in Soft Tissues* book by Mamou et al [67].

1.2.3 Microfluidics

The field of microfluidics has become a prominent field for studying blood rheology. It allows for small sample sizes, it's cost effective, and produces small amounts of waste. One of the major advantages to microfluidic techniques is the ability to apply multiple studies or functions at the same time. Clinical applications of microfluidics include the implementation of lab on a chip technology. Lab on a chip technology has grown quickly with the main concept of implementing full ranges of laboratory tests onto one device [83]. Major challenges to this exist through dealing with fluids at the microscale. These challenges include fabrication and flow physics at the microscale.

1.2.3.1 Microfluidic Flow Properties

Fluid flow behaviour in microfluidic systems can differ greatly from macroscale systems. Dimensionally microfluidics is within the scale of 1-1000um [84]. This small scale results in low Reynolds number. The low Reynolds number permits laminar flow which exhibits viscous forces more important than inertial ones. Intramolecular surface forces and boundary layers may also play a larger role in a microfluidic system compared to that of a macro system [84], [85]. At the microscale mixing occurs through diffusion which is a slow process [85]. These factors need to be taken into consideration when designing a microfluidic system.

1.2.3.1.1 Co-flow System

Co-flow, also called Couette flow, is the flowing of a viscous fluid between two surfaces. Traditionally one surface is moving while the other is stationary. This causes a shear across the viscous fluid. Looking at this flow in two-dimensional (2D) space Figure 1-5 depicts the scenario.

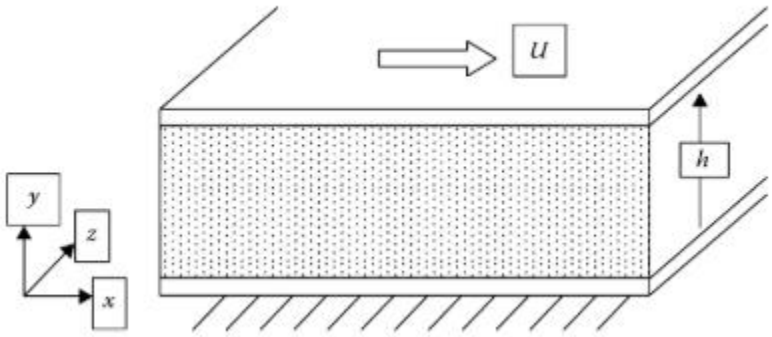

Figure 1-5: *Flow between two infinite plates [18].*

From Figure 1-5 it is possible to deduce the equation representing the velocity profile using the Navier Stokes equations. It is assumed to be 2D flow, the top surface is moving at a constant velocity, and the flow is considered steady in the x direction. The velocity profile is thus represented using,

$$u(y) = \left(\frac{U}{h}\right) y \tag{1.2}$$

where u(y) is the velocity profile, U is the velocity at h, h is the height of the channel, and y is the distance in the y axis. From Equation (1.2) it is possible to see that the velocity profile is linear. This results in a state of constant shear across the flow represented by the following equation;

$$\tau = \mu\left(\frac{du}{dy}\right) = CONSTANT \tag{1.3}$$

where τ is the shear stress, μ is the viscosity, du is the local slope of the velocity profile, and dy is the distance in the y axis. A Couette flow system has been used in microfluidics to study blood aggregation and is discussed in the following section of this report.

1.2.3.2 Couette Flow Experiments on RBC Aggregation

Shear forces are a factor when dealing with blood aggregation. Under low shear rates blood will aggregate, while under high shear rates blood will disaggregate. A study by Bishops et al. investigated RBC aggregation using the polymer Dextran 500 in a rat venule. The study was able to support the inverse relationship of aggregate size to shear rate [86]–[88]. This *in vivo* study matched *in vitro* studies done before [7]. Therefore, it is important to understand this relationship to RBC aggregation and shear rate. One of the easiest ways to study aggregation *in vitro* is to use a co-flow shearing system. For example, the rotating cylinder viscometer, also called the Couette viscometer, has been used for some blood aggregation studies [89]. Figure 1-6 depicts a schematic of a classical Couette viscometer. The Couette viscometer traditionally consists of a concentric cylinder placed inside another cylinder with a small gap between the two. Either the inner or outer cylinder rotates creating a constant shear torque across the fluid in the gap. Alternate configurations include the Mooney, cone, and plate viscometers.

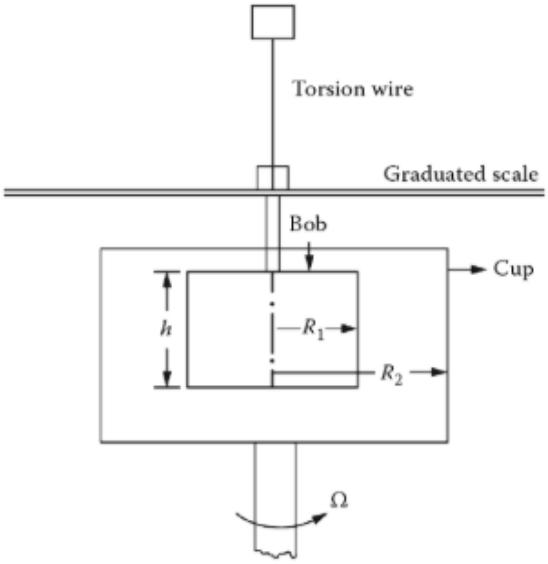

Figure 1-6: *Diagram of a Couette viscometer [18].*

A study done by Kaliviotis et al. utilized a co-flow shearing system to analyze RBC aggregation and its effect on viscosity [89]. They were able to show that the variation of viscosity across the flow was due to the RBC aggregates.

Couette shearing systems have also been incorporated into microfluidic systems in order to reduce the sample volume and offer better visibility of the suspension. Studies done by Mehri et al. have incorporated a two-fluid low shear rate microfluidic device using the same shearing concepts as a Couette viscometer [8], [9], [90]–[92]. The system used in Mehri et al. studies consists of a microchannel with two inlets and one outlet as seen in Figure 1-7. The flow rates of the shearing flow are controlled separately of that of the sheared fluid.

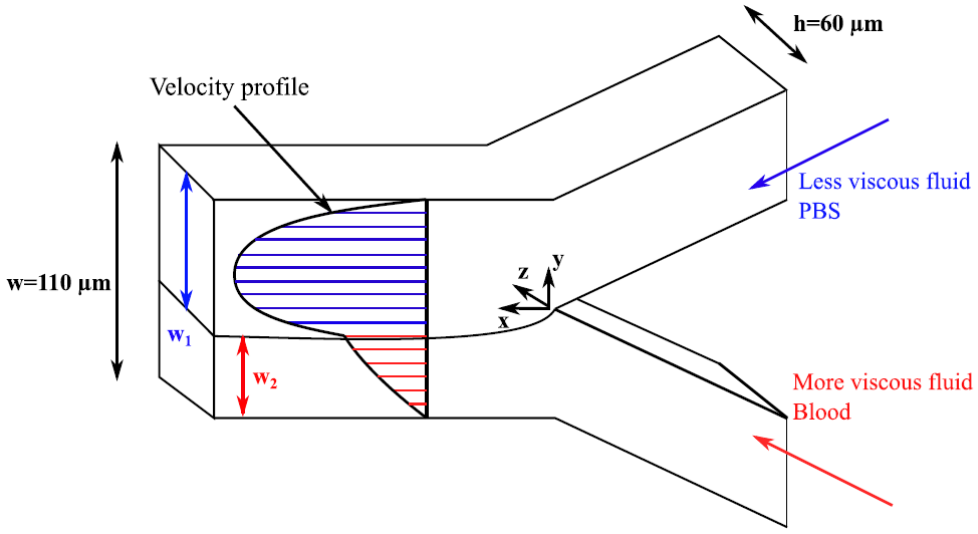

Figure 1-7: *Two fluid shear system used by Mehri et al. for RBC aggregation characterization [8].*

The ratio used to create a pseudo-constant shear rate was 4:1 of shearing fluid to RBC flow. Low hematocrits were used and analyzed by Mehri et al. showing relationships between viscosity, shear rate, hematocrit and temperature to aggregation characteristics. Mehri et al. characterized aggregate size and shape using the algorithm developed by Niazi et al. as mentioned in section 1.2.2.6.1 of this chapter [65], [66].

1.2.3.3 Microfluidic Devices

Microfluidic chips are most commonly manufactured using Polydimethylsiloxane (PDMS) [93]. PDMS is widely used due to its transparency [94], low costs, and ease of manufacturing [93], [95], [96]. Perfusing microfluidic chips can require several hundred bars of pressure to overcome the resistance of the

system. Under pressure, the dimension of the channels can significantly change depending on the compliance [97]. The compliance is the change in volume for any given applied pressure. When using a syringe pump as the system's input source, the time it takes for the system to reach steady flow conditions can vary from seconds to hours depending on the fluidic resistance and compliance. This time until steady flow conditions are reached is called the response time or the characteristic time.

PDMS has a low elastic modulus (1 to 3 MPa) which allows deformation of the device under high pressures [95], [96], [98]. At a low Reynolds number, the law that governs fluid flow is the Hagen Poiseuille model. The hydraulic resistance of a microchannel is a function to the power of 4 of the hydraulic diameter of the channel. As a result, a small variation in this dimension, due to the deformation of the elastomer resulting from pressure, can cause significant variation in the hydraulic resistance and thus, invalidate the expected flow rate.

To overcome the limitations associated with PDMS, other materials have been used for the fabrication of microfluidic devices. One of the most promising materials is the optical glue Norland Optical Adhesive (NOA). The manufacturing process used to design the NOA chip is comparable to that of the PDMS gold standard [99]–[101]. This material is clear and around 160 times more rigid than that of PDMS (Youngs modulus of 325MPa) [99], [100]. This allows NOA to be used in high pressure flow systems with minimal compliance as shown by Elodie Sollier et al. when comparing PDMS to other forms of polymer based materials, including NOA, in high pressure flow systems [8].

1.2.3.4 Norland Optical Adhesive Microfluidic Devices

NOA microfluidic devices offer more rigidity and are less compliant than that of their silicone counterparts. Jae Hwan Sim et al. fabricated NOA devices using a sequential replica molding technique [99]. This technique involves the stamping of a positive patterned PDMS mold on uncured NOA81. The positive patterned PDMS mold is created from a silane treated negative patterned PDMS mold. The stamped NOA81 is then pre-cured in UV light and the stamp is removed. A top is made in similar fashion with metal inserts for inlets and outlets. The UV imprinting technique was based on Bartolo et al. in which he uses the

techniques in the fabrication of micro-patterned stickers [103]. Figure 1-8 is a diagram of the methodology used by Jae Hwan Sim et al [99].

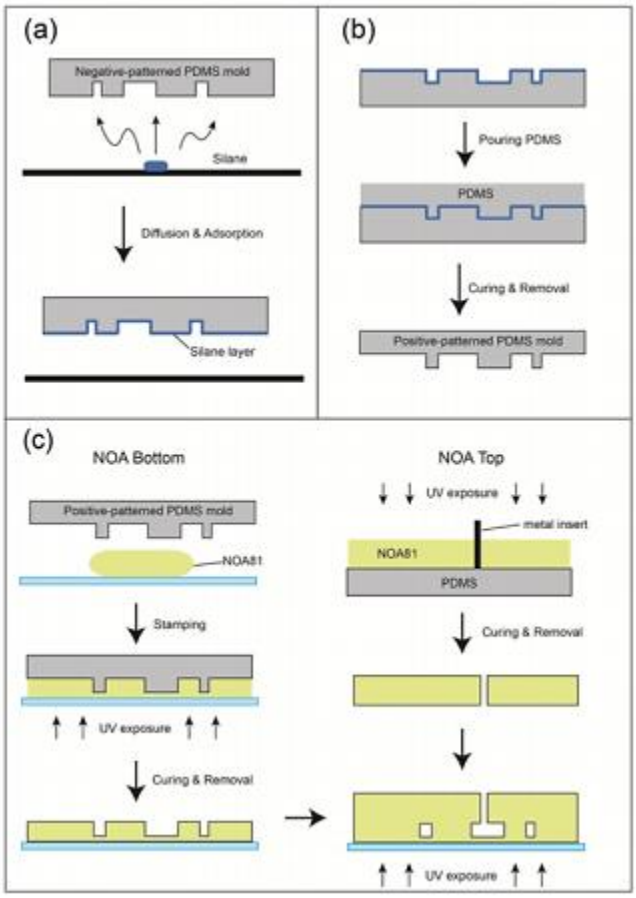

Figure 1-8: *Diagram from Jae Hwan Sim et al. describing the fabrication process for NOA microfluidic device where a) is the silanation treatment of PDMS, b) is the creation of the positive PDMS mold, and c) is the UV treatment of the NOA device [99].*

Other methodologies have been used for NOA microfluidic devices. Dupont et al. developed a NOA microfluidic deice using NOA 63 [100]. Dupont et al. pour the NOA directly onto an SU-8 wafer and encased by a hollow PDMS mold. After exposing the NOA 63 to 140s of UV light, it is removed and plasma bonded to a piece of PDMS. When studying their device Dupont et al. found that the NOA 63 produced very stable hydrophilic properties in comparison to PDMS, when exposed to oxygen plasma [100], [101].

Since NOA is a relatively new material for microfluidic device fabrication, the properties of NOA are still being characterized. Wagli et al. looked into the wetting behaviour and the chemical resistance of

NOA [104], [105]. NOA surfaces were made hydrophobic through an additive into the uncured polymer. It was also found that NOA samples were resistant to many Infar-red organic solvents with low polarity [104].

1.2.4 Particle Image Velocimetry

Using particles placed in a fluid to study the flow and velocity is an old concept. It is first recorded to have been a technique used by Ludwig Prandtl around 1930 [106]. Since then more techniques have been used such as Laser Doppler Velocimetry and Laser Speckle Velocimetry which allowed velocity measurement at a point in space. These techniques all predate Particle Image Velocimetry (PIV) which, unlike its predecessors, is able to measure velocity of a fluid in 2D and/or three-dimensional (3D) space. PIV is a technique used in both macro and micro fluid flows, although the technique differs depending on the respective scale. The hardware setup affects the PIV processing techniques used. For example, incorporating an interline transfer camera to capture double frames at short intervals allows the use of the cross-correlation processing method. On the other hand, using a normal camera only allows one image to be taken. With one image the auto-correlation method is used. Cross-correlation is more accurate than auto-correlation since the velocity vectors have less directional ambiguity when using cross-correlation techniques [1], [107], [108]. Therefore, for the duration of this section a PIV setup incorporating an interline transfer camera will be the focus.

When using an interline transfer camera, the dual images are illuminated by a double-pulsed laser. The timing between the two images, dt, is controlled and altered based on the flow rate of the fluid being analyzed. The dt is usually around 10^1 to 10^3 microseconds in magnitude. The choice of the dt is driven by the need to ensure getting a particle shift within the flow that does not exceed one quarter of the correlation window size [8], [9], [90]. Particles used within the flow are called tracer particles and are usually reflective in classical PIV and fluorescent in micro PIV. Therefore, the reflective tracers will scatter light and the fluorescent tracers will emit light when the laser hits them. The tracer particle size can range anywhere from 10um to 30um in classical PIV [109] and less than a micron in micro PIV. Laser pulsations are timed with the camera's dt to ensure that the images depict the particle flow with the medium. The interline

transfer camera will take (usually around 100 pairs) paired images and they will be analyzed using the cross-correlation method on the appropriate software.

To prepare the paired images for cross-correlation, each image is discretized into smaller sections called interrogation windows. These interrogation windows need to be larger than the particle displacement to ensure accuracy of the cross-correlation method. The cross-correlation technique is explained by Keane et al. as follows [108];

$$R(s) = \int I_1(X) I_2(X - s) dX \tag{1.4}$$

Where X is a spot on the interrogation frame separated by vector s, $I_1(X)$ is the transmitted light from the image after interrogation by the laser, $I_2(X\text{-}s)$ is the image intensity of the second frame taken dt after the first, and R(s) is the image displacement [108]. This explanation is further reinforced by Raffel et al. who explain the theory of cross correlation using the interrogation window size as follows [110];

$$C_{x,y} = \sum_{i=-L}^{L} \sum_{j=-M}^{M} I(i,j) I'(i + x, j + y) \tag{1.5}$$

Where I and I' are the intensity values of the paired images, L and M represent the size of the interrogation windows and C(x,y) is the displacement [110].

1.2.4.1 Micro PIV

Micro PIV (µPIV) has three distinct differences from its macro scaled counter parts. These differences are widely known in the field, but are displayed clearly by Werely et al. [111]. Looking at the particles used in macro PIV they are much larger in size than µPIV. Particles in µPIV range from 0.1 to 5µm in diameter versus macro PIV particles which are at least 10^1 in magnitude larger. Due to the sizing of the particles in µPIV, they become too small to be detected by the wavelength of the laser. This can be remedied by tagging the particles in the flow, with fluorescents. The particles in standard PIV are illuminated using a laser sheet. This method cannot be replicated for µPIV as the flow size in question is too small and would result in laser diffraction. Therefore, in µPIV a volume illumination method is used to illuminate the particles [112],

[113]. This method illuminates the entire test section using a 3D volume of light, opposed to the 2D illumination used in a sheet illumination method [112]. Due to the use of the volume illumination method in µPIV two factors become important in the post processing of images. These factors are the Depth of Field (DOF) and the Depth of Correlation (DOC). The DOF relates to the microscopes focus plane while the DOC is an estimation of the thickness of the measurement volume [114]. One of the final big differences between macro PIV and µPIV stems, again, from the small particle size in µPIV flow systems. Due to the small size, the effect of Brownian motion has a larger impact on the results. Brownian motion is the random movements of the particles as the flow through the medium [115]. These random motions can be limited by averaging the sets of paired images obtained from the camera.

1.2.4.1.1 Micro PIV used to Study RBC Velocity

The µPIV technique was first believed to have been developed by Santiago et al. in 1998, when they analyzed the velocity field in Hele-Shaw flow around a 30um elliptical cylinder [113]. Since then the use of µPIV in microfluidic devices has been increasing. For example, Pitts et al. presented a protocol to obtain measurements of blood flows in microchannels [116]. These measurements included shear rate, maximum velocity, flow rate, and velocity profile shape [116]. The protocol presented by Pitts et al. is similar to techniques used by Kim et al. when they studied velocity profiles of blood flow through microchannels. The major difference is that the study by Kim et al. utilized RBCs as tracer particles instead of micro/nano particles.

One of the earliest studies done combining µPIV techniques to the field of hemorheology was done by Sugii et al. in 2002 [117]. Their highly accurate µPIV techniques were applied to images of a rat's mesentery, specifically the arteriole. They used an intravital microscope and a high speed digital video system to acquire images of the blood flow. Accounting for the movement of the mesentery, the study was able to acquire complete velocity profiles along the vessels cross section. The *in vivo* study suggests that highly accurate *in vivo* studies could be done even in the micro-vessels. This study was repeated by Nakano et al. with consistent results [118]. Sugii et al. went on to develop *in vitro* techniques in round microchannels

[119], [120]. The results obtained again had a high spatial resolution (9um x 2.2um) and high temporal resolution (6000 Hz) [119], [120].

Other *in vitro* studies have explored blood velocity. Bitsch et al. completed studies on blood velocity profiles through flat micro capillaries [121]. They investigated the plug flow nature of the velocity profiles. A cell free layer was found to cover 21% of the channel width. From their finding they were able to conclude that blood flow is best represented as a two-phase model.

The studies done by the aforementioned Pitts et al. show the accuracy of the µPIV methods in microfluidic devices [116], [122], [123]. They found that fluorescent particles obtained more accurate velocity profiles when used as tracer particles in comparison to using RBCs as tracers. The work done by Mehri et al. complement the findings of Pitts et al [8], [65], [91], [92]. They also investigate the relationship of viscosity to the aggregability of blood flow. The shearing system used by Mehri et al. is capable of measuring shear rates from around 2 s^{-1} to 50 s^{-1} while simultaneously characterizing aggregate size and shape [8].

1.3 Thesis Statement

This thesis presents research of RBC aggregation and its characterization using microfluidic techniques. A new microfluidic device is presented and verified with a detailed calibration of its flow properties within a co-flow system. The aggregation characterization was completed using software developed by Niazi et al. which allowed image detection of aggregation in high resolution images of RBC aggregation [66]. The software was used on porcine blood samples acquired by Mehri et al. in collaboration with LMA [8], [91]. This was done to acquire data necessary for developing their backscatter model, the Effective Medium Theory and Local Monodisperse Approximation (EMTLMA), which will be submitted to the Journal of the Acoustical Society of America. LMA is working on using ultrasound backscattering techniques to characterize blood aggregation *in vivo* taking into consideration the anisotropy physiological properties of RBC aggregation. Currently they utilize porcine blood samples, with the desire to move to human blood

samples. The current system used at LMA, a rotating Couette flow system similar to the viscometer presented Figure 1-6, requires 100ml of blood to facilitate their co-flow apparatus. This amount is an unrealistic amount to acquire from human blood samples. Therefore, by transitioning their co-flow system to a microfluidic device, they will be able to use human blood samples. They also will be able to view the blood flow microscopically at the same time while running their experiments. This will allow for verification and comparison of their results.

The novel microfluidic device developed and presented in this thesis, is to allow the group at LMA to transition to human blood samples. The device fabrication methodology is adapted from work done from Jae Hwan Sim et al. [99]. It is manufactured from NOA, giving the device low compliant properties. The low compliant behaviour of the NOA device is verified experimentally and analyzed using the Windkessel Theory [18]. To develop the device and the methodology Benoit Charlot (IES, Institut d'Electronique et des systèmes, UMR5214, CNRS, Montpellier, France) manufactured the SU-8 wafer mold used to fabricate the device. Also, Andy Vinh Le contributed by verifying the methodology presented in this thesis by completing it successfully on his own accord. Work done on the fabrication and verification of the NOA microfluidic device is submitted, currently under review, at the Journal of Microelectronic Engineering at the time of this thesis submission.

The calibration of the NOA microfluidic device under co-flow conditions was completed in Ottawa in consultation with LMA to address their constraints. The device development is to allow them to work on human blood samples instead of porcine ones. By calibrating the shear rate applied to the blood flow through the device, the team at LMA will be able to begin adapting their ultrasound backscattering techniques to the device and use it without a comprehensive microfluidic platform (μPIV, driven pressure flow, etc..). The goal of this research is to aid the team at LMA with RBC aggregation characterization, develop a microfluidic device capable of controlling RBC aggregation through controlling shear rate, calibrate the device's flow properties, and allow the device to be incorporated in the works of the team at LMA.

The results obtained from this research may contribute to advancements in the field of microfluidics by providing new microfluidic device fabrication techniques. They may also contribute to future research in the field of hemorheology by providing the RBC aggregation characterization through multiple physical properties including size, shape, and orientation to the flow. Lastly the research presented in this thesis will have an impact on development of the ultrasound techniques, by allowing the team at LMA to verify their techniques through the microfluidic device.

1.4 Research Goals

This thesis is part of an international project aiming to develop diagnostic tools capable of assessing RBC aggregation *in vivo* locally. Such devices would aid in identifying hemorheological disorders that could lead to microvascular dysfunctions and venous thrombosis. The focus of this thesis is to develop and validate a microfluidic device capable of incorporating an ultrasound transducer for RBC aggregation characterization. With this device, microfluidic techniques could be used to allow the focus of the international project to shift from porcine blood to human blood. This project is in collaboration with Dr. Franceschini et al. at LMA in Marseille France. They have developed ultrasound techniques capable of measuring RBC aggregation *in vivo*. In order to reach this goal, their methodology needs to be verified. Thus, a microfluidic device capable of optical and ultrasound measurements of RBCs under controlled aggregation is needed. This will be used to validate a cellular ultrasonic imaging methodology used to assess RBC aggregation *in vivo*.

The objective of this thesis is to aid in the verification process of the ultrasound imaging methodology in part of the international study. To do so, the EMTLMA model developed by Franceschini et al. needed more theoretical analysis. Therefore, in collaboration with Lenin Chinchilla, a detailed RBC aggregate characterization methodology was developed using Niazi et al. novel algorithm. Porcine blood form Mehri et al. work was analyzed and used to develop the theoretical model which is set to be submitted in the Journal of the Acoustical Society of America (JASA). In addition, blood aggregation characteristics were investigated in a low compliant device. To control shear rate and the blood flow as done by Mehri et al.

pressure driven flow cannot be used. Therefore, using a syringe pump to drive the flow a solution needs to be developed to minimize the compliance of the system. Firstly, a fabrication method for a novel, less compliant microfluidic device was completed, keeping optical clarity as a priority. This device was calibrated to achieve the desired hemodynamics used to study the effects of blood aggregation through a controlled *in vitro* environment. In addition, the RBC aggregation characteristics were investigated, directly comparing the shear rate, the Dextran concentration, and the flow rate. This allowed further investigation into the microfluidic device's capability of controlling the shear rate of a non-Newtonian fluid using µPIV techniques to record the velocity profile and corresponding flow properties.

To achieve the main goal of this thesis and contribute towards the aim of this international project, the following three tasks need to be completed. They are presented as follows;

1) A segmentation methodology needs to be applied and verified using pre-existing high speed microscopic images of porcine and human blood *in vitro* to help verify the EMTLMA model of RBC aggregation.
2) A fabrication process needs to be developed and verified for a less compliant microfluidic device in comparison to the gold standard; PDMS, allowing for integration of an ultrasonic transducer for simultaneous data collection.
3) The microfluidic device then needs to undergo verification of shear rate control using µPIV techniques, assessing shear variation at multiple concentrations of Dextran 70 and Dextran 500 so as to ensure the team at LMA can incorporate their current procedure to the world of microfluidics seamlessly.

1.5 Thesis Structure

The document is organized into five chapters; the present chapter includes the motivation behind the research and a detailed literature review of the topics covered in this thesis. It also outlines the thesis statement and research goals. The following chapters are structured to address all three objectives

outlined in section 1.4 (Research Goals), in the same order as presented in section 1.4. An overview of the chapters content is as follows:

Chapter 2 presents the methods used throughout this study, both experimentally and analytically. This includes detailed descriptions and materials used.

Chapter 3 includes all major findings from the research conducted. This includes segmentation analysis of porcine and human blood samples, NOA microfluidic device compliance verification, and the shear rate calibration of the NOA microfluidic device.

Chapter 4 provides detailed discussions on the findings of chapter 3. This includes possible factors affecting the outcome of the results.

Finally, Chapter 5 concludes the research conducted in this thesis outlining the contributions made and highlighting future areas of study.

Chapter 2

2 Methodology

This chapter outlines the methods used for the characterization of RBC aggregates, the microfluidic device fabrication and compliant characterization, and the flow properties and calibration of the microfluidic device.

2.1 Aggregation Characterization

The image processing techniques used for analyzing the aggregation of RBCs *in vitro* were done using an in-house MATLAB application developed by Niazi et al. [66], [124]. The details for image preparation and selection are detailed in subsection 2.1.1, whereas the application procedure and post processing analysis are found in subsection 2.1.2.

2.1.1 Image Acquisition

Images were selected from pre-existing experiments done by Rym Mehri [9], [124]. Three porcine experiments were chosen for analysis and one human experiment. These were chosen in accordance with LMA and their current experimental procedures. The experimental recordings were acquired using a high-speed (HS) camera (Graftek Imaging, Inc., Austin, TX, USA). The blood flow observed is undergoing a pseudo-constant shear rate through a co-flow system, similar to the co-flow system presented in chapter one of this report (subsection 2.3.2). A total of 150 pictures were analysed for each recording set of 1500 images. The porcine and human samples selected were tested at hematocrits of 10% or 20%, at flow rates ranging from 7.5µl/hr too 240µl/hr. Each flow rate had multiple sets of recordings. These recordings were analyzed separately. Every tenth image in a set was analyzed using the Niazi et al. algorithm. Figure 2-1 shows an example of one of the pig's blood images at varying flow rates, before post processing.

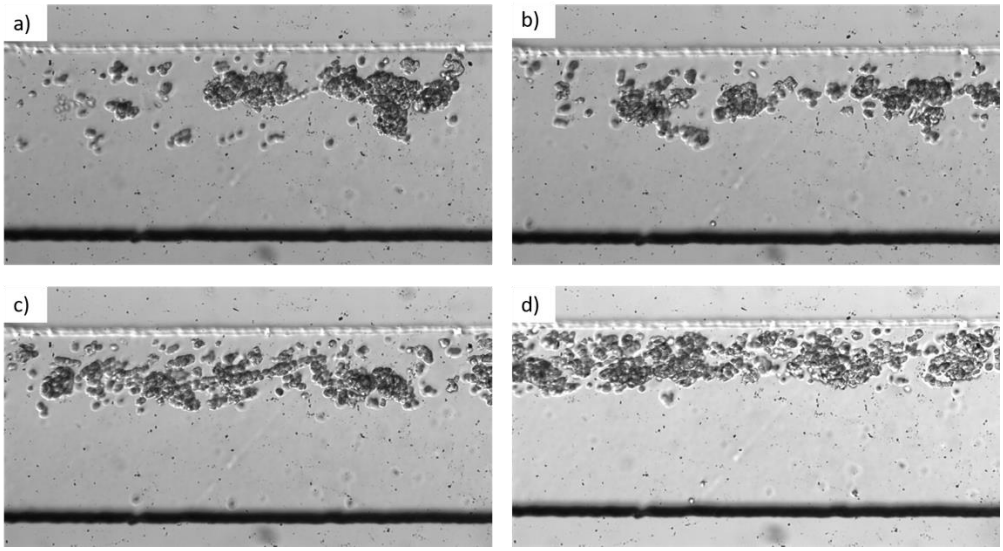

Figure 2-1: *Raw images from Mehri et al. of porcine blood in a co-flow microfluidic system for flow rates of a) 10µl/hr, b) 20µl/hr, c) 30µl/hr, and d) 60µl/hr.*

Table 2-1 gives a complete overview of the data that was prepared for post processing. It includes the type of blood analyzed, the flow rate, and the number of tests analyzed.

Table 2-1: *General Overview of all of Rym Mehri's data analyzed using the post processing procedure [9].*

SAMPLE NUMBER	TYPE OF BLOOD	FLOW RATES ANALYZED (µL/HR)	NUMBER OF TESTS PROCESSED
1	Porcine (PIG 1)	20, 30, 60, 120, 240	20
2	Porcine (PIG 2)	7.5, 10, 20, 30, 60, 120, 240	41
3	Porcine (PIG 3)	10, 20, 30, 60, 120, 240	33
4	Human (Aa03B)	10, 20	5

2.1.2 Image Processing

To analyze the images the same segmentation MATLAB application, developed by Erfan Niazi, was used [66]. The applications segmentation techniques for size and orientation are outlined in subsection 1.2.1, while the image filtering and binary operators can be found in section 1.2.2. Finally, the measurement and saving procedure is outlined in section 1.2.3 and the analysis in section 1.2.4.

2.1.2.1 Size and Orientation

The application segregates each RBC aggregate and estimates its size and shape based on the shape of an elliptical. The particle detection developed by Niazi et al. was tested, verified and published in the

Journal of Advances in Engineering Software (2019) [66]. Each detected particle is fit to an ellipse that encases the particle in question. The major and minor axis of the fitted ellipse, as well as the total area and the orientation from the horizontal axis, are saved in a csv file format. The algorithm then takes the overall pixel area and scales the fitted ellipse appropriately to match the area. The fitted ellipse data is then used to present the ellipse size, the axis ratio (minor over major axis) and orientation of the individual aggregate. This creates a more accurate ellipsoid projection in two dimensions. The two-step process is outlined in Figure 2-2. Figure 2-3 depicts the quantitative parameters extracted from each ellipse.

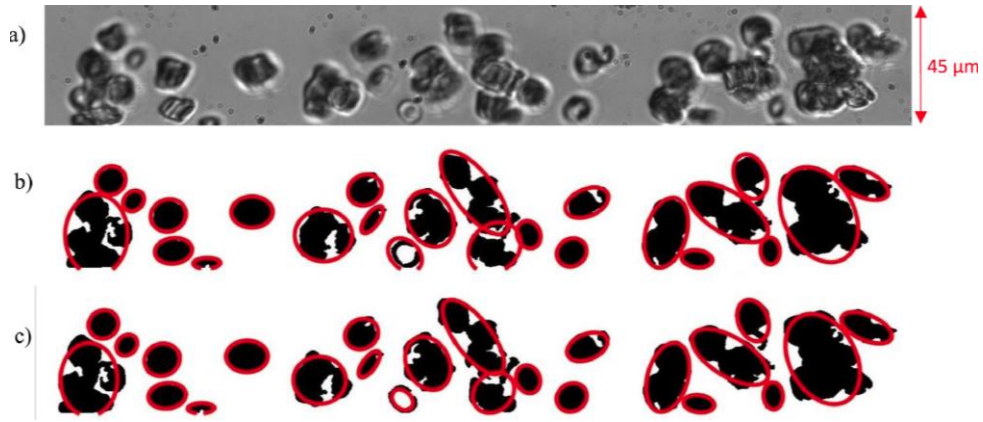

Figure 2-2: *Images depicting the steps used by the algorithm developed by Nirazi et al. where a) is the original image, b) is the first step the algorithm takes in fitting ellipses to the aggregates, and c) is the second step, where the ellipses are resized to match the size of the aggregate [66].*

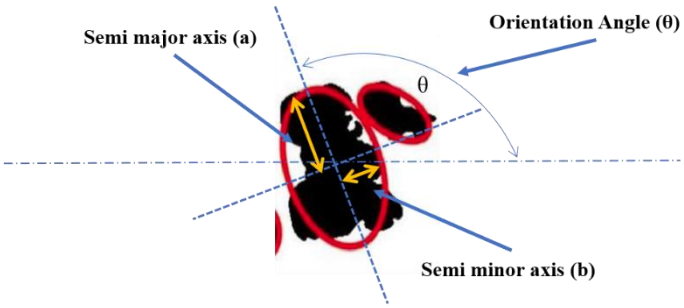

Figure 2-3: *Quantitative parameters extracted from the Niazi et al. algorithm; semi major axis (a), semi minor axis (b), and orientation angle (θ).*

2.1.2.2 Image Filtering and Binary Operator selection

To obtain accurate ellipsoid projections of the aggregates, the first image of each series is selected, and alterations are made in order to improve the automatic processing. The algorithm by Niazi et al. consists of filtering and binary image processing options. These options are outlined in Figure 2-4 and Figure 2-5. A combination of these processes was used to ensure accurate RBC aggregate detection.

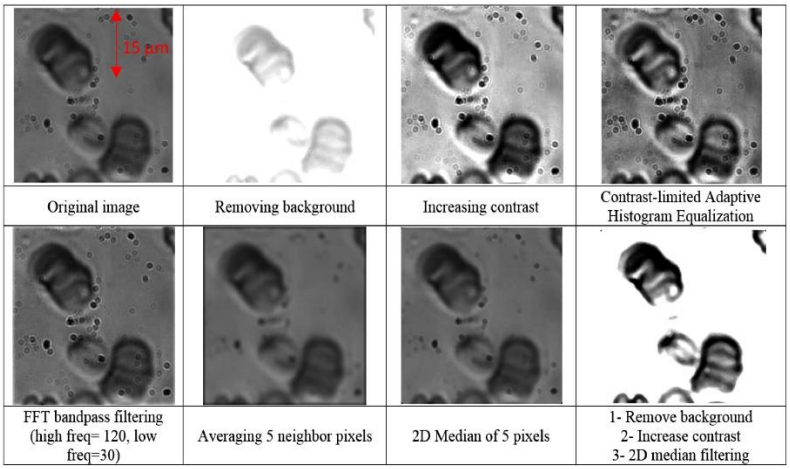

Figure 2-4: *Image from Niazi et al. showing effects of each image enhancement filter [66].*

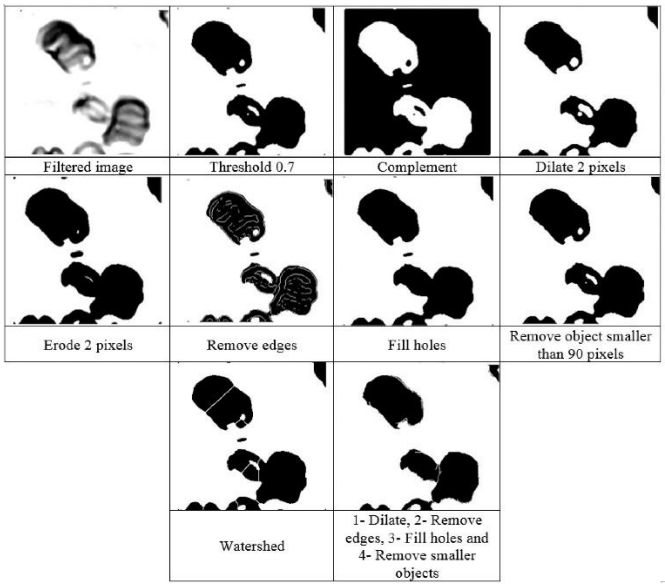

Figure 2-5: *Figure from Niazi et al. outlining the binary operators available in the algorithm [66].*

The filters and binary options used in this study are adapted from the suggested protocol for segmentation from Niazi et al. for sheared flow [66]. The background is removed from the image and the contrast of the

image is increased. Two-dimensional medium filtering is also used. Next binary operators are applied. The smaller objects (smaller than individual RBCs) are removed, holes in the binary image are filled, and edges are removed. Finally, the threshold of the operators is altered until each aggregate can be visualized individually in the binary image. The filtered image is used as reference when altering the threshold. Figure 2-6 clearly depicts the image processing and the effects of filters and binary operators to prepare for automatic processing. This concludes the manual set up of the image processing. The next section (2.1.2.3) goes over the automatic processing of the algorithm.

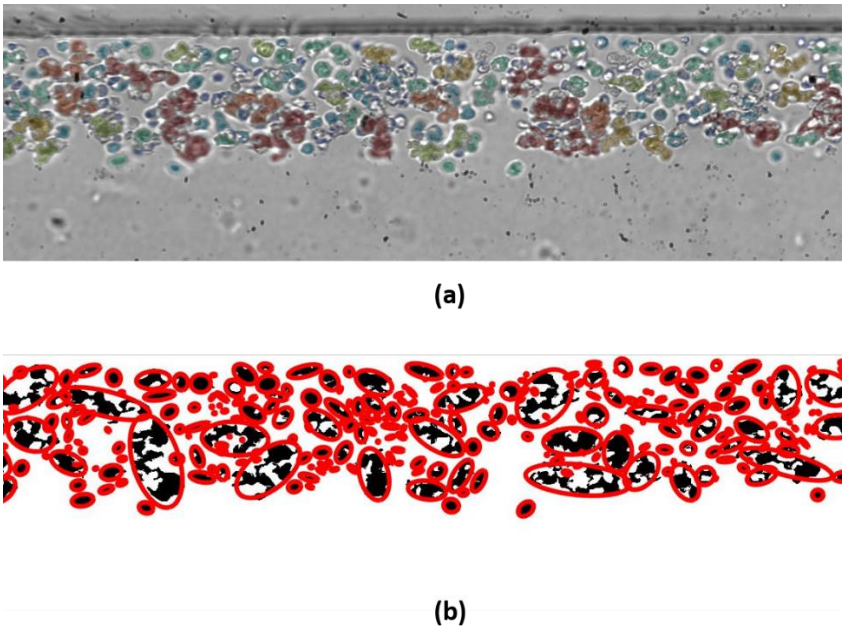

Figure 2-6: *a) RBC aggregate detection through the filtered image. b) Ellipse measurement detection of the automatic processing.*

2.1.2.3 Measurement and Saving

Once prepared the Fit Ellipse measurement tool is selected and every tenth image in the experimental recording is automatically analyzed. The experiments conducted by Mehri et al. included 1500 images. Therefore 150 images were analyzed per data set. From each data set tens of thousands of aggregates were analyzed. An ellipse is fit to each aggregate and the properties of its orientation, size and dimensions are saved in a csv file format. The csv file saves the data in terms of pixels, so the calibrated measurement used from Mehri et al. experiments, 0.27μm/pixel, is applied to obtain the measurements in μm [9].

Once the data is obtained from the Niazi et al. algorithm a MATLAB code is used to create histograms of each individual data set. The MATLAB code creates three histograms per data set. They display the normalized semi-minor axis of each aggregate ellipsoid (b) normalized over a_c the average size of the specimen's RBC radii (2.75μm and 2.44μm for humans and porcine samples respectively), the axis ratio (semi-major axis over the semi-minor axis), and the orientation angle of each of each aggregate. The data is then characterized using a probability density function. Size-histograms are fit with a Gamma distribution curve, angle-histograms are fit with a normal distribution in accordance to methods used by LMA.

2.1.2.4 Segmentation Analysis

The size distribution of aggregates is assumed to follow a Gamma distribution in accordance with practices followed by the research at the LMA. Previous studies have shown that a Gamma PDF distribution is a good representation of the aggregate size [125] using a spherical model. De Monchy et al. further hypothesized that a Gamma PDF could be suitable for even the most complex cases. LMA's computer simulations use the Gamma distributions of aggregate size from the optical image segmentation of RBC aggregates [67], [125]. The following equation represents the Gamma PDF ($p_{z,\varphi}(x)$):

$$p_{z,\varphi}(x) = \frac{1}{\Gamma(z)\varphi^z} x^{z-1} e^{-\frac{x}{\varphi}} \tag{2.1}$$

Where z is the shape parameter, and φ is the scale parameter. The effects of varying z and φ can be seen in Figure 2-7.

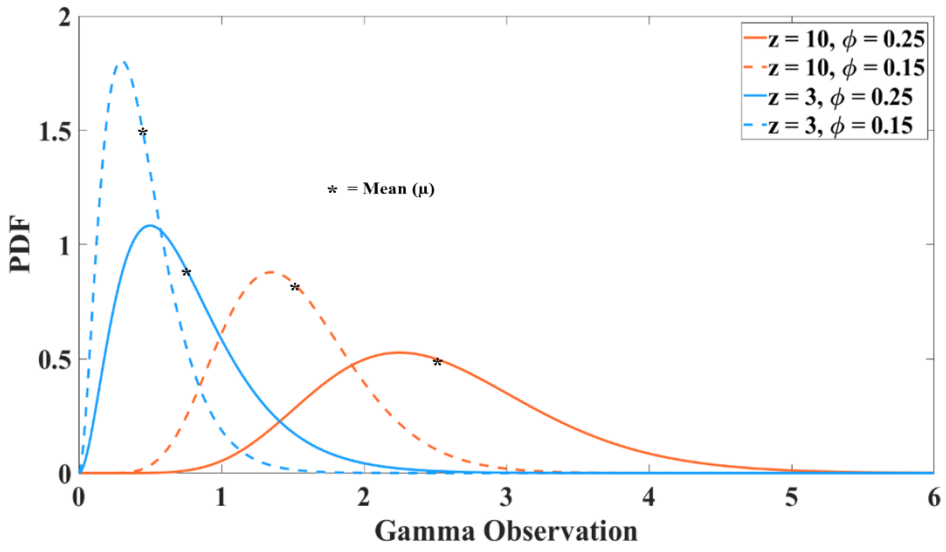

Figure 2-7: *Gamma PDF distribution presented at different z and φ (phi) values to emphasize the effects of the shape and scale parameters respectively.*

The mean is represented by μ, and can be calculated by the following equation;

$$\mu = z\varphi \tag{2.2}$$

Where changes in z and φ directly effect the mean. Changes in z alter the overall shape of the distribution curve while changes in φ correspond directly to the distribution spread. For example, larger scale parameter results in a more spread out distribution.

2.2 Microfluidic Device Fabrication and Compliant Characterization

Comparing the compliance of optical glue NOA to the gold standard material for microfluidics (PDMS) is done by measuring the characteristic time for each material in a microfluidic flow system. The details for manufacturing the microfluidic chips is given in subsection 2.2.1 whereas the experimental setup and analysis are explained in subsection 2.2.2 and 2.2.3, respectively.

2.2.1 Manufacturing

NOA63 and NOA81 were both considered, as they were both used in previous studies as microfluidic device materials [100], [101]. NOA63 was chosen due to its increased viscosity and low shrinkage [100], [101].

2.2.1.1 SU-8 Wafer

The stamp used for the replica molding of PDMS chips was made with SU-8 photoresist patterned on 3 inches silicon wafer. After Piranha solution cleaning (mixture of H_2SO_4 and H_2O_2), and nitrogen drying, a thin layer of SU-8 2050 (Kayaku Advanced Materials, Inc.) was manually poured on the surface of the silicon wafer and spin coated at 3000 rpm for 30s. During spin coating, PGMEA (Propylene glycol methyl ether acetate) developer was spread on the side of the wafer to prevent the formation of edge beads. After soft baking at 95°C, with a slow temperature ramp up and down, the wafer was exposed to UV light through a photomask at 150mJ/cm^2 at 365nm using a lithography aligner and a UV 365nm bandpass filter. The silicon wafer was then post baked at 95°C using a slow temperature ramp and then developed in PGMEA, rinsed with Isopropyl alcohol, and hard baked at 130°C for several minutes. The mask used for SU-8 structures imprint is positive, e.g. the opposite of classical negative masks used to create microchannels by PDMS replica molding, as shown in Figure 2-8.

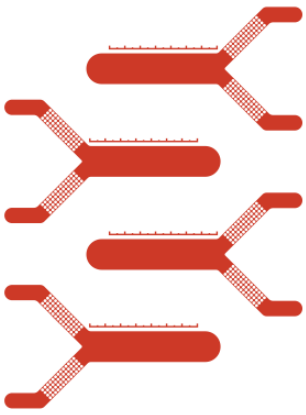

Figure 2-8: *Mask used for SU-8 structures to make the PDMS stamp.*

The resulting SU-8 structures are made mostly of SU-8 including holes inside a regular layer. The same PDMS master was obtained from double molding with a classical SU-8 wafer following the silanization steps presented in section 2.2.1.3.

2.2.1.2 NOA Device

NOA devices are manufactured using a patterned silicon stamp. The manufacturing method of the NOA63 microfluidic devices is adapted from the technique presented by *Sim, Jae Hwan et al.*[99]. The details of the manufacturing method of the NOA device are presented in Figure 2-9.

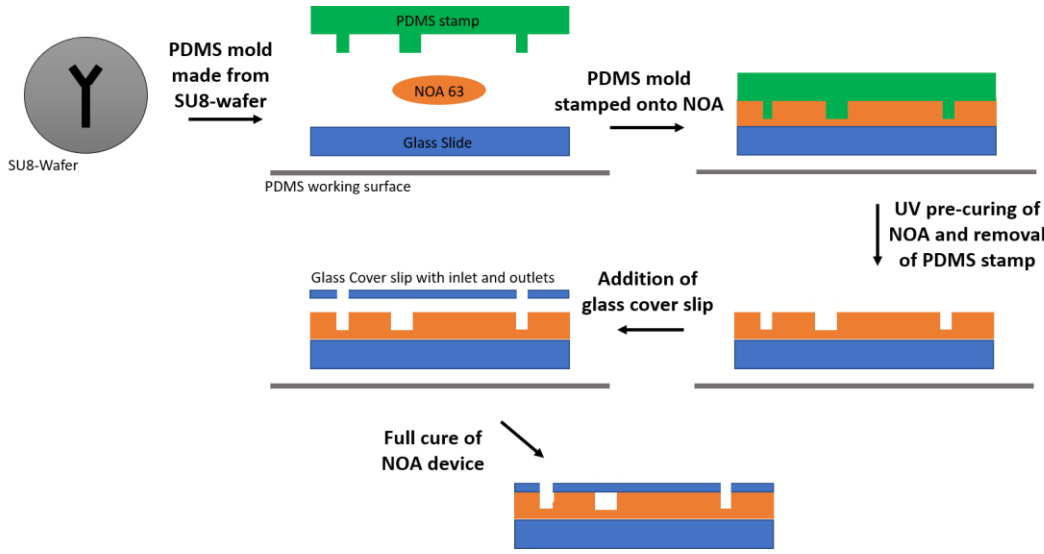

Figure 2-9: *Schematic layout of the NOA device manufacturing method using NOA 63. NOA microfluidic chips require a PDMS master of the channels to use as a stamp which is taken from the patterned wafer. The PDMS mold is then slowly placed down on top of the NOA. The NOA is precured using UV light of 365nm wavelength and 23.1mW/cm^3 intensity. The PDMS master is then peeled off and the remaining NOA becomes an inverse replica of the PDMS stamp. A glass cover slip with the appropriate inlet and outlet holes, is placed on top of the precured NOA chip. The NOA chip is then fully cured for two hours under the UV light.*

A 1.25cm diameter circle of NOA63 is dispensed onto a standard glass slide. The PDMS stamp generated from the SU-8 wafer is used to manually stamp the uncured NOA63. The stamped NOA63 is then placed under 365nm wavelength UV light, of intensity 23.1mW/cm^2, for 20s causing the glue to stay in a precured state for a total energy exposure of 40mJ/cm^2. Therefore, the stamped channels are retained by the NOA. The PDMS stamp is removed from the NOA and a glass cover slip is placed, and aligned, on top of the precured NOA. A cover slip with laser cut holes for the appropriate inlet and outlet ports is prepared using a CO_2 laser etching machine (*Epilog Laser)*. The etching machine was set to a speed of 80% and a power of 85%. The coverslip was secured to a wooden surface and five laser shots were used to create the inlet and outlet holes. Once aligned atop the precured NOA63, the entire NOA63 device is placed under UV light at an intensity of 23.1mW/cm^{2}and a wavelength of 365nm for 2 hours for a total energy exposure of

144J/cm^2. Pieces of PDMS are pre-punched at an 18-gauge diameter and plasma bonded onto the glass coverslip, completing the NOA device. This allows common inlet systems to be utilized. A completed NOA device is depicted in Figure 2-10.

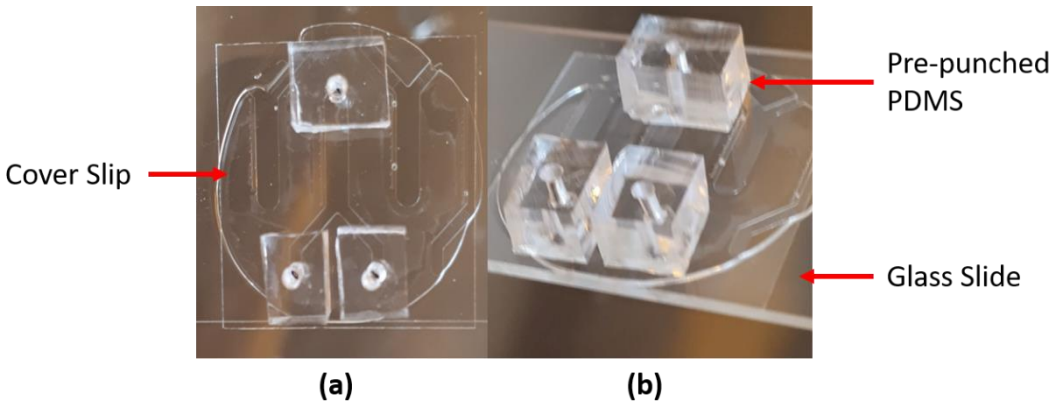

Figure 2-10: *Example of final version of the NOA microfluidic chip including the plasma bonded inlets and outlets of PDMS. a) Top view of the chip. b) Isometric view.*

2.2.1.3 PDMS Device

The PDMS devices were manufactured using the same patterned SU-8 wafer as the NOA devices to ensure that the channels are homogenous. The manufacturing process for the PDMS microfluidic devices is detailed in Figure 2-11.

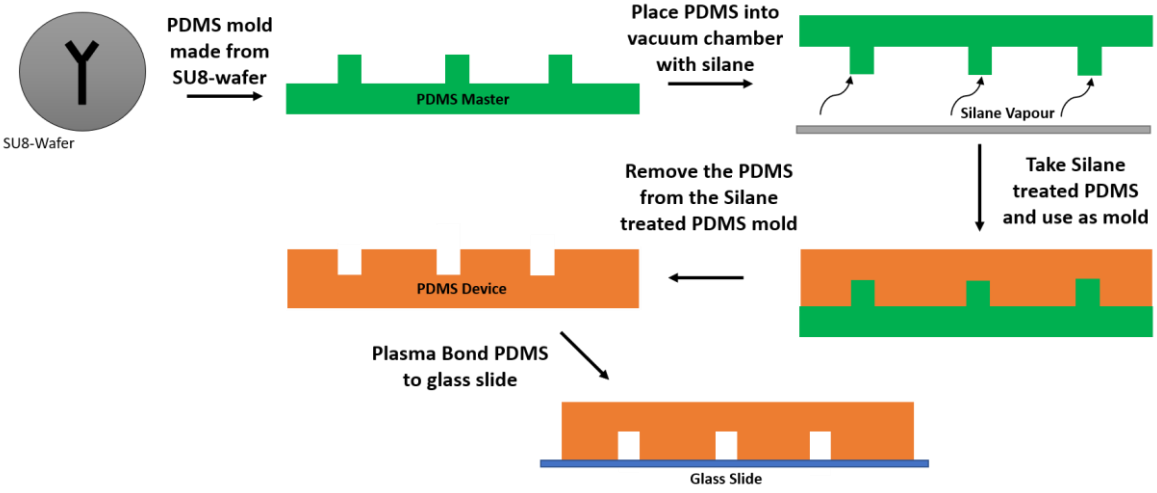

Figure 2-11: *Schematic layout of the PDMS device manufacturing method using a PDMS master. A PDMS master is created using a 5:1 ratio of the main agent and the curing agent thus creating a harder PDMS mold [126]–[128]. The mold is used as a master and is treated by vaporizing trichloro (1H, 1H, 2H, 2H-perfluorooctyl) silane (PFOTS) in a vacuum [129]. This causes a small film of PFOTS to be left on the surface of the PDMS which can then be used as its own mold for manufacturing PDMS devices with correctly orientated channels from the initial PDMS master.*

Using a silanization process, the PDMS master molded from the SU-8 wafer was used to fabricate the PDMS device. The PDMS-PDMS replica molding was adapted from *Zhuang et al.* [129]. The PDMS master is created using a PDMS 5:1 mixture of main agent and curing agent, respectively. The PDMS master is thus, identical to the PDMS stamp used in section 2.2.1.2 but with different mechanical properties [126]. This creates a harder PDMS master allowing the PDMS to act as a more effective mold during the silanization process [126]–[128]. The harder PDMS master is placed in a vacuum chamber, directly above 2 drops of trichloro (1H 1H 2H 2H-perfluorooctyl) silane (PFOTS). The PDMS master is de-gassed for 15-20min causing the PFOTS to create a thin layer over the PDMS surface. The PDMS master is then placed on a hot plate for 10min at 150°C, before being transferred into a pool of de-ionized water for 10min to remove any excess silane (PFOTS) that may remain on the PDMS master. It can then be used as a mold for the PDMS device by using a traditional 10:1 ratio of main agent to curing agent, typically used in microfluidic devices [128]. The 10:1 ratio is then poured on top of the PDMS master and heated at 75°C for 1hr. The PDMS device is finally cut away from the PDMS master, inlet and outlet holes are pre-punched into the device, and it is plasma bonded to a glass slide. The completed PDMS device can be seen in Figure 2-12.

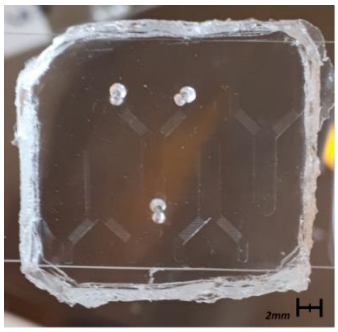

Figure 2-12: *Example of final version of the PDMS microfluidic device, shows the top view of the chip.*

2.2.1.4 Device Geometry Comparison

The NOA and PDMS devices were compared microscopically to confirm channel widths were maintained constant during manufacturing. Each channel was measured 10 times using ImageJ software and sample images of these measurements are displayed in Figure 2-13.

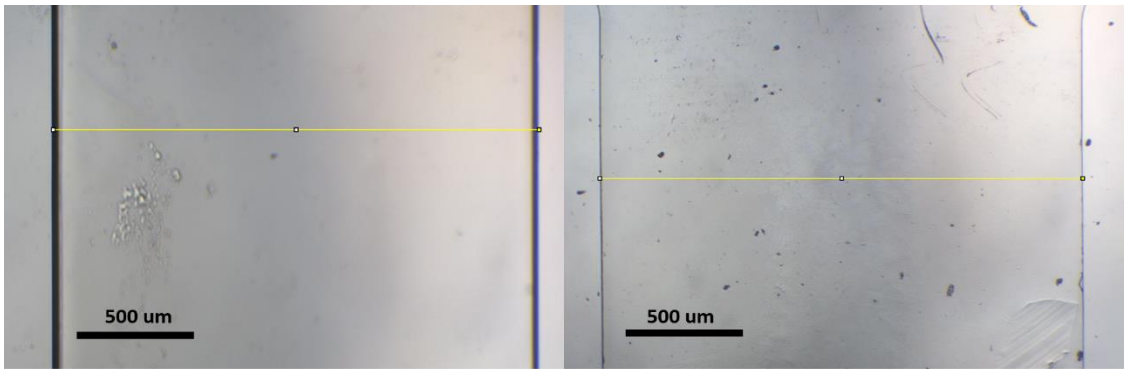

Figure 2-13: *Example of final version of the PDMS microfluidic device and the NOA63 microfluidic device both measured using a microscope at 4x magnification through a Zeiss camera of 5x magnification. a) Top view of the PDMS device. b) Top view of the NOA63 device.*

The mean channel width for the PDMS devices was 2.05mm ± 0.014mm while, the mean channel width for the NOA devices was 1.99mm ± 0.011mm. The PDMS channel width differs by 2.5%, while that of the NOA devices differs by 0.5% from the SU-8 wafer channel width. Both measurements were completed using 4x microscopic magnification through a Zeiss camera with a 5x magnification. The manufacturing processes of both devices were optimized to ensure proficient curing and bonding was achieved, and in particular, that no air bubbles or pockets were present in the microfluidic devices.

2.2.2 Experimental Setup

The flow system used to test the characteristic time for both devices consisted of rigid components with low compliant properties. These included 500µl *Hamilton* glass syringes, 18-gauge metal tubes, and small but rigid polymer tubing. All connections were secured with Teflon tape to ensure an airtight system. The glass syringes and rigid tubing materials were used to ensure that the system was as non-compliant as possible. This ensures that the flow system components, other than the microfluidic device, minimally affected the total compliance. A detailed flow chart of the experimental setup can be seen in Figure 2-14.

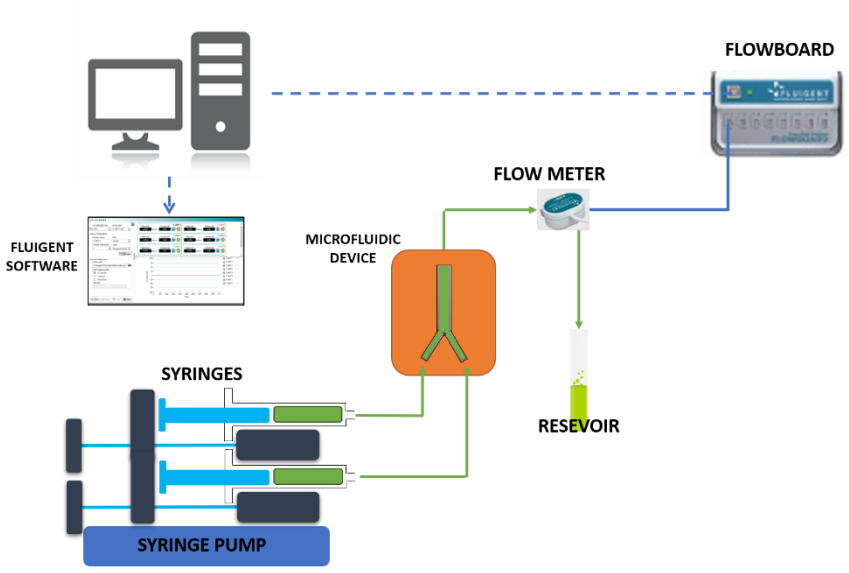

Figure 2-14: *Flow set up for the characteristic time testing of microfluidic devices. Setup includes a Chemyx Nexus 3000 syringe pump with two 500µl Hamilton glass syringes with 18-gauge metal tubes. All fluid runs through a rigid polymer tubing. After exiting the microfluidic device, the flow is directed into a Fluigent flow meter size S (small). The flow board takes the output from the flow meter and processes it visually through the Fluigent software resulting in a flow rate measured over time plot.*

The Chemyx Nexus 3000 syringe pump was set to accommodate flow rates of 10µl/hr, 25µl/hr, 50µl/hr, and 100µl/hr through the microfluidic device. A flow unit size (S) (Fluigent) was used to measure and record the flow rate over time as it exited the microfluidic device. This data was analyzed to calculate the characteristic time, and the process was repeated 3 times. A total of 16 microfluidic devices were tested; 8 PDMS devices and 8 NOA devices.

2.2.3 Analysis

The fluidic system was modelled using the Windkessel model in section 2.2.3.1 [18]. The data was collected from the Fluigent flow software and was processed using MATLAB software. This was done by fitting an exponential function, derived from the Windkessel model, to the flow rate over time plot as shown in section 2.2.3.2.

2.2.3.1 Windkessel Model

The flow of the system can be described by:

$$Q_{in} - Q_{out} = Q_c \tag{2.3}$$

where Q_{in} is the inflow to the system, controlled by the syringe pump. Q_{out} is the outflow of the system measured by the flowmeter, and Q_c is the rate of storage of the system itself. Q_c can be further described by:

$$Q_c = C\frac{dP}{dt} \tag{2.4}$$

where C is the compliance of the system and $\frac{dP}{dt}$ is the pressure change over time inside the system. This means the volumetric rate of storage of the system is directly related to the compliance of the system. Q_{out} can be defined, assuming Hagen-Poiseuille flow, as:

$$Q_{out} = \frac{\Delta p}{R_s} \tag{2.5}$$

where Δp is the drop-in pressure of the system, and R_s is the peripheral resistance. When the pressure at the outflow is assumed to be close to zero, it is reduced to the pressure within the storage chamber, p. Thus Equation *(2.3*), *(2.4*) and Equation *(2.5*) can be re-written as:

$$Q_{in} - \frac{p}{R_s} = C\frac{dp}{dt}. \tag{2.6}$$

Integrating to solve for $p(t)$ using initial conditions of $p = p_o$ (initial pressure) and $t = 0$ (time) the pressure can be written as:

$$p(t) = R_s Q_{in} - (R_s Q_{in} - p_0)e^{-\left(\frac{t}{R_s C}\right)} \tag{2.7}$$

where p_0 is the initial pressure and t is the time. From Equation *(2.7*) dp/dt can be rewritten as:

$$\frac{dp}{dt} = \left(\frac{R_s Q_{in} - p_0}{R_s C}\right)e^{-\left(\frac{t}{R_s C}\right)}. \tag{2.8}$$

Combining Equation *(2.8*), Equation *(2.4*) and Equation *(2.3*) the system equation can be rewritten as:

$$Q_{out} = Q_{in} - \left(\frac{R_s Q_{in} - P_0}{R_s}\right) e^{\left(-\frac{t}{R_s C}\right)} \quad (2.9)$$

where p_o is the initial pressure of the system, t is the time, and R_sC represents the characteristic time of the system.

2.2.3.2 Characteristic Time Extraction

The characteristic time of each trial is calculated and used to compare the compliance of the system. This is assuming that the resistance of the external system is constant and the only change in compliance from the system comes from the microfluidic device. All experimental outliers were removed using the Chauvenet Criterion [130].

The Outflow of the system, Q_{out} (which is a function of time t), can then be modelled using the following equation:

$$Q_{out} = A - Be^{-(t-t_0)D}. \quad (2.10)$$

The four constants are used to fit the raw data, acquired experimentally, from Equation *(2.9)*. The constant A represents the Q_{in}, the constant B represents the maximum rate of storage, t_0 is a correction factor for the time variable, and the constant D is the inverse of the characteristic time of the system.

2.2.3.2.1 Characteristic Time Simulation

To illustrate how the characteristic times between PDMS and NOA differ to a greater magnitude for small channel cross-sectional areas, a simulation of more traditional microfluidic dimensions was developed. Initially, compliance for each material is calculated using the resultant expression, as follows:

$$C = \frac{\tau}{R_s} \quad (2.11)$$

Where C is compliance, τ is the characteristic time experimentally found for PDMS or NOA using Equation *(2.3*) to Equation *(2.10*), and R_s is the estimated total resistance based on the geometry of the microfluidic device. Next the Compliance factor (CF) was computed as follows:

$$CF = \frac{C}{V} \tag{2.12}$$

Where V is the total estimated volume of the chip. The CF can then be used to calculate different characteristic times of different PDMS and NOA devices with alternate geometries by estimating the resistance and volumes of said devices. Four different geometries were simulated using the CF. Estimations of the geometric volume and hydrodynamic resistance values were calculated. Circular cross section hydrodynamic resistance was calculated using the following equation:

$$R_h = \frac{8\mu L}{\pi R^4} \tag{2.13}$$

Where R is the radius of the cross-section, μ is the viscosity of the fluid, and L is the length of the channel in question. Rectangular cross sections have the following equation for hydrodynamic resistance:

$$R_h = \frac{12\mu L}{wh^3(1 - \frac{0.63h}{w})} \tag{2.14}$$

Where h is the height of the channel and w is the width of the channel. The four different geometries simulated are outlined in Table 2-2, where *a* is a variable used to control overall size of the cross-sectional area. The characteristic time of the various device geometries are calculated by re-arranging Equation *(2.12*) and Equation *(2.11*) as follows:

$$\tau = CF * R_s * V \tag{2.15}$$

where CF is the compliance factor, Rs is the calculated resistance for the specific geometry in question, and V is the estimated priming volume of that device. A total of 8 expressions for time constants, 4 for PDMS and 4 for NOA are derived and plotted against variable *a* to develop the simulations of time constants in terms of geometry.

Table 2-2: *Set dimensions for geometric cross-sectional areas (A, B, C, D) in terms of variable a.*

A (square)	**B (rectangle)**		**C (rectangle)**		**D (circle)**
height and width [m]	height [m]	width [m]	height [m]	width [m]	radius [m]
a	a	2a	a	5a	a

2.3 Flow Properties and Calibration of Microfluidic Device

Analyzing the flow properties characterized by the NOA microfluidic device was done using µPIV techniques to obtain the velocity profile for various blood solutions. The velocity profile in the blood layer of sheared flow within the co-flow system was analyzed to acquire the shear rate. The setup used was comparable to the microfluidic setup as seen in chapter one of this report, section 1.2.3.2. Details of the sample preparation, experimental setup, µPIV setup, high speed camera and shear analysis procedures can be found in subsection 2.3.1, 2.3.2, 2.3.3, 2.3.4, and 2.3.5 respectively.

2.3.1 Sample Preparation

Samples of human blood were prepared using different concentration of Dextran 70 and Dextran 500 in order to induce RBC aggregation. A total of 7 testing samples were prepared. They are outlined in Table 2-3. Details on the sample parameters can be found in the following subsections.

Table 2-3: *Overview of samples and their constituents.*

Sample #	*Blood (%)*	*PBS (%)*	*OptiPrep (%)*	*Dextran 70 (g/100ml)*	*Dextran 500 (g/100ml)*	*Sample Size Total Volume (ml)*
1	10	68.5	31.5	0	2	5
2	10	68.5	31.5	0	1.5	5
3	10	68.5	31.5	0	1	5
4	10	68.5	31.5	3.5	0	5
5	10	68.5	31.5	3	0	5
6	10	68.5	31.5	2.5	0	5
7	10	68.5	31.5	0	0	5

2.3.1.1 Fluids

Each sample contained 68.5% Phosphate Buffered Saline (7.4 pH) and 31.5% OptiPrep by volume. OptiPrep is a density gradient medium which prevents RBCs from settling in the solution allowing for prolonged experimental procedures. OptiPrep has a density of 1.32g/ml while the density of blood and PBS is 1.125g/ml and 1.01g/ml respectively. The addition of 31.5% OptiPrep brings the solutions overall density closer to the blood's density. The PBS was a 1x solution prepared using PBS tablets and de-ionized water. PBS is used to maintain RBCs in homeostasis preventing ion diffusion across the cell membrane. PBS and

OptiPrep have an osmolarity of 288 mOsmol/L and 170 mOsmol/L respectively, while human plasma has an osmolarity of 275-285mOsmol/kg. The mixture of PBS and OptiPrep proposed allows for the osmolarity of the solution to fall withing the 275-285mOsmol/kg range, thus preventing inflation, which could lead to hemolysis or crenation of the cells.

2.3.1.1.1 Solution Preparation

The solutions prepared contain varying amounts of Dextran 70 or Dextran 500 concentrations. To achieve the proper concentration values a two-step dilution method was used as outlined in Table 2-4.

Table 2-4: *Solution preparation based on a two-step dilution method.*

Name	**PBS (ml)**	**Glucose (mg)**	**OptiPrep (ml)**			
Base Solution	23.45	315	11.55ml			
Name	***Amount of Base Solution (ml)***	***D500 (g)***	***D70 (g)***			
Dilution 1	12	0.24	N/A			
Dilution 2	12	N/A	0.42			
Name	***Amount of Base Solution (ml)***	***Amount of Dilution 1 (ml)***	***Amount of Dilution 2 (ml)***	***Dextran 70 (g/100ml)***	***Dextran 500 (g/100ml)***	***Final Volume (ml)***
Sample 1	0	5	0	0	2	5
Sample 2	1.25	3.75	0	0	1.5	5
Sample 3	2.5	2.5	0	0	2	5
Sample 4	0	0	5	3.5	0	5
Sample 5	0.71	0	4.29	3	0	5
Sample 6	1.43	0	3.57	2.5	0	5
Sample 7	5	0	0	0	0	5

Each solution has a final volume of 5ml, with varying levels of Dextran concentrations. The Dextran concentrations were selected based on the experiments being executed in LMA, in accordance with studies of polymer induced RBC aggregation [1], [131].

2.3.1.1.2 Blood Preparation

Blood samples were collected from willing and self-declared healthy volunteers, according to the approval of the ethics committee of the University of Ottawa (H-03-19-3441). Three coded EDTA test tubes (4ml each) were obtained from the volunteer and centrifuged four times at 3000rpm for 10mins using

a centrifuge. The first centrifuge of the blood allowed the removal of plasma and WBC's from the sample by separating the blood into its constituents. PBS was then used to wash the blood three times. Once washed, the whole blood hematocrit was verified, and sample volumes were adjusted accordingly. The whole blood was measured using a glass capillary tube and a micro-centrifuge (CritSpin, Thermo Fisher Scientific, China).

The proper amount of RBCs were added to create a 2ml solution of each of the 7 solutions described in Table 2-3, in accordance to sample volumes seen in Table 2-4. By volume, 30µl/ml of fluorescent tracer particles were added to each sample. The fluorescent particles allow for velocity measurements through µPIV. All experiments were performed and completed within 48hrs of blood acquisition.

2.3.2 Experimental Setup

The experimental setup used consisted of a µPIV system (LaVision's MITAS), a high-speed camera system (Graftek Imaging, Inc., Austin, TX, USA), and a fluid flow system. The µPIV system included a New Wave Solo-II Nd:YAG laser (New Wave Research, USA) emitting a wavelength of λ emission equal too 532 nm, a Charged-Coupled Device (CCD) Imager Intense camera (LaVision GmbH, Germany), and a MITAS inverted microscope (LaVision GmbH, Germany) with a 10X lens magnification. The µPIV setup has a moving stage (x, y, z) placed on top of the inverted microscope that allows for movements of as little as 1 µm steps. The stage can be controlled through the DaVis Imaging Software (LaVision GmbH, Germany). The high-speed camera system is controlled via a LabVIEW software (National Instruments, USA). The flow system is controlled by two syringe pumps (Nexus3000, Chemyx Inc., USA) flowing at ratios of 25:1 in relation to each other. The syringe pumps are controlled through a serial port connection using PuTTY software. Two Hamilton glass syringes (Hamilton, USA) of 1ml and 250µl in size, by volume, are used. These syringes are connected to the NOA microfluidic device using rigid tubing. The NOA microfluidic device contains a Y channel with main channel dimensions of 2000µm (width) x 63µm (depth). Fluorescent tracer particles are added to the samples, diluted at 1% in water (dp = 0.79 µm, λabs = 542 nm

and λemission = 612 nm). These fluorescent particles are necessary for velocity measurement with the μPIV system. Figure 2-15 highlights the experimental setup used.

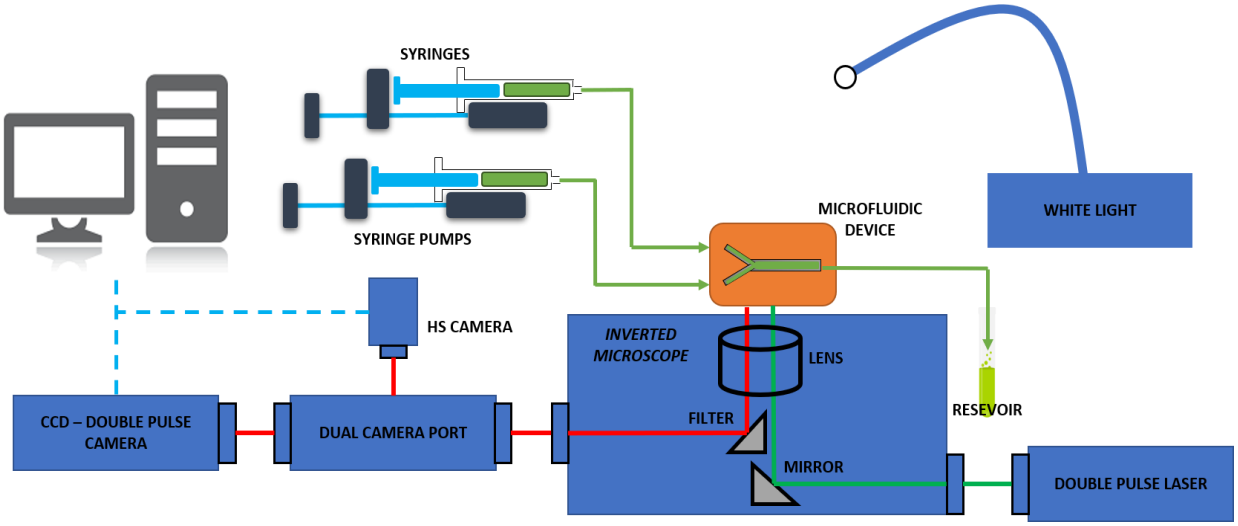

Figure 2-15: *Co-flow set up used to analyze velocity profile in NOA microfluidic device.*

2.3.2.1 Flow Settings

The co-flow settings used for the experimental setup shown in Figure 2-15 are given in Table 2-5.

Table 2-5: *Flow rate settings used to shear blood samples.*

Base Flow Ratio	***Flow Factor***	***Sheared Flow (Blood Flow Rate) (μl/hr)***	***Shearing Flow (PBS Flow Rate) (μl/hr)***
25:1	0.1	25	1
	0.2	50	2
	0.4	100	4
	0.8	200	8
	1	250	10
	2	500	20
	4	1000	40
	8	2000	80
	16	4000	160
	30	7500	300

A blood sample is loaded into the 250μl Hamilton glass syringe. The 1ml Hamilton glass syringe is then filled with PBS at 1x concentration. The syringe pumps are set using the serial port connection through PuTTY software. The flow ratios used are obtained from the base flow ratio in Table 2-5 of 25:1. The flow rates used are obtained by multiplying that ratio by the flow factors in Table 2-5. This creates a co-flow

system, thus allowing the ability to control RBC aggregation through varying the shear conditions. Each sample uses the flow rates in Table 2-5 once each, thus obtaining 10 separate velocity profiles for analysis.

2.3.3 µPIV Setup

The components of the µPIV setup are shown in Figure 2-15. The blood samples are viewed normal to their flow direction allowing for a 2D representation of the velocity profile. The laser beam, emitted from the New Wave Solo-II Nd:YAG laser, is filtered when it enters the MITAS inverted microscope allowing for a certain range of wavelengths to pass. The laser beam then encounters a dichroic mirror which deflects the beam upwards towards the NOA microfluidic device. The fluorescent tracer particles within the sample come into contact with the laser beam, causing them to emit light. The light produced passes through the emitter in the filter cube and is recorded by the CCD camera. The CCD camera can record 100 paired images at a rate of 5MHz. The spatial resolution of the CCD camera is 10 x 10µm^2 per pixel with 0.57 µm/pixel when using the 10x magnification lens. The LaVision image intense camera has high sensitivity and low read out noise. The CCD camera and the high-speed camera are separated via a camera dual port. The camera dual port dictates the light path used by the cameras. This is essential since the highspeed camera uses white light.

2.3.3.1 Velocity Measurement

Velocity measurements are obtained by averaging the 100 image pairs recorded through the CCD camera using cross-correlation methods at the microscale. This process is done using the DaVis Imaging software. The software allows for control of CCD and laser settings during data acquisition, as well as post processing procedures. The time between laser pulses, dt, was set using the automated dt function in the DaVis software. The software was able to recognize a pixel displacement of around 5 allowing for accurate instantaneous velocity measurements of the flow. Three areas of interest were used to calibrate the automated dt, all of which were placed within the blood layer of the flow.

Post processing of the images was also completed using the DaVis software. The 2D velocity field was obtained using a multi-pass cross correlation method over the CCD images as seen in Figure 2-16.

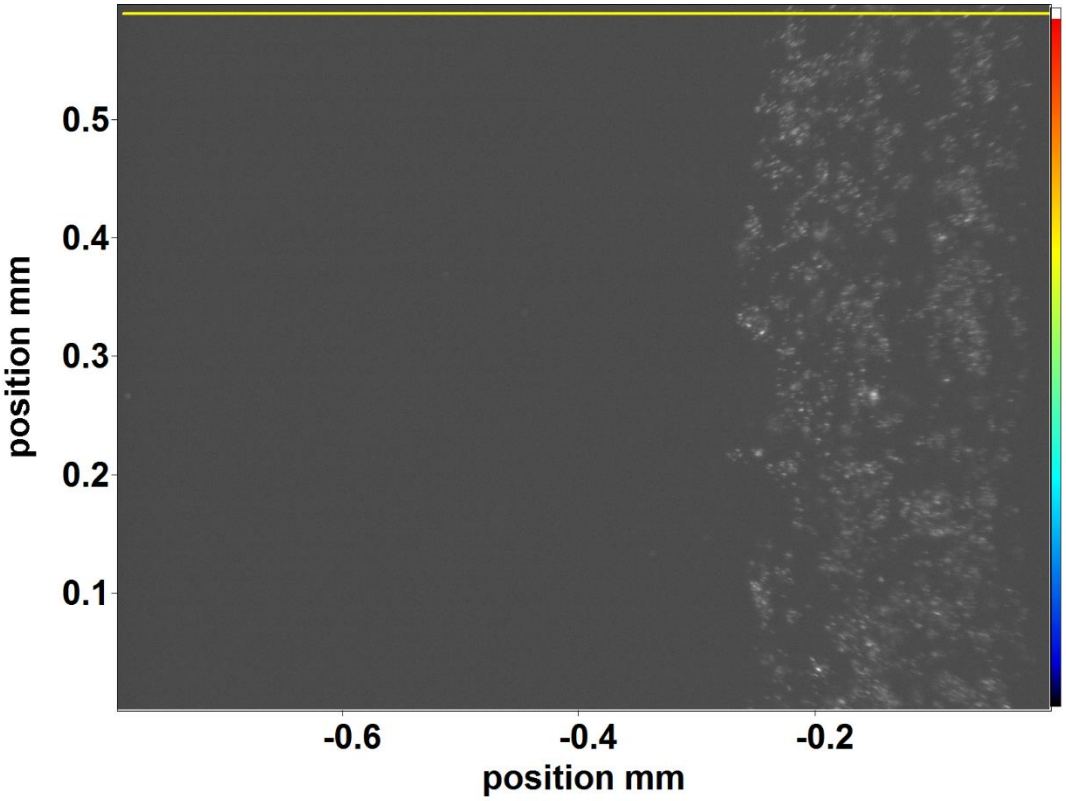

Figure 2-16: *Example of image from the CCD of D500(1.5g/100ml) at a flow factor of 8. Fluorescent particles presented in the blood layer can been seen in the right side of the picture.*

The correlation window started at a size of 64 x 64, decreasing to a size of 32 x 32. The overlap of the windows was set at 60% for each pass. The correlation windows were oval shaped and were weighted at a 4:1 ratio in the x-direction. For each set of 100 images an average velocity vector field was created as seen in Figure 2-17.

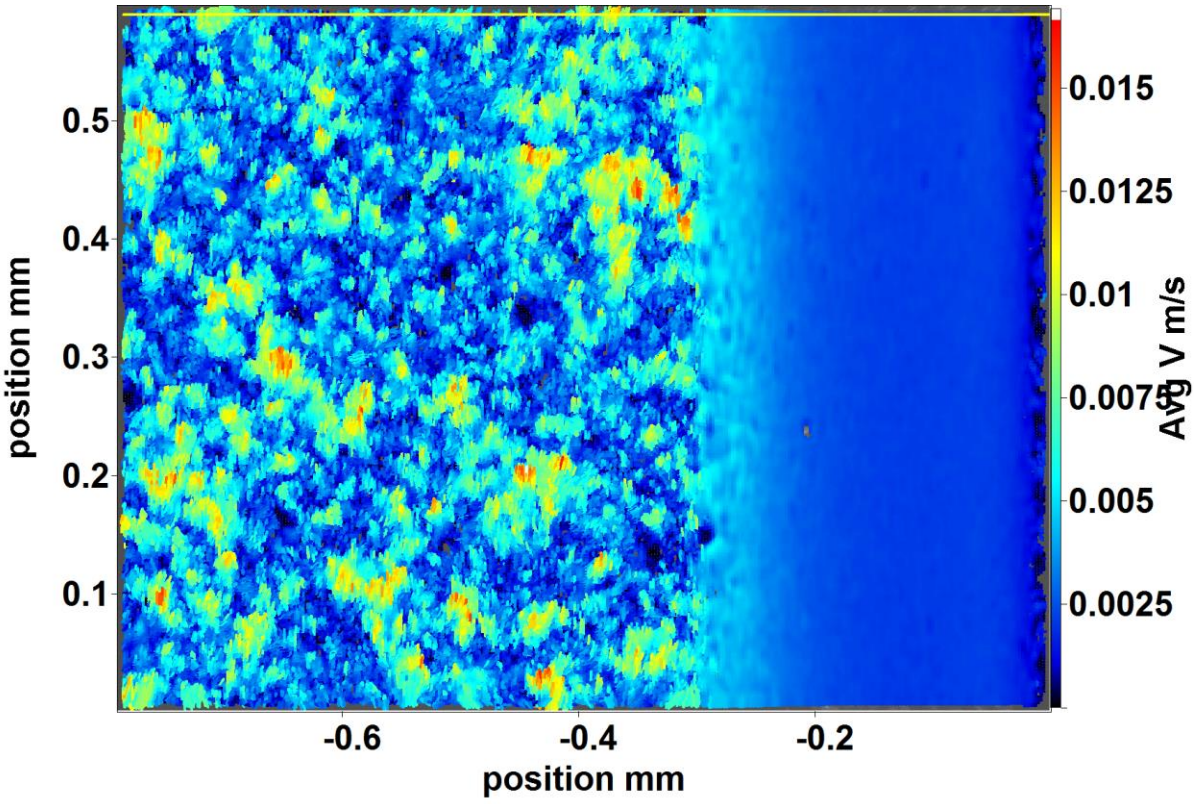

Figure 2-17: *Velocity vector field of the D500(1.5g/100ml) sample flowing at flow factor 8 (Sheared blood flow at 80 µl/hr. The left part with no particle presents noise, where the right part the color represents the velocity of the fluorescent particles.*

2.3.4 High Speed Camera

The high-speed camera was used to capture the RBC arrangements. The recording clarity is based on the frame rates and field of view of the camera. At maximum field of view allowed by the high-speed camera (resolution of 5.5 by 5.5 μm^2 per pixel, 0.53 µm/pixel with 20x magnification), the highest frame rate possible is 340 frames/s. The camera system is controlled by a LabVIEW program. The exposure time, frame rate and field of view can be altered through the software.

2.3.5 Shear Analysis

The shear rate of each trial is verified through the analysis of the velocity profile, acquired through the µPIV system. The blood layer in the flow is sheared by the faster flow which is the PBS, creating a pseudo-linear velocity profile across the blood layer as seen in

Figure ***2-18***.

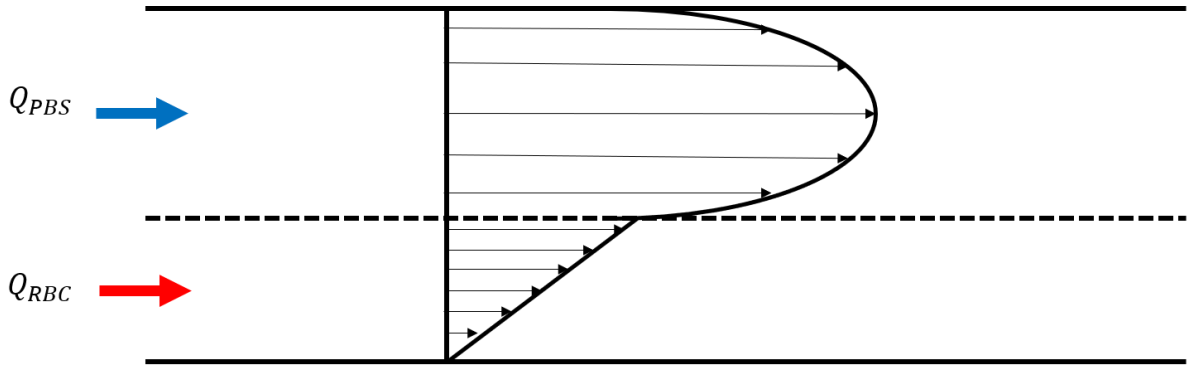

Figure 2-18: *Velocity profile produced in the co-flow system presented.*

This creates a pseudo-linear velocity profile in the blood layer between the wall (Ywall) and the PBS interface (Yint). To quantify the shear at each trial from Table 2-5, the following equation was used;

$$\dot{\gamma} = \frac{du}{dy} \tag{2.16}$$

Where $\dot{\gamma}$ is the shear rate, du is the change in velocity across the blood layer, and dy is width of the blood layer. An example of this measurement can be seen in Figure 2-19, using Equation *(2.16)*.

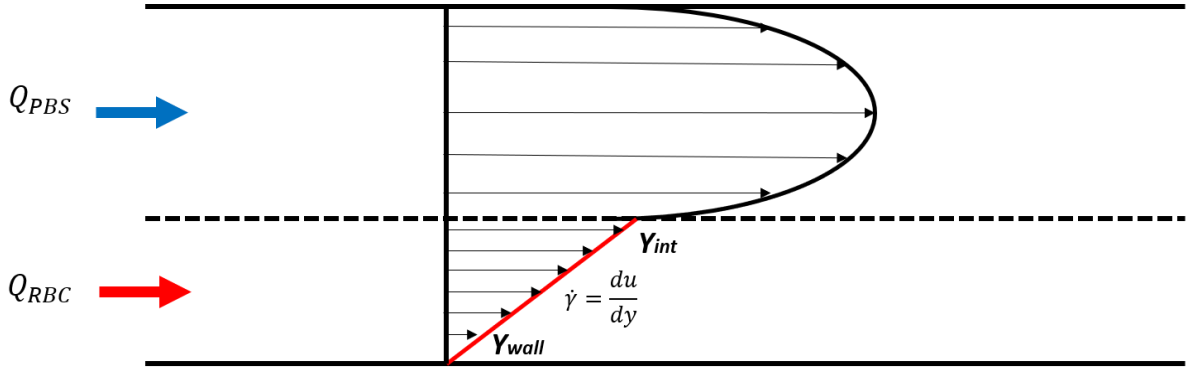

Figure 2-19: Example acquisition of shear rate from pseudo-linear velocity profile of blood layer.

When analyzing the velocity profiles a MATLAB program was used and the area close to the channel wall was neglected. This area (0.05mm) was neglected consistently in all trials due to inaccurate measurements from the µPIV system and probable cell-free-layer (region with lack of RBC) [9].

Chapter 3

3 Results

This chapter outlines the results obtained from all experimental and analytic procedures including the aggregation characterization methodology, the microfluidic device compliant characterization, and the shear rate calibration of the microfluidic device.

3.1 Aggregation Characterization

The quantitative aggregation data acquired from the Mehri et al. porcine experiments were analysed. The resulting histograms present aggregation distribution of the normalized size of the semi-minor axis of the ellipsoidal model, the axis ratio between minor and major axis of the ellipsoid, and the orientation angle of the ellipsoid (Methodology 2.1.2). Data is modeled using probability density functions (PDF). The distribution was considered a Gamma distribution for the size of the normalized semi minor axis and the axis ratio, and a Gaussian distribution for the orientation angle (Methodology 2.1.2.4). Figure 3-1 gives examples of a set of histograms and PDFs obtained for a test from the Mehri et al. data set.

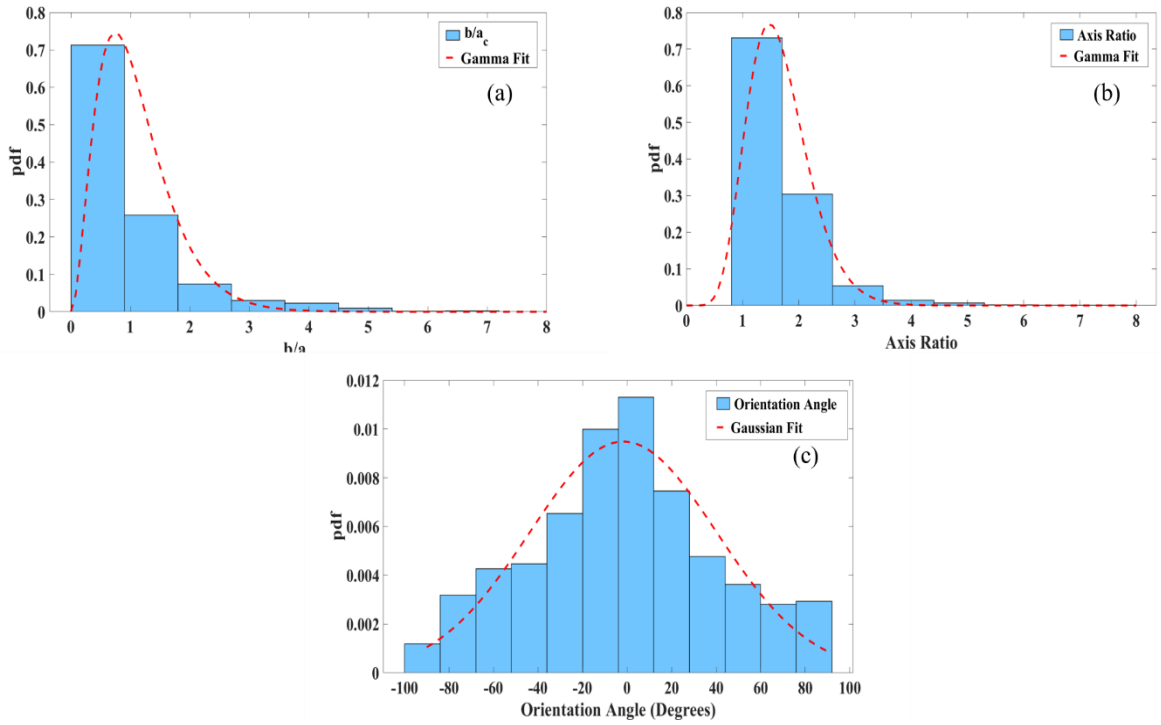

Figure 3-1: *Histogrmas of (a) the normalized minor axis, b, over the normalization value a_c, (b) the axis ratio (major over minor axis), (c) the orientation angle of the ellipsoids. All histograms are presented with a probability density function (Gamma for (a) and (b); Normal for (c)) and a fitted curve (red) in accordance to the distribution. All data taken from PIG 3 at a flow rate of 10µl/hr by Mehri et al.*

Similar histograms from those of Figure 3-1 were obtained for each test with each flow rate up to 240µl/hr. The histograms were then fit to a Gamma or Gaussian distribution, respectively. The quantitative results of this comparison, including the mean (Equation *(2.2)*), shape parameter (Equation *(2.1)*), and scale parameter (Equation *(2.1)*), are displayed in the following tables: Table 3-1, Table 3-2, and Table 3-3. The raw data comprises the blue area of the histogram and the fit data refers to the Gamma or Gaussian line of best fit. All the data collected from the multiple tests were averaged for a fixed flow rate. Table 3-1 shows the average from each flow rate regarding the normalised minor axis (b/a_c) tested for each specimen.

Table 3-1: *Fitted quantitative results from each minor axis (b/ac) histogram from all blood samples in Mehri et al. experiments.*

	PIG 1				
	Gamma Fit				
Flow Rate (µl/hr)	**Number of Tests**	**Shape z**	**Scale φ**	**Mean µ**	**STD**
Q20	*3*	3.0	0.30	0.91	0.53
Q30	*3*	4.0	0.24	0.95	0.48
Q60	*3*	3.9	0.25	0.98	0.50

Q120	*5*	5.4	0.17	0.90	0.39
Q240	*6*	6.7	0.12	0.80	0.31
[redacted]	**PIG 2**				
	Gamma Fit				
Flow Rate (µl/hr)	**Number of Tests**	**Shape z**	**Scale φ**	**Mean µ**	**STD**
Q7.5	*3*	3.6	0.35	1.3	0.66
Q10	*6*	2.7	0.39	1.1	0.65
Q20	*7*	2.4	0.41	0.98	0.63
Q30	*7*	3.0	0.30	0.90	0.52
Q60	*6*	3.5	0.23	0.81	0.43
Q120	*6*	3.9	0.18	0.72	0.36
Q240	*6*	5.1	0.13	0.65	0.29
[redacted]	**PIG 3**				
	Gamma Fit				
Flow Rate (µl/hr)	**Number of Tests**	**Shape z**	**Scale φ**	**Mean µ**	**STD**
Q10	*9*	3.0	0.36	1.1	0.62
Q20	*8*	4.2	0.26	1.1	0.53
Q30	*5*	6.2	0.15	0.93	0.37
Q60	*1*	5.4	0.17	0.92	0.40
Q120	*6*	7.6	0.11	0.84	0.30
Q240	*4*	8.5	0.091	0.77	0.27
[redacted]	**HUMAN**				
	Gamma Fit				
Flow Rate (µl/hr)	**Number of Tests**	**Shape z**	**Scale φ**	**Mean µ**	**STD**
Q10	*3*	4.6	0.25	1.1	0.53
Q20	*2*	4.7	0.21	0.98	0.45

From the data in Table 3-1, the mean size of *b* tends to decrease, with minor deviations, as the flow rate increases. This suggests that the semi-minor axis of the aggregate ellipsoid decreases in size when the flow rate increases. This can be seen more clearly in

Figure 3-2. The standard deviation (STD) between the multiple tests of each flow rate decreases with the lowest STD's for each specimen calculated at the largest flow rate of 240µl/hr (Pig 1 ±0.31, Pig 2 ±0.29, Pig 3 ±0.27), or 20µl/hr for the human specimen (±0.45). An increase in the shape parameter occurred from low flow rates to high flow rates as depicted in Figure 3-3. The fitted shape parameter z ranged from around 3.0 to 8.5. The scale parameter φ tended to decrease from low flow rates to high flow rates as seen in Figure 3-3. Recorded scale parameters of the Gamma pdf ranged from 0.360 to 0.091. This increase in shape parameter z and decrease in scale parameter φ suggest the spread of the distribution is reduced at higher flow rates. This infers a higher percentage of aggregates with the size of the semi minor axis reduced. This could suggest that aggregates elongate in faster flow rates through a decrease in the semi-minor axis length.

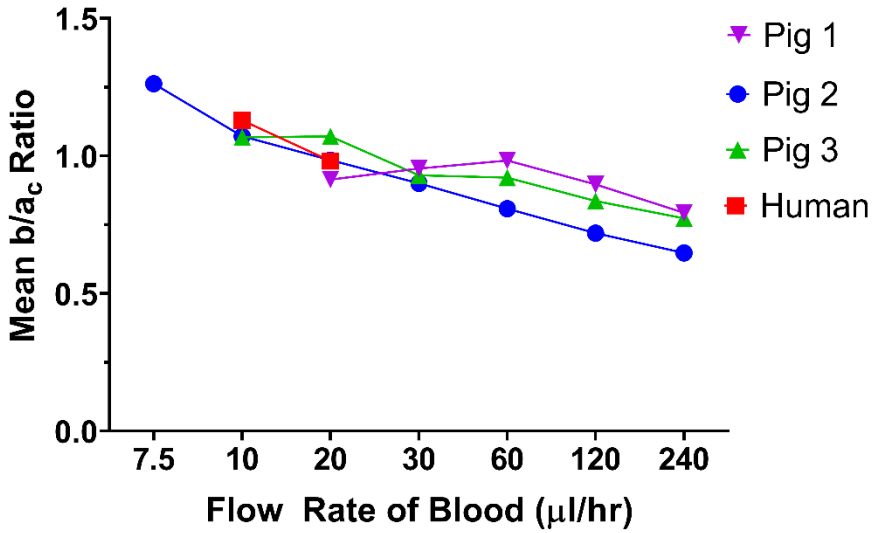

Figure 3-2: *Mean size of the normalized semi-minor axis of the ellipsoid aggregate (b/a_c) from the fitted Gamma pdf displayed at varying flow rates for all four specimens in the Mehri et al. experiments.*

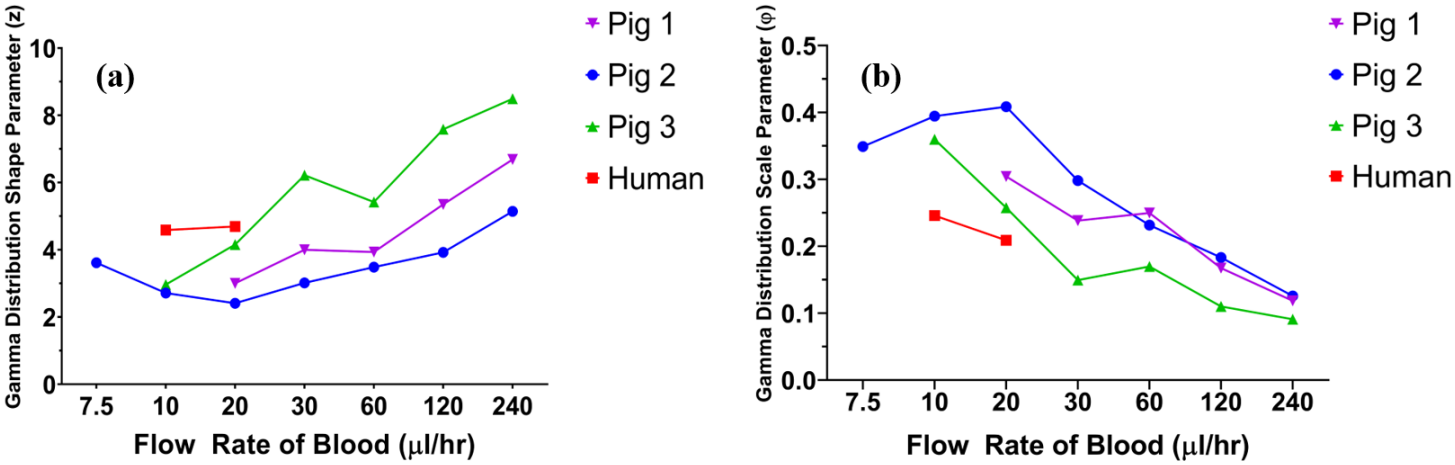

Figure 3-3: *Shape and Scale parameter of semi- minor Axis. (a) Z fitted Gamma pdf of the normalized semi minor axis, displayed as a function of flow rate used by Mehri et al. for all four specimens. (b) φ of the fitted Gamma pdf of the normalized semi minor axis, displayed as a function of flow rate used by Mehri et al. for all four specimens.*

Table 3-2 summarizes the average µ for axis ratio values at each flow rate for each specimen.

Table 3-2: *Fitted quantitative results from each axis ratio histogram from all blood samples in Mehri et al. experiments.*

	PIG 1				
	Gamma Fit				
Flow Rate (µl/hr)	**Number of Tests**	**Shape z**	**Scale φ**	**Mean µ**	**STD**
Q20	*3*	9.0	0.20	1.8	0.60
Q30	*3*	9.2	0.21	1.9	0.63
Q60	*3*	8.8	0.21	1.8	0.62
Q120	*5*	7.8	0.25	2.0	0.70
Q240	*6*	6.6	0.33	2.2	0.84
	PIG 2				
	Gamma Fit				
Flow Rate (µl/hr)	**Number of Tests**	**Shape z**	**Scale φ**	**Mean µ**	**STD**
Q7.5	*3*	9.4	0.19	1.8	0.60
Q10	*6*	11	0.15	1.6	0.50
Q20	*7*	7.1	0.24	1.7	0.64
Q30	*7*	9.7	0.17	1.7	0.54
Q60	*6*	9.1	0.20	1.8	0.60
Q120	*6*	6.6	0.31	2.0	0.80
Q240	*6*	6.1	0.36	2.2	0.90
	PIG 3				
	Gamma Fit				
Flow Rate (µl/hr)	**Number of Tests**	**Shape z**	**Scale φ**	**Mean µ**	**STD**
Q10	*9*	8.9	0.19	1.7	0.58

Q20	*8*	9.9	0.18	1.8	0.57
Q30	*5*	11	0.16	1.8	0.53
Q60	*1*	9.5	0.19	1.8	0.60
Q120	*6*	9.0	0.21	1.9	0.63
Q240	*4*	7.3	0.28	2.1	0.76
	HUMAN				
	Gamma Fit				
Flow Rate (µl/hr)	**Number of Tests**	**Shape z**	**Scale φ**	**Mean µ**	**STD**
Q20	*3*	11	0.16	1.8	0.53
Q30	*2*	9.6	0.20	1.9	0.62

From data in Table 3-2, the axis ratio (semi-major over semi-minor axis) tends to increase as the flow rate increases. This could support evidence that the aggregate ellipsoid becomes more elongated as the flow rate increases, either by increasing its semi-major axis or decreasing it semi-minor axis. Values of the highest recorded mean axis ratio for Pig 1, Pig 2, Pig 3, and the human specimens were 2.2, 2.2, 2.1, and 1.9 respectively. Each specimen had the highest recorded axis ratio at the highest tested flow rate. As clearly illustrated in Figure 3-4. The STD of the raw data tends to increase as the flow rate increases with the highest rates of STD at the highest tested flow rate for each specimen. The Gamma fitted data shows a decrease in the shape parameter and an increase in the scale parameter as the flow rate increases. This is the opposite of what was observed with the normalized mean size of the semi-minor axis. This means the axis ratio becomes more variable at higher flow rates with a larger spread. The shape parameter ranged from 11 to 6.1 while the scale parameter ranged from 0.36 to 0.15, both are clearly shown in Figure 3-5.

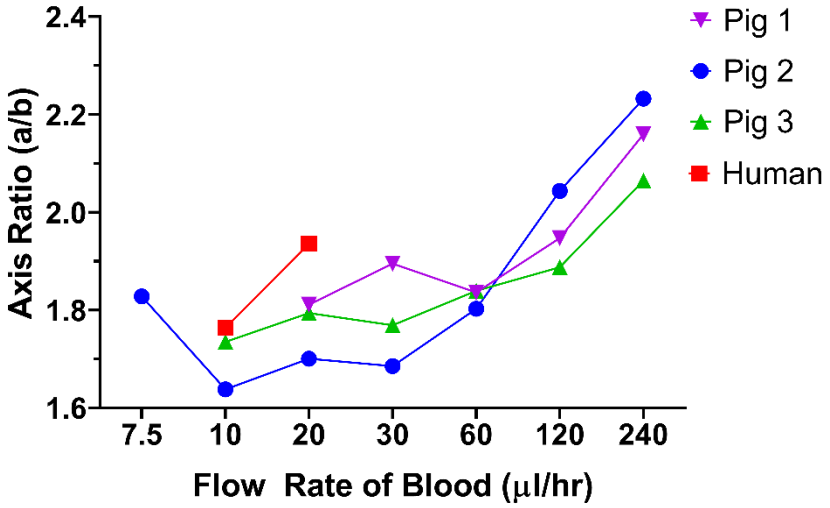

Figure 3-4: *The mean axis ratio of the ellipsoid aggregate (a/b) from the fitted Gamma pdf displayed at varying flow rates for all four specimens in the Mehri et al. experiments.*

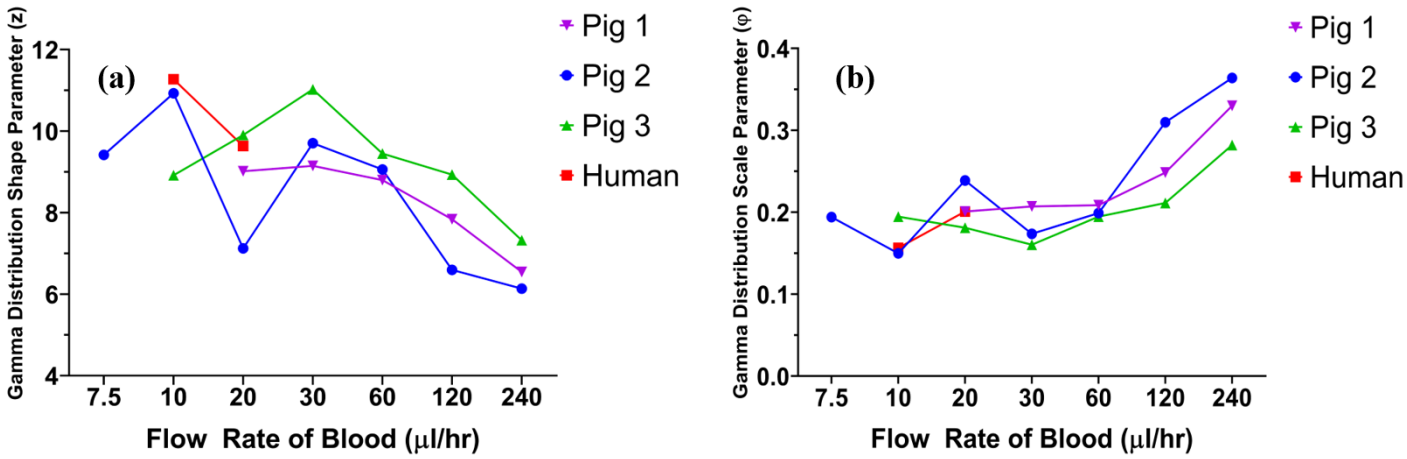

Figure 3-5: *Shape and Scale parameter of the axis ratio; (a) z of the fitted Gamma pdf of the axis ratio displayed as a function of flow rate used by Mehri et al. for all four specimens. (b) φ of the fitted Gamma pdf of the axis ratio displayed as a function of flow rate used by Mehri et al. for all four specimens.*

Table 3-3 summarizes the average aggregate orientation from each flow rate tested for each specimen.

Table 3-3: *Fitted quantitative results from each orientation angle histogram from all blood samples in Mehri et al. experiments.*

	PIG 1			
	Gaussian Fit			
Flow Rate (µl/hr)	**Number of Tests**	**Mean**	**STD**	**Variance**
Q20	*3*	-2.1	81	6568
Q30	*3*	-3.9	75	5606

Q60	*3*	-4.5	70	4869
Q120	*5*	-2.7	68	4619
Q240	*6*	-0.91	66	4376
	PIG 2			
	Gaussian Fit			
Flow Rate (µl/hr)	**Number of Tests**	**Mean**	**STD**	**Variance**
Q7.5	*3*	-1.5	83	6919
Q10	*6*	0.91	74	5450
Q20	*7*	1.2	73	5296
Q30	*7*	3.0	76	5810
Q60	*6*	3.0	74	5452
Q120	*6*	2.4	61	3717
Q240	*6*	1.5	57	3287
	PIG 3			
	Gaussian Fit			
Flow Rate (µl/hr)	**Number of Tests**	**Mean**	**STD**	**Variance**
Q10	*9*	-0.91	74	5404
Q20	*8*	-1.1	77	5920
Q30	*5*	-2.7	79	6183
Q60	*1*	-2.7	71	5023
Q120	*6*	-3.0	68	4674
Q240	*4*	-3.6	62	3894
	HUMAN			
	Gaussian Fit			
Flow Rate (µl/hr)	**Number of Tests**	**Mean**	**STD**	**Variance**
Q20	*3*	-0.30	75	5686
Q30	*2*	0.91	76	5771

Looking at the data in Table 3-3, the mean orientation angle stays rather constant, at or around 0°. The STD in the raw data decreases as the flow rate increases, thus implying that more aggregates tend to align themselves with the flow at faster flow rates. The high STD values found suggest a wide spread to the distribution. The STD still decrease as flow rate increases with the lowest STD found at the highest flow rates. This again suggests that more aggregates tend to align themselves with the flow at higher flow rates. Figure 3-6 shows the change of the mean orientation angle at each tested flow rate for each specimen.

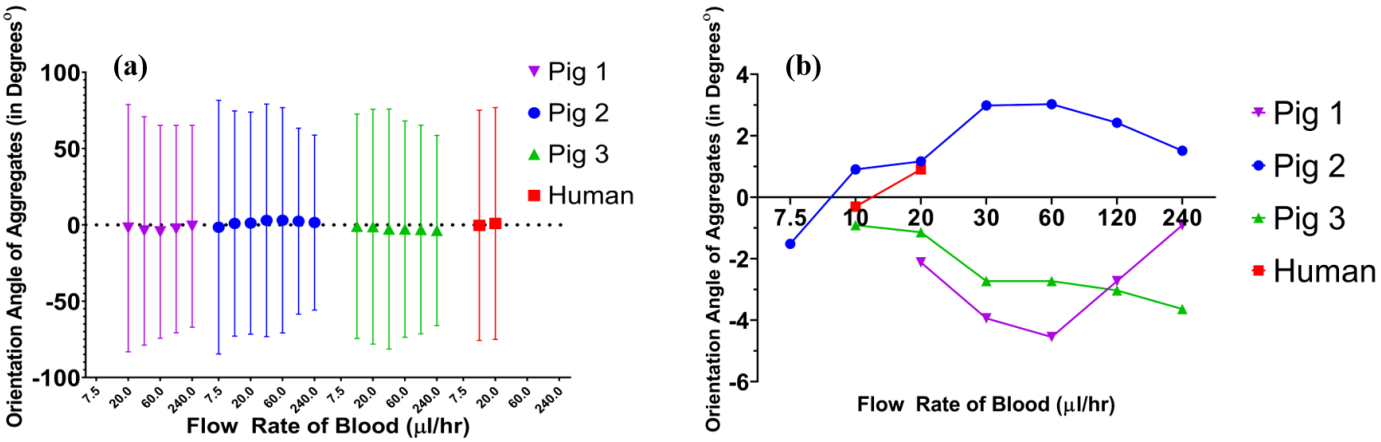

Figure 3-6: *Orientation angle of aggregates from Mehri et al. experiments at each analyzed flow rate, including all specimens; (a) and (b) depict the mean θ but (a) separates each specimen and displays the STD.*

The complete set of analyzed data was then used in testing the EMTLMA model by Franceschini et al. Figure 3-7 depicts a portion of data from the porcine experiments at flow rates 10µl/hr, 20µl/hr, and 30µl/hr with shear rates of 3 s^{-1}, 6 s^{-1}, and 11 s^{-1} respectively [8], [9].

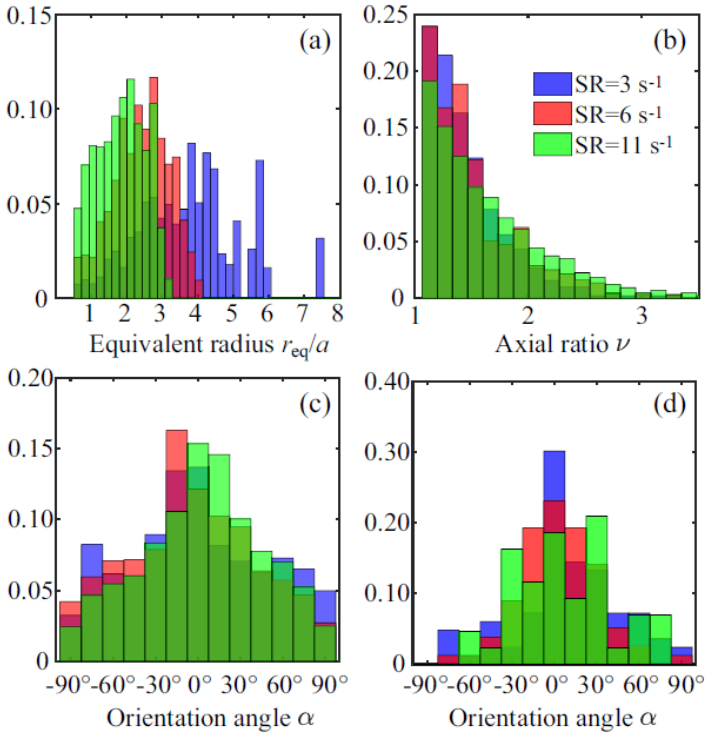

Figure 3-7: *Histograms of the aggregate volume distribution p(req)(4/3)πr3 (panel a), of the axial ratio distribution (panel b) and of the orientation distribution (panel c) for the blood sample with hematocrit φ=10%. (d) Histograms of the orientation distribution p(α) considering only the large aggregates req/a > 2.25 with ν >1.7. These histograms were acquired from Chinchilla et al. from LMA.*

Mehri et al. showed that each flow rate in its microfluidic co-flow corresponded to a specific shear rate. It was found that 10µl/hr for the shearing fluid corresponded to a constant shear rate of 3 s^{-1}, while flow rates 20µl/hr, 30µl/hr, and 60µl/hr corresponded to constant shear rates of 6 s^{-1}, 11 s^{-1}, 22 s^{-1} respectively. The data presented in Figure 3-7 is set to be published in the Journal of the Acoustical Society of America by Chinchilla et al. from work done at the LMA. Part of the aim of the research at LMA is to propose an anisotropic formulation of the EMTLMA and compare theoretical isotropic and anisotropic backscatter coefficient (BSC) calculations to 3D computer simulated ultrasonic backscattering. The computer simulations are modelled using the Gamma distributions of aggregate size from the optical image segmentation of RBC aggregates presented in this thesis.

3.2 Microfluidic Device Compliant Characterization

Each of the 8 PDMS and NOA63 microfluidic devices underwent 3 trials at each flow rate. The results from example PDMS trials are presented in Figure 3-8**.**

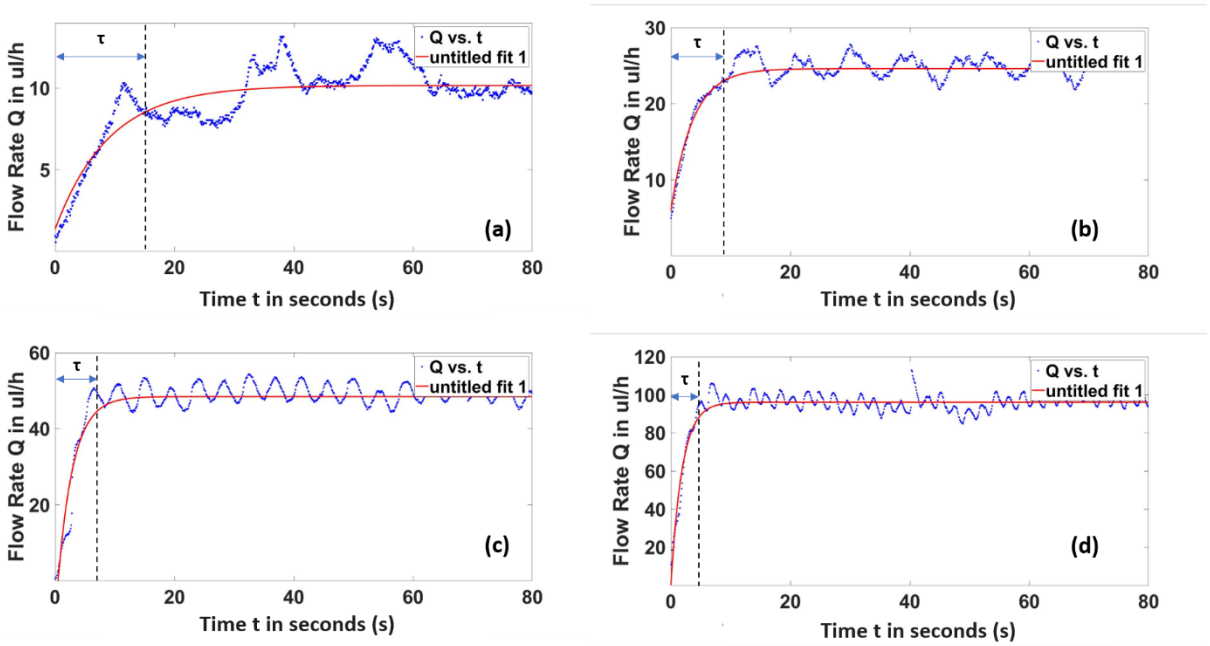

Figure 3-8: *PDMS flow rate versus time graphs. a), b), c), and d) are examples of a PDMS microfluidic device sample at each flow rate of 10µl/h, 25µl/h, 50µl/h, and 100µl/h respectively. Each device has a significant initial rise from zero to the plateau value (Q_{out}) over the time interval τ measured from the Fluigen Flow Meter (S).*

Figure 3-9 represents examples from the NOA device trials.

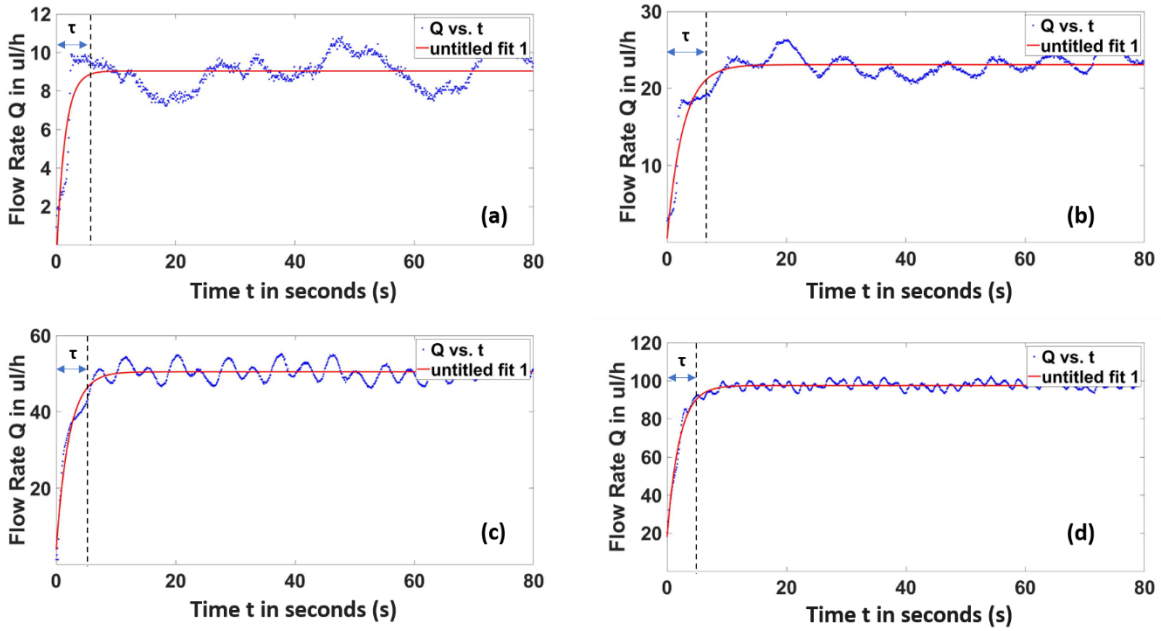

Figure 3-9: NOA63 flow rate versus time graphs. a), b), c), and d) are examples of a NOA63 microfluidic device sample at each flow rate of 10µl/h, 25µl/h, 50µl/h, and 100µl/h respectively. Each device has a significant initial rise from zero to the plateau value (Q_{out}) over the time interval τ measured from the Fluigent Flow Meter (S).

All of the PDMS and NOA63 trials characteristic times were averaged and compared in Figure 3-10. The data was considered a normal distribution, due to the nature of the data which describes a physical property of a material [130].

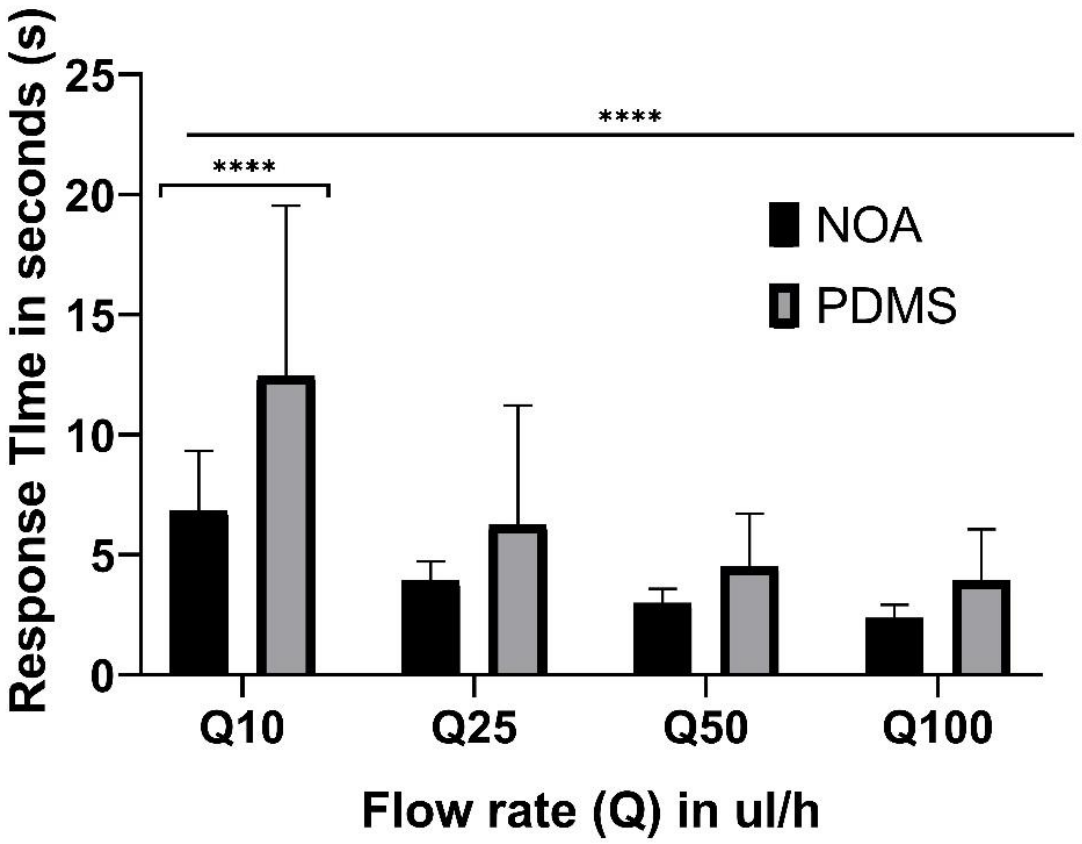

Figure 3-10: Comparison of average characteristic times τ for NOA and PDMS devices at four different flow rates (Q10, Q25, Q50, Q100 in µl/h).

As shown in Figure 3-10, there was a clear difference between the characteristic time of the NOA device versus the PDMS device. It was found that the PDMS devices had a characteristic time around 51% longer than that of the NOA device. Looking at the characteristic time differences, at each of the four flow rates, there was a statistical difference between all flow rates presented in Figure 3-10. The 10µl/hr (Q10) flow rate had a statistical difference between both the NOA and the PDMS trials. Furthermore, Q10 suggested a difference in the average characteristic time of around 58%. The PDMS characteristic time was much higher than that of the NOA device at 12.5 seconds and 6.8 seconds, respectively, at Q10. This trend was consistent at all other flow rates suggesting that the NOA device had a lower average characteristic time. The results presented in Figure 3-10 suggest a decay of characteristic time, as the flow rates increases. This suggests a plateau exists at a higher flow rate, of approximately 3.9 seconds for the PDMS device and 2.4 seconds for the NOA device.

Statistically, the results infer that the NOA devices were more consistent in performance with standard deviations of ±2.5µl/hr, ±0.8µl/hr, ±0.6µl/hr, and ±0.6µl/hr for flow rates of Q10 to Q100, respectively. Alternatively, the PDMS devices demonstrated more inconsistency, showing standard deviations of ±7.1µl/hr, ±5.0µl/hr, ±2.2µl/hr, and ±2.1µl/hr for flow rates of Q10 to Q100, respectively. The characteristic time of varying geometries of microfluidic devices are displayed in Figure 3-11. Each geometry is based off a characteristic length a. The four geometries include a square (a x a), a rectangle (2a x a), a longer rectangle (5a x a), and a circle (radius of a).

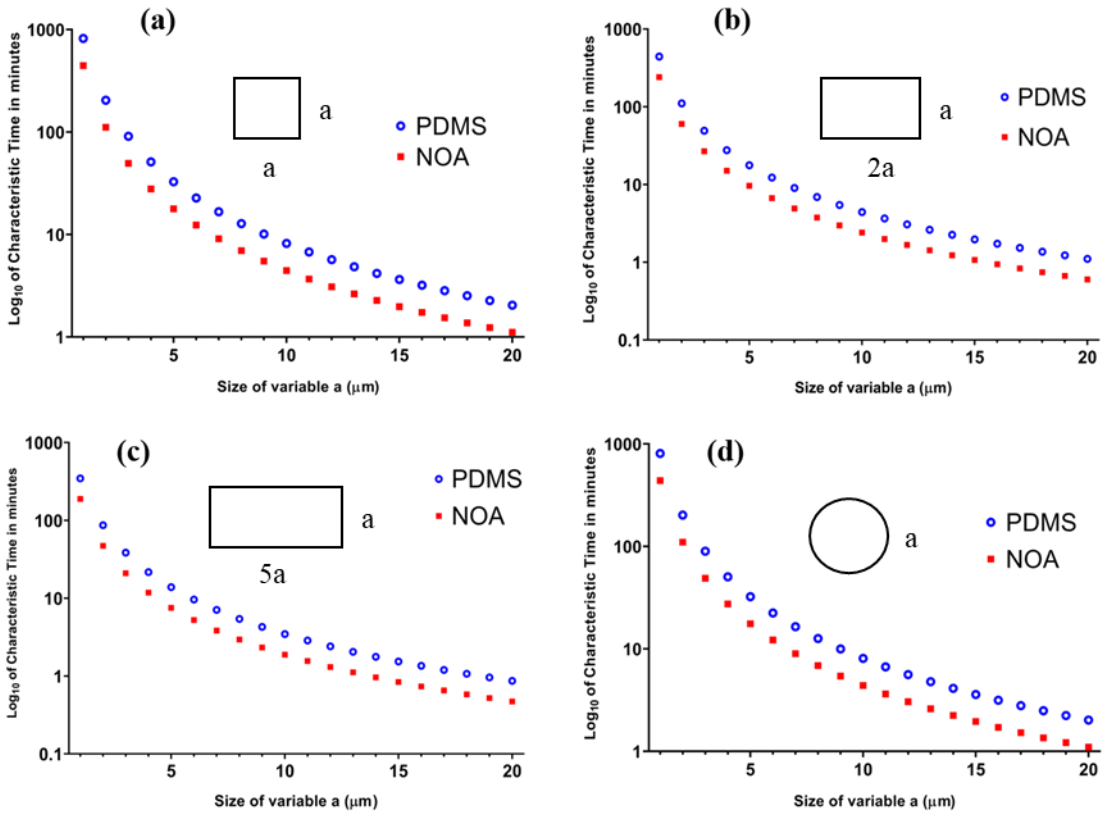

Figure 3-11: *theoretical characteristic times (displayed using a logarithmic scale) of four different microfluidic device cross-sectional areas, all based off a geometric variable of "a" which determines height, width and radii of the cross-sectional area. The four geometries include (a) square (a x a), (b) rectangle (2a x a), (c) rectangle (5a x a), and (d) circle (radius of a). The characteristic time is plotted versus the size of the variable a in µm. Both NOA (red square) and PDMS (blue circle) characteristic times are shown for each geometry.*

In each simulation the NOA device had characteristic times around half of PDMS. At a characteristic length *a* equal to 1µm for example, the difference in characteristic time between PDMS and NOA device was 6.2hr, 3.4hr, 2.6hr, and 6.1hr for square, rectangle (2a x a), rectangle (5a x a), and circle respectively. At a

common microfluidic device cross-sectional area of 5µm x 5µm the characteristic time is approximately 15min shorter for the NOA chip.

3.3 Flow properties and Calibration of Microfluidic Device

The calibration of the microfluidic device shear rate was done by analyzing the velocity profile of all the flow rates of each sample solution. An example of all ten velocity profiles obtained is given in Figure **3-12**: these are of the Dextran 70 sample solution with a concentration of 2.5g/100ml at all 10 blood flow rates.

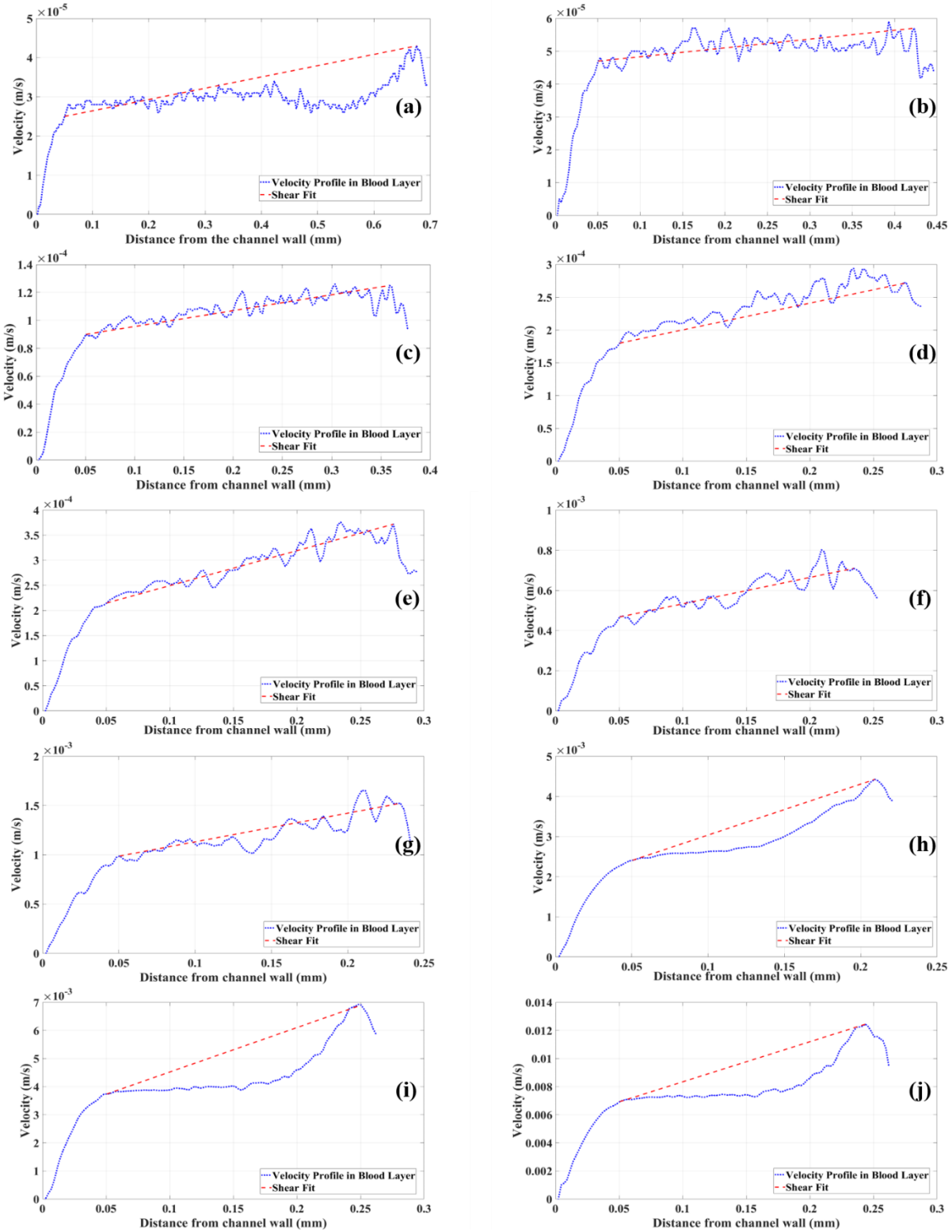

Figure 3-12: *Velocity profiles from the μPIV trials of Dextran 70 (2.5g/100ml) at each flow rate: (a) 25μl/hr:1μl/h, (b) 50 μl/hr:2 μl/hr, (c) 100 μl/hr:4 μl/hr, (d) 200 μl/hr:8 μl/hr, (e) 250 μl/hr:10 μl/hr, (f) 500 μl/hr:20 μl/hr, (g) 1000:40, (h) 2000 μl/hr:80 μl/hr, (i) 4000 μl/hr:160 μl/hr, and (j) 7500:300.*

From the velocity profiles an estimate shear rate can be obtained in the blood layer at each flow factor (section 2.3.5). In order to design the future experiments invoving the ultrasound sensor, the shear rate calibration curves of the device are presented for the differents blood conditions. Figure 3-13 depicts the relation beteewen the flow factor in the blood layer when RBC are suspended in PBS, and shear rates.

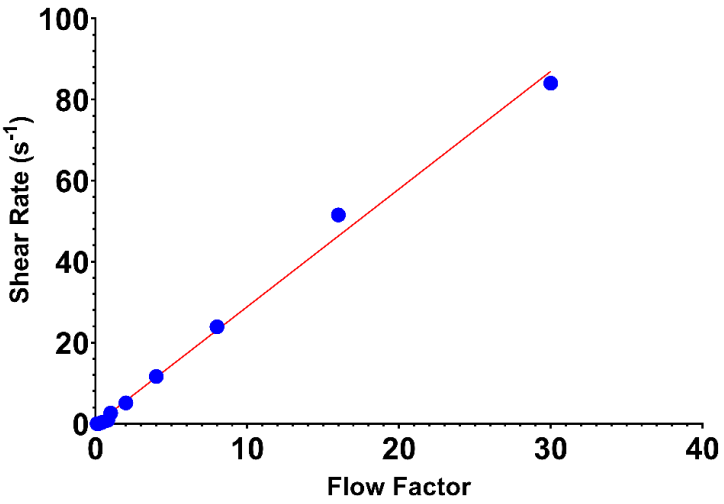

Figure 3-13: *RBC suspension in PBS: estimated shear rate in s^{-1} against the flow factor values (defined in table 2-5) of each trial*

Shear rates are presented in Figure 3-14 for each sample solution of Dextran 70 and PBS for comparison. Figure 3-14 presents the shear rate at all flow factors.

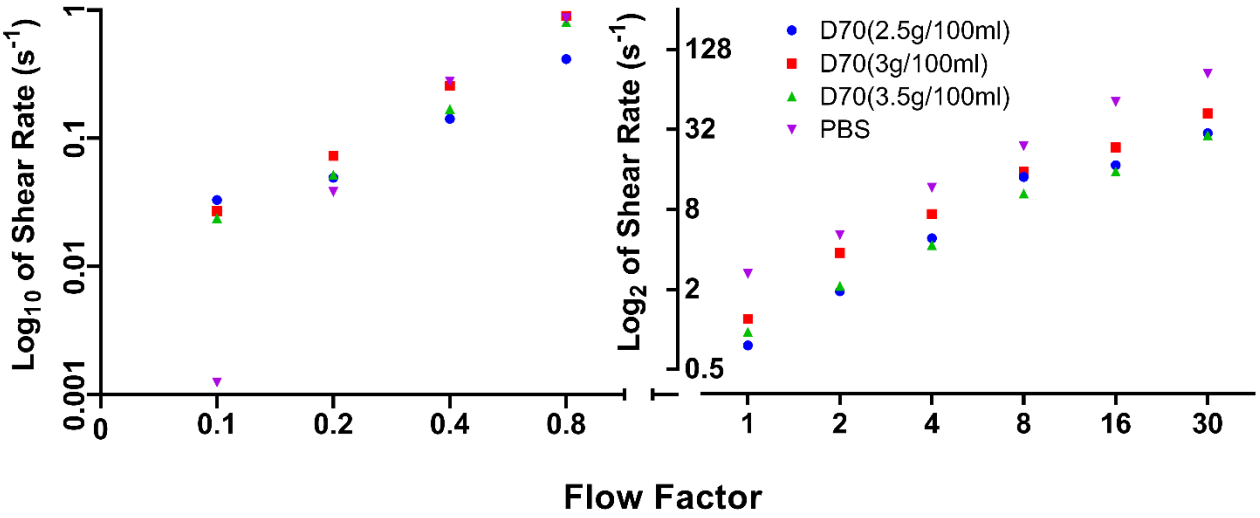

Figure 3-14: *Estimated shear rates of suspension in PBS and in each Dextran 70 solution at each flow factor (defined in table 2-5), low flow factors (<1) displayed on a log_{10} scale with high flow factors (>1) displayed on a log_2 scale.*

The maximum shear rate of each Dextran 70 concentration including PBS was $30s^{-1}$, $42s^{-1}$, $29s^{-1}$, and $84s^{-1}$ for concentrations of 2.5g/100ml, 3g/100ml, 3.5g/100ml, and 0 g/100ml (suspenssion in PBS) respectivley. For Dextran 70 and PBS at concentrations of 2.5g/100ml, 3g/100ml, 3.5g/100ml, and 0 g/100ml, the shear rates ranged as low as $0.033s^{-1}$, $0.027s^{-1}$, $0.024s^{-1}$, and $0.0012s^{-1}$ respectivley.

Shear rates are presented in Figure 3-15 for each sample solution of Dextran 500 and PBS. Figure 3-15 presents the shear rate at all flow factors.

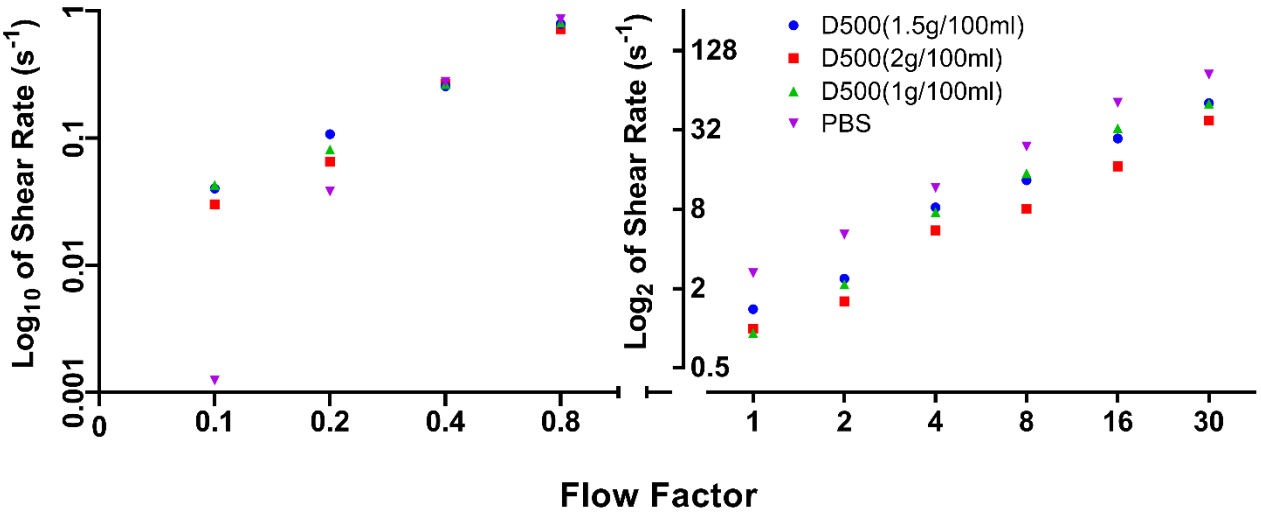

Figure 3-15: *Estimated shear rates of RBC is suspention in PBS and in each Dextran 500 solution at each flow factor* (defined in table 2-5), *low flow factors (<1) displayed on a log_{10} scale with high flow factors (>1) displayed on a log_2 scale.*

The maximum shear rate of each Dextran 500 concentration with RBC suspension in PBS was $51s^{-1}$, $51s^{-1}$, $38s^{-1}$ and $84s^{-1}$ for concentrations of 1g/100ml, 1.5g/100ml, 2g/100ml, and 0g/ml (suspension in PBS) respectivley. For Dextran 500 conecentration of 1g/100ml, 1.5g/100ml, and 2g/100ml the shear rates ranged as low as $0.043s^{-1}$, $0.04s^{-1}$, $0.031s^{-1}$ respectivley.

Also assisting the future expereriments involving the ultrasound, the blood layer tickness calibration curves of the device are presented for the differents blood conditions. The size of the blood layer varied as the flow rate increased. For the Dextran 70 trials Figure 3-16 displays the blood layer size at each flow rate factor in µm including the RBC dilution in PBS for comparison.

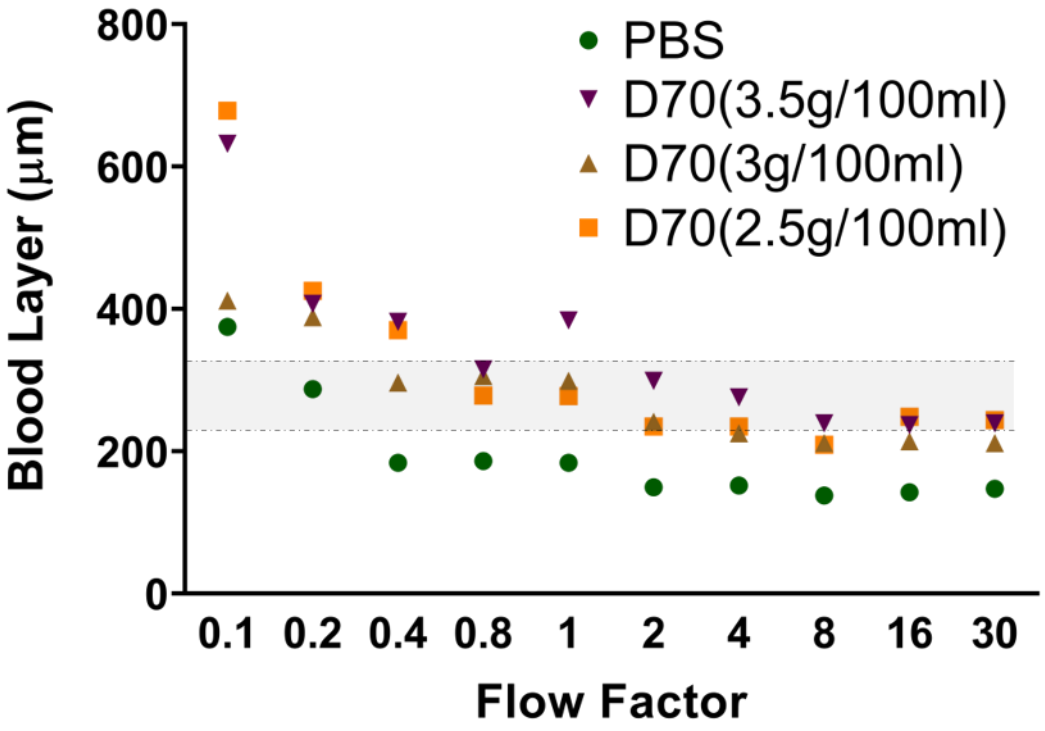

Figure 3-16: *Size of blood layer (µm) at each flow factor (defined in table 2-5) during each trial for Dextran 70 (at concentrations of 2.5g/100ml, 3g/100ml, and 3.5g/100ml) and PBS; theoretical blood layer for µ values 1-3 cP, is highlighted in faded grey (between 0.24um and 0.34um).*

The greyed area of Figure 3-16 represents the theoretical blood layer tickness for viscosity values within 1-3 cP (10% hematocrit) using the sheared flow in a Parallel Plate Model. The range (240µm and 340µm) is within the same range as the experimental data. The PBS sample had the most consistent and smallest blood layer values with a mean and STD of 0.19mm ± 0.077mm. The mean blood layer of all D70 samples with STD are 0.32mm ±0.14mm, 0.28mm ±0.073mm, and 0.34mm ±0.12mm for concentrations of 2.5g/100ml, 3g/100ml, 3.5g/100ml, respectivley.

For the Dextran 500 trials the blood layer size at each flow rate in µm is given in Figure 3-17.

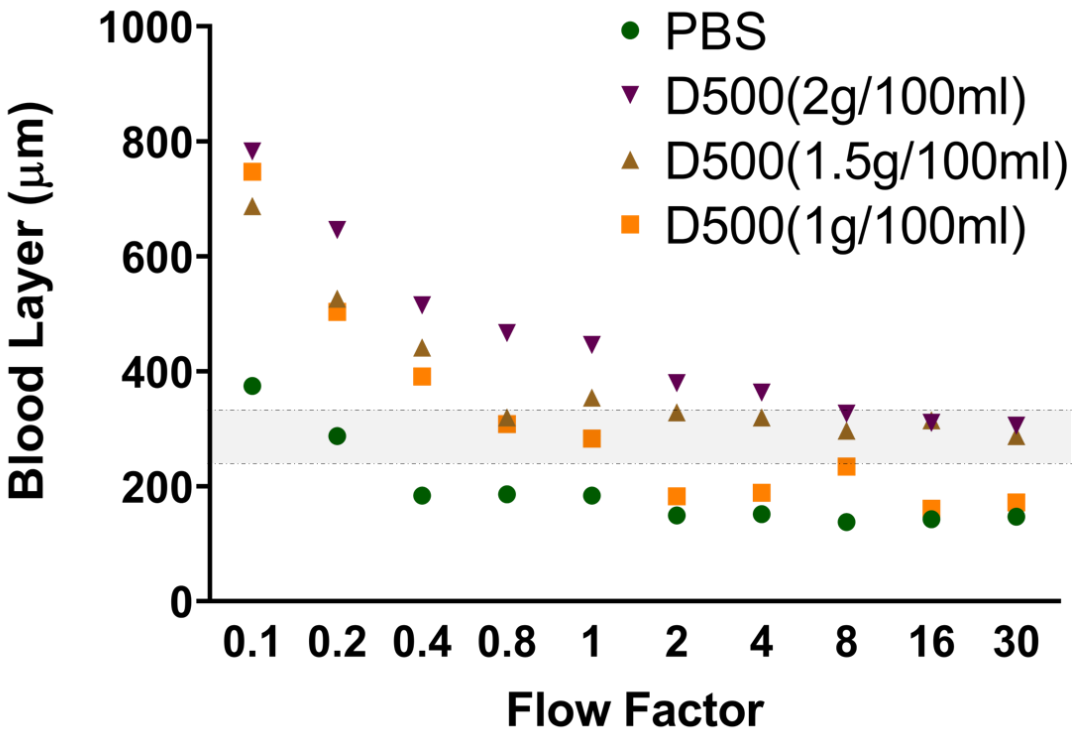

Figure 3-17: *Size of blood layer (µm) at each flow factor (defined in table 2-5) during each trial for Dextran 500 (at concentrations of 1g/100ml, 1.5g/100ml, and 2g/100ml) and PBS; theoretical blood layer for µ values 1-3 cP is highlighted in faded grey (between 0.24µm and 0.34µm).*

The greyed area of Figure 3-17 represents the theoretical blood layer in a Parallel Plate model for viscosity beteewen 1-3 cP. The PBS sample had the most consistent and smallest blood layer values with a mean and STD of 0.19mm ±0.077mm. The mean blood layer of all D500 samples with STD is 0.32mm ±0.19mm, 0.39mm ±0.13mm, and 0.45mm ±0.16mm for concentrations of 1g/100ml, 1.5g/100ml, 2g/100ml, respectivley.

Chapter 4

4 Discussion

4.1 Aggregation Characterization

4.1.1 Limitations of Post Processing Procedures

The algorithm developed by Niazi et al. was used for analysis due to its ability to quickly and efficiently analyze aggregates in 2D images. The algorithm was validated against the current gold standard method of manual techniques for aggregation size measurement and for size distribution accuracy, published in the journal, *Institute of Physics and Engineering in Medicine* [65], [66]. The algorithm was found to have errors of 2-4% in comparison to the manual methods. These validations were completed at hematocrit values of 5%, 10%, and 15%.

When analyzing images using the automatic image analysis technique, detecting multiple objects from sequential images can cause problems. The higher the density of RBCs the more impactful this problem can be. High densities, or high hematocrits, can result in overlapping aggregates and lead to false detections. To remedy these errors, several image processing techniques have been incorporated into the algorithm. These include the multiple filters and binary operators that allow for more accurate aggregate detection [66]. Another source of error in the algorithm is its assumption of 2D flow. This is necessary due to the nature of image analysis although, in reality, RBCs travel in three dimensions across the flow. To combat this error and the possible overlap of aggregates, Mehri et al. used a microfluidic device with dimensions of 110x60μm^2. The small depth of 60μm creates a confined area that encourages less overlap since RBCs will tend to travel towards the centre of the channel due to the Saffman force [66], [132].

4.1.1.1 Two-Dimensional Processing

The 2D image analysis of the specimens is one major limitation to the procedures used to estimate the aggregate shape in three-dimensions (prolate ellipsoid) with the fitted ellipse from the optical

measurements. The extrapolation of 2D information in three-dimensions is unrealistic and results in minimum radii smaller than possible for RBC radius. This could introduce bias into the simulations. It is evident that RBCs can change orientation while flowing through the device. Figure 4-1 depicts an example of an aggregate rotating, changing its 2D shape.

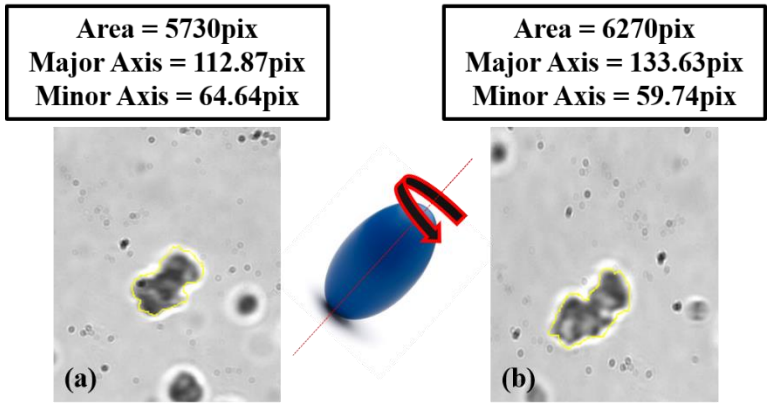

Figure 4-1: *Depiction of an aggregate rotating without changing the orientation angle, (a) before rotation with area of 5730pix; (b) aggregate after rotation with area 6270pix.*

The aggregate highlighted in Figure 4-1 has a semi-minor axis size of 64.64pix in (a), and 59.74pix in (b). The difference in aggregate size based on the semi-minor axis is around 7%. Since an aggregate rouleaux consists of RBCs stacked on top of each other, the small discrepancy in size is to be expected. However more complex aggregate shapes can form and further analysis of the effects of aggregate rotation should be conducted.

4.1.2 Aggregate Alignment and Size in Relation to Flow Rate

The aggregate 2D segmentation yielded results similar to that of the researchers at LMA. A decrease in size at higher flow rates was found as depicted in Figure 3-2. The Gamma fit does indicate that the normalized mean size of the semi-minor axis tends to decrease as the flow rate increases. This is evident in Figure 3-3 which shows the decrease in the scale parameter as the flow rate increases. The shape parameter of the Gamma pdf increases as the flow rate increases, suggesting a change in shape of the distribution. The size of the normalized semi-minor axis, therefore, does seem to decrease as the flow rate increases. Since the mean axis ratio shown in Figure 3-4 increases at higher flow rate, an increase in the semi-minor axis of

the aggregate ellipsoid is suggested. However, the aggregates become disaggregated as the shear rate increases, therefore the small decrease in the normalized semi minor axis suggests most aggregates take the shape of rouleaux. This is consistent with the findings of LMA and advocates that aggregate size decreases when the shear rate increases. The elongated aggregates found in this study are also supporting evidence of the anisotropic nature of RBC aggregates as predicted by the EMTLMA model by Franceschini et al.

The orientation of the aggregates as depicted in Figure 3-1 (d) suggests that the aggregates tend to align themselves to the flow. The number of aggregates aligned to the flow increases as the shear rate increases (flow rate is increased). Figure 3-7 (histogram (d)) from Chinchilla et al. shows the distribution of aggregates with axis ratios greater than 1.7 and b/a_c greater than 2.25. This histogram suggests that larger aggregates tend to align themselves to the flow. The orientation of the aggregates in Figure 3-6 suggests that the alignment of large aggregates to 0 degrees increases as the shear rate increases. It is important to note the large STD of the data in Figure 3-6. When looking at RBC and RBC aggregates in flow, it is important to consider studies done about the orbital pattern of RBCs [133]–[135]. In particular the studies done by Harry L. Goldsmith [133]. He was able to detail the orientation of a 15 RBC rouleau over time. From his studies he was also able to show that aggregates spent most of their time aligned to the flow as their velocity of rotation tended to be much higher when perpendicular to the flow [133], [134]. As illustrated here in Figure 4-2.

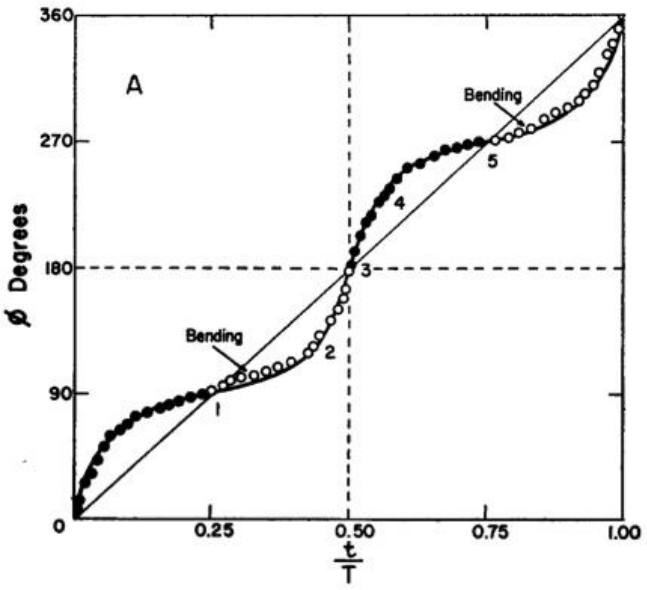

Figure 4-2: *Variation in orientation (φ) of 15 cell rouleau in Poiseuille flow. The dots represent experimental results, while the line represents simulated results. This graph was obtained from Harry L. Goldsmith's paper* The Microrheology of Red Blood Cell Suspensions *in the Journal of General Physiology [133].*

From Figure 4-2, it is possible to deduce the velocity of rotation of the aggregate, and thus acquire the PDF of the angle based on the velocity of rotation. This PDF describes the probability of the aggregates position. Figure 4-3 shows the histogram of the angle of orientation from Figure 3-1 (d), with the PDF acquired from Goldsmith's data based on velocity of rotation.

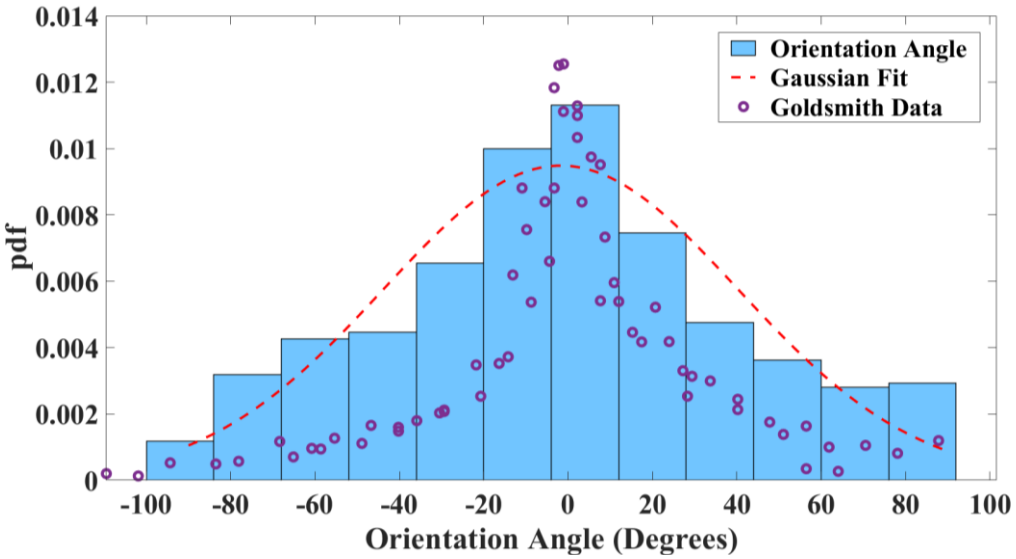

Figure 4-3: *Orientation angle distribution as seen in Figure 3-1 (c); red line is the fitted Gaussian distribution, purple 'o' represents the PDF found from Goldsmith data in Figure 4-2 [133].*

The distributions in Figure 4-3 are similar, implying that aggregates spend more time aligned to the flow than perpendicular too it. For that reason, when pictures were acquired, more aggregates were aligned with the flow. It is important to note that the superimposed data from Goldsmith in Figure 4-3 was acquired from one individual aggregate, whereas the histogram was generated from tens of thousands of aggregates. It appears from the segmentation results that the aggregates align themselves parallel with the flow, although evidence suggests the aggregates constantly rotate spending a majority of time aligned with the flow.

Overall, the segmentation data matches the findings of research done at LMA. It furthers the understanding of aggregate flow properties allowing for new models of quantitative ultrasound backscattering techniques to be developed. The data will be used to assist in the development of ultrasound backscattering techniques used for aggregation characterization. The overall effect of the 2D interpretation of aggregate size and orientation, extrapolated into three dimensional simulations, is yet to be discovered. Future studies using confocal microscopic techniques and the same methodology performed by Mehri et al. could help in determining a more accurate 3D aggregate structure.

4.2 NOA Microfluidic Device

4.2.1 Flow Rate Measurement Uncertainty

The Small Fluigent flow meter, with a range of ±420 µl/hr, was used to accommodate the low flow rates used in the protocol. The accuracy of the device was ±5% of the measured value for all flow rates of 25µl/hr and higher, and ±1.26µl/hr for all measurements below 25µl/hr. Therefore, measurements taken at 10µl/hr had approximately, 90% accuracy. The repeatability of the device was within 0.5% for all measurements taken above 42µl/hr and ±0.21µl/hr below 42µl/hr. Thus, all measurements taken were repeatable within 0.5% of the measured value except those taken at Q25 and Q10, which were repeatable within 0.84% and 2.1% of the measured value, respectively.

The high standard deviations, for the PDMS and NOA devices, can be explained by the inaccuracy of the Fluigent flow meter at low flow rates (Q10). Although, the standard deviations are consistently high for the PDMS devices, the inconsistency in characteristic time, compared to NOA devices, suggests differences in the PDMS vs NOA devices. In PDMS devices, small variations in material properties can occur with changes in temperature, holding time, and altered mass ratios of pre-polymer to curing agent [126], [136]. Furthermore, PDMS thickness can affect flow conditions and can display significant bulging or deformation during use [95], [137], [138]. Slight altercations to the PDMS mechanical properties, through uncontrolled parameters, coupled with deformation may also contribute to the large standard deviations with PDMS devices. Consistency with the NOA results, suggests a more repeatable system than PDMS equivalents. The only flow rate over ±1µl/hr with NOA devices was that of the Q10 flow rate and it was the highest standard deviation measured for NOA devices. This increase is expected due to the 2% disparity in the Fluigent flow meter at the aforementioned flow rate.

4.2.2 Dependency of Characteristic time on Flow Rate

The rate of storage for the system, Q_c, is described by Equation *(2.4)* as the compliance (C) multiplied by the change of pressure over time $\left(\frac{dP}{dt}\right)$. As the flow rate increases, the system pressure increases as well, which ultimately increases the volume of the rate of storage of the system. This is only achieved by changing the diameter of the system, which consequently decreases the resistance. This decrease in characteristic time can be further explained using the modeling equations derived from the Windkessel model. In Equation *(2.9)*, characteristic time is represented proportionally to the compliance and the resistance of the system. This could suggest the decrease is due to the pressure increase at higher flow rates, thus causing larger cross-sectional area leading to a decrease in system resistance. The result is a decreased characteristic time, as evident in Figure 3-10.

4.2.3 Characteristic Time Dependency on Geometry

The untraditionally large microfluidic device used for these trials consisted of a channel width of 2mm by 60µm. More traditionally sized microfluidic channels, for example 100µm by 50µm, would

correspondingly increase the resistance produced by the microfluidic device. The theoretical resistance can be calculated using the hydrodynamic resistance equation for a rectangular or circular cross section, as seen in section 2.2.3 of this thesis. The resistance of the current microfluidic device and more traditional devices is around $5.15x10^5$ MPa*s/m^3 and $1.10x10^8$ MPa*s/m^3, respectively. The more traditional microfluidic dimensions increase the resistance by a magnitude of 10^3. Since resistance is directly linked to the characteristic time of the system, these results suggest a more exaggerated difference in characteristic times between PDMS and NOA for smaller channel cross-sectional areas. Further study of this difference is shown in Figure 3-11. Theoretical characteristic times were simulated based on the geometrical size and shape of more traditional microfluidic devices. The difference of characteristic time at smaller geometries can be as high as approximately 6hrs.

4.2.4 Compliance

Since the flow is modelled using Equation *(2.6*), the characteristic time is calculated as system resistance (R_s) multiplied by the compliance (C). The system setup used was consistent throughout all trials. Therefore, the same rigid tubing and glass syringes were used throughout the entire experimental process. Thus, the only change to the resistance and compliance of the system can be directly associated with the change in the microfluidic device being tested. Due to the low compliance of the materials, the system outside of the microfluidic device was assumed to be negligible when comparing characteristic time values. It's also important to note, that the resistance of the system outside of the microfluidic device (syringes and tubing, etc.) is constant. The estimated value is calculated to be $3.37x10^{-5}$ MPa*s/m^3 compared to the resistance of the chip estimated to be $5.15x10^5$ MPa*s/m^3. Thus, the characteristic times seen in Figure 3-10, are directly related to the compliance of each microfluidic device, therefore suggesting that the PDMS devices have on average, a higher compliance than that of the NOA devices.

4.2.5 Anticipated Periodic Instability of the Output Flow

The results presented in Figure 3-8 and Figure 3-9, show the flow rate change over time of PDMS and NOA, respectively. The data demonstrate a clear rise and plateau, following the derived model presented.

For both NOA and PDMS devices, the raw data plateaued with a sinusoidal behaviour. This behaviour was analyzed and found to be, as anticipated, from the syringe pump's (Chemyx Nexus 3000) stepper motor [139], [140]. It was verified that the frequency was given by the product of the velocity of the syringe pump and the step resolution (0.012μm/step for our pump). The velocity of the pump can be easily obtained dividing the flow rate by the syringes cross-sectional area.

4.3 NOA Microfluidic Device Shear Rate Calibration

4.3.1 Velocity Profile Measurement Accuracy

Sources of error can arise from the acquisition of the velocity profile and measurement of the shear rate. Theses include uncertainties in DOC, Brownian motion, camera calibration and timing, variation in hematocrit, boundary layer, and the cell free layer (CFL).

4.3.1.1 Depth of Correlation

The DOC is affected by the number of particles present in the field of view. Since the effect of RBCs on the DOC is difficult to estimate the best methods for dealing with errors in DOC were utilized. Proper post processing techniques shown to minimize the effect of RBCs on the DOC were utilized [116]. These methods are outlined in section 2.3.3. Therefore, the effects of DOC were neglected.

4.3.1.2 Brownian Motion

Brownian motion plays a vital role in μPIV systems. To counteract the effects of Brownian motion the 100 frames acquired are averaged which greatly reduces the effect of the random motion of particles.

4.3.1.3 Timing and Camera Calibration

The dt (timing interval) used was determined by the automated dt calibration system built into the DaVis software. This allowed for more accurate dt settings leading to more precise measurements of velocity. In the DaVis manual the uncertainty of the timing unit however is 5 ns. This means that for two

pulses the uncertainty of the timing is 10ns. The smallest dt value used was 203 us which leads to an uncertainty of around 0.0025%. Therefore, the dt uncertainty can be neglected.

Camera calibration was performed as described in section 2.3.3. Using a 10x lens magnification the scale was determined as 0.57μm/pixel. This scale was used consistently throughout all experiments.

4.3.1.4 Hematocrit Variation

Hematocrit was measured before adding the packed RBC to each sample. When measured the volume of packed RBC added to each sample was adjusted based on the measured hematocrit ensuring hematocrit values as close to 10% as possible. However, the hematocrit flowing through the field of view cannot be precisely controlled. Sedimentation could occur in the syringes or the tubing before reaching the microfluidic device. The addition of OptiPrep to the samples does help to prevent sedimentation but is not absolute. Tubing connections were kept as short as possible to help prevent sedimentation. Finally, the NOA microfluidic device used in these experiments consists of pillars in the entrances to the main channel as seen in Figure 2-8. These pillars create high shear rates and cause disaggregation of RBCs heading into the channel preventing clogs. However, it is possible for RBCs to become stuck within the lattice of the pillars which could affect the hematocrit in the channel. Extensive measures were taken between trials to clean the device and check for obstructions throughout the experiment.

4.3.1.5 Cell Free Layer

The CFL also effects the measured velocity profile. Gliah et al. have shown that CFL thickness changes with smaller flow rates [141]. Since the lower flow factors utilize low flow rates, the effects of CFL are evident in the lower flow factors. The multifactorial mechanism of the CFL formation is still under investigation by the hemodynamic community, but research has shown that increased aggregation may lead to an increased CFL [141], [142]. With a pronounced CFL, the change of the concentration of RBC close to the wall will change the fluid properties locally. The viscosity would be then lower than in the bulk flow (lubrification). A change of velocity profile was actually seen on the profile as shown Figure 3-12. To

account for that, a 0.05mm segment close to the wall of the microchannel was neglected from the shear measurements. This value was decided due to the shape of the velocity profile. Removing an area close to the wall of the channel also helps to prevent μPIV errors due to the correlation window, directly against the wall [9].

4.3.1.6 Two-Dimensional Estimation

The velocity profiles obtained in the experimental results were two dimensional. Therefore, great care was taken to ensuring that the focus plan was in the centre of the channel (~30μm in depth). This ensured that the velocity profile obtained was of the flows mid-plane and resulted in the fastest flow velocity within the channel. To ensure that the focal plan is in the mid-plan, pre-measurements were done and process iteratively until the max velocity was found.

4.3.2 Blood Layer Variation

If we assume the 10% RBC dilute in PBS as Newtonian fluid (no aggregation), a constant blood layer size was expected since the flow ratio of shearing flow to sheared flow was constant at 25:1. However in Figure 3-16 and Figure 3-17 it is clear that the blood layer changes at lower flow factors for all samples including the PBS. For the Dextran 70 and Dextran 500 samples, the expansive blood layer at lower flow ratio factors makes sense. The lower flow factors induce aggregation, which alters the viscosity [9], [143]. With changes to viscosity and viscous forces throughout the flow, this can account for the change in blood layer. However, the PBS sample is lacking the addition of any amount of polymer to induce aggregation and is thus presumed to be disaggregated at all flow factors. Figure 3-16 shows the estimated PBS blood layer based on the viscosity of PBS and blood at 10% hematocrit. The blood layer found experimentally is a good order of magnitude to the theoretical model. The model is based on a 2D parallel plate using Newtonian fluid and therefore, does not consider all aspects of the flow properties present and is used as an estimation. Since the blood layer is determined by the fluorescent particles as stated in section 2.3.5, the small expansion of the blood layer at flow factors of 0.1 and 0.2 could be explained by the diffusion of fluorescent particles; at low flow rates the amount of time the fluorescent particles are exposed in the flow

is increased at the same location in the device. This added time could result in more diffusion and thus a larger blood layer could be recorded. When the flow rates are increased, the diffusion effect would become negligible and the layer thickness would be found constant.

4.3.3 Dextran Concentrations Effect on Aggregability

The flow factors were selected based on the results of the PBS sample. The pseudo-linear shear growth of the PBS sample was to be expected. The Dextran sample concentrations were selected based on the aggregation results found in Red Blood Cell Aggregation, Baskurt et al. and displayed in Figure 1-3 of this thesis [1]. Comparing these results to the experimental results of Dextran 70 at 3g/100ml and Dextran 500 at 1.5g/100ml were hypothesized to have the highest aggregability due to increased interactional energy of RBCs [1]. Knowing that aggregation increases the viscosity of the flow, which in turn results in a low shear rate, it could be used to deduce the aggregability of the solution indirectly based on the shear rate results. Looking at the results of the Dextran 70 experiments, the Dextran 70 sample of 3g/100ml consistently displayed the highest shear value comparatively, too the Dextran 70 samples of 3.5g/100ml and 2.5g/100ml. This could be explained by a decrease in aggregability in comparison to other samples. The Dextran 70 sample at 3.5g/100ml displayed the lowest shear rates on average, therefore suggesting higher viscosity and consequently a higher aggregability rate. Comparing the three Dextran 500 samples, the sample of 2g/100ml clearly displayed the lowest shear rates suggesting the highest aggregability, while the sample of 1.5g/100ml consistently displayed the largest shear rates.

For both Dextran 70 and Dextran 500, the concentration that suggested the lower aggregability, also resulted in the largest blood layer. To confirm these results, suggesting that the highest concentration from both Dextran 70 and 500 resulted in the highest aggregability, a further study into the aggregate size at each concentration would need to be conducted. It is important to note that in all Dextran samples, aggregation was present in the low flow factors, increasing in size as the flow factors decreased. No aggregation was visually present for the PBS sample. It is also interesting to note that the aggregate shape was more rouleaux in the Dextran 70 samples, whereas in Dextran 500 it was more robust and larger.

4.3.4 Shear Rate and Velocity Profiles

The velocity profiles in Figure 3-12 have a particular “s” shape at higher flow rates. Figure 3-12 (j) shows clearly the shape. The reason for the deviation in pseudo-linearity is unclear and requires further investigation. Although, the shape of the high shear velocity profile is in line with the observed shape by Mehri et al. when velocity profiles were measured further from the inlet [9].

Chapter 5

5 Conclusion

5.1 Summary of Results

This thesis presents detailed methodologies in segmentation procedures of RBC aggregates in order to help quantify blood aggregation using ultrasound backscattering techniques. Large data sets of sheared porcine and human RBCs at 10% and 20% hematocrit were segmented using a certified algorithm by Niazi et al [66]. All data indicated a decrease in aggregate size with increased shear rates. They also indicated an anisotropic aggregate structure when analyzing the normalized semi-minor axis (b) and the axis ratio. Finally, the aggregates appeared to be aligned with the flow, as deduced when looking at the orientation angle of the aggregates. However, this STD on this measurement was high, though a majority of aggregates were aligning. It is hypothesized that the rotation of aggregates resulted in individual aggregates spending more time aligned to the flow. The results from the aggregation segmentation will be used in 3D computer simulations by LMA to examine the influence of aggregate size polydispersity and the anisotropic nature of aggregates when relating to the ultrasound backscattering. Further study was needed to compare the methodologies used in ultrasound backscattering techniques to that of microscopic imaging techniques which are considered the gold standard in aggregation characterization.

To do so a microfluidic device capable of low compliance under high pressure, with good optical clarity needed to be developed. Henceforth the NOA device presented in this thesis was created. The compliance of the NOA63 microfluidic device was compared under repeatable flow conditions to its PDMS counterpart. A unique way of manufacturing NOA63 microfluidic devices was presented and compared to the gold standard PDMS microfluidic devices, showing a more consistent response time than that of the PDMS. All 16 microfluidic devices were examined using the Fluigent Flow Systems software and a Fluigent flow meter, at flow rates of 10µl/hr, 25µl/hr, 50µl/hr, and 100µl/hr. On average the characteristic

times were found to be 51% longer for PDMS devices than NOA devices. Ultimately, the highest response times were found at the lower flow rates and the response times decreased with increasing flow rates. It is believed a change in the system resistance due to pressure is responsible for the non-consistent characteristic time. These results concur with the material properties of both NOA and PDMS, having elastic moduli of 325MPa and 2MPa, respectively. The results suggest NOA microfluidic devices could increase consistency in microfluidic research due to their significantly lower standard deviations. The presented results demonstrate that NOA microfluidic devices are less compliant than PDMS microfluidic devices. This could potentially encourage the use of NOA devices in microfluidic research and in high pressure microfluidic flow systems. These findings could be used to better understand the use of NOA as a microfluidic material, as well as its properties of compliance and corresponding benefits to microfluidic research.

The NOA microfluidic device was then calibrated using a μPIV system which also allowed us to characterize its velocity profile. Seven different blood samples of 10% hematocrit were tested at a flow ratio of 25:1, shearing flow (PBS) to sheared flow (blood at 10% hematocrit). Dextran 70 samples at 2.5g/100ml, 3g/100ml, and 3.5g/100ml concentrations were tested, as well as Dextran 500 samples at 1g/100ml, 1.5g/100ml, and 2g/100ml concentrations. The concentrations were selected based on the RBC aggregation results from Meiselman et al. [1], [54]. Each sample was tested at 10 flow factors therefore varying the shear rate. The blood layer of the velocity profile was analyzed to determine the estimated shear rate across it at each flow factor. This resulted in a graphical representation of shear rate (s^{-1}) displayed against flow rate. This calibration of shear rate versus flow rate was necessary to allow the researchers at LMA to conduct further experiments using their measurement methodology of blood aggregation using ultrasound backscattering techniques. The size of the blood layer was also characterized. It was found that the blood layer increased as the shear rate decreased correlating with an increase in aggregation.

5.2 Summary of Contributions

This research contributes to the understanding of RBC aggregates in microfluidic devices and the field of hemorheology. It also contributes to advancing the field of microfluidics with new fabrication procedures. Accomplishment highlights include:

1) Size and orientation distributions of RBC aggregates were obtained from optical experiments completed by Mehri et al. The images were analyzed using an algorithm developed by Niazi et al. The distributions of size and orientation characterisations were prepared and interpreted in order to be used in 3D computer simulations to help verify backscattering RBC aggregate detection techniques. The results of this analysis are being used by researchers at LMA and are set to be published in the Journal of the Acoustical Society of America.
2) A novel NOA microfluidic device was developed with low compliant properties. It was compared to the gold standard of PDMS and shown to have characteristic times of around 51% less. This work is set to be submitted in the Journal of Microelectronic Engineering.
3) The calibration of the shear rate in the NOA device was completed using human blood, at hematocrit levels of 10%. This work is set to be used to create a microfluidic device capable of using optical and ultrasound techniques simultaneously. This will allow further verification of the ultrasound backscattering methodology developed by Franceschini et al. at LMA

5.3 Future Work and Recommendations

Many limitations were mentioned in Chapter 4 (Discussion) of this thesis, however one that requires further investigation is the effect of using 2D aggregate detection on three dimensional simulations. As shown in section 4.1.1.1, aggregates can rotate within the flow without changing orientation angle. This then alters the aggregate size. The models used in the LMA simulations are created from the 2D interpretation. The effect of using this 2D information requires further investigation, perhaps using the same experimental methodology as Mehri et al., except incorporating a confocal microscope. This could provide

further information into the aggregate structure and possibly better aggregate detection under higher hematocrit values.

The shear rate and flow rate relationship of the NOA microfluidic device was calibrated. This device is now ready to incorporate an ultrasound transducer for further analysis. Using the same fabrication methodologies as those presented in section 2.2.1, an NOA device with the same geometry could be created incorporating a small ultrasound window as seen in Figure 5-1. This window reduces the amount of material between the ultrasonic transducer and the fluid flow. The estimated thickness of the wall within the window is 10µm, but some initial tests would need to be conducted with NOA and the ultrasound technique. This would ensure that the NOA63 material is compatible with ultrasound testing.

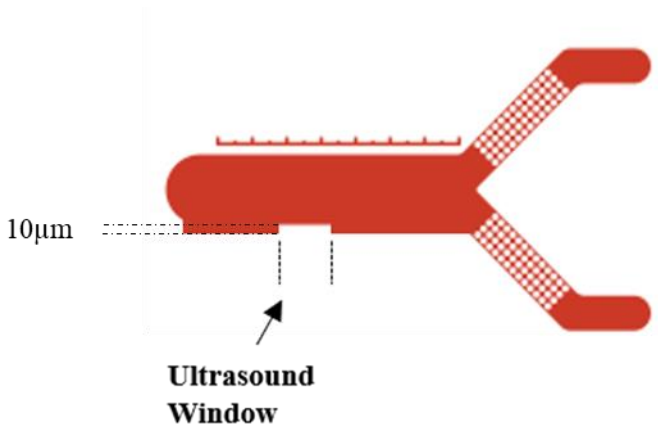

Figure 5-1: *CAD drawing of NOA microfluidic device incorporating an ultrasound window for access to ultrasonic transducer readings; wall thickness ~10µm.*

Once fabricated the methodology for shear rate analysis could be reproduced, while simultaneously performing the ultrasound backscattering methodology developed at LMA. This would allow a direct comparison of ultrasound and optical measurements of RBC aggregates. The NOA device will allow the researchers at LMA to use human blood samples due to the reduced size of the device, thus the reduced requirement of blood. With simultaneous data collection, the ultrasound backscattering technique could be verified using human blood samples and the researchers involved in the study could move forward with development of a medical device capable of characterizing blood aggregation *in vivo*.

References

[1] O. Baskurt, B. Neu, and H. J. Meiselman, *Red Blood Cell Aggregation*, 1st ed. CRC Press, 2019.

[2] M. Thaler *et al.*, "The Role of Blood from HLA-Homozygous Donors in Fatal Transfusion-Associated Graft-versus-Host Disease after Open-Heart Surgery," *N. Engl. J. Med.*, vol. 321, no. 1, pp. 25–28, Jul. 1989, doi: 10.1056/NEJM198907063210105.

[3] M. S. Greenberg and E. H. Kass, "Studies on the Destruction of Red Blood Cells: XIII. Observations on the Role of pH in the Pathogenesis and Treatment of Painful Crisis in Sickle-Cell Disease," *AMA Arch. Intern. Med.*, vol. 101, no. 2, pp. 355–363, Feb. 1958, doi: 10.1001/archinte.1958.00260140187028.

[4] E. Bonora and M. Muggeo, "Postprandial blood glucose as a risk factor for cardiovascular disease in Type II diabetes: the epidemiological evidence," *Diabetologia*, vol. 44, no. 12, pp. 2107–2114, Dec. 2001, doi: 10.1007/s001250100020.

[5] J. Tripette *et al.*, "Red blood cell aggregation, aggregate strength and oxygen transport potential of blood are abnormal in both homozygous sickle cell anemia and sickle-hemoglobin C disease," *Haematologica*, vol. 94, no. 8, pp. 1060–1065, Aug. 2009, doi: 10.3324/haematol.2008.005371.

[6] R. B. Ami *et al.*, "Parameters of red blood cell aggregation as correlates of the inflammatory state," *Am. J. Physiol.-Heart Circ. Physiol.*, vol. 280, no. 5, pp. H1982–H1988, May 2001, doi: 10.1152/ajpheart.2001.280.5.H1982.

[7] H. Schmid-Schönbein, P. Gaehtgens, and H. Hirsch, "On the shear rate dependence of red cell aggregation in vitro," *J. Clin. Invest.*, vol. 47, no. 6, pp. 1447–1454, Jun. 1968, doi: 10.1172/JCI105836.

[8] R. Mehri, C. Mavriplis, and M. Fenech, "Red blood cell aggregates and their effect on non-Newtonian blood viscosity at low hematocrit in a two-fluid low shear rate microfluidic system," *PLoS ONE*, vol. 13, no. 7, pp. 1–26, Jul. 2018, doi: 10.1371/journal.pone.0199911.

[9] R. Mehri, “Red Blood Cell Aggregation Characterization: Quantification and Modeling Implications of Red Blood Cell Aggregation at Low Shear Rates,” Thesis, Université d’Ottawa / University of Ottawa, 2016.

[10] A. H. Gordon, “The acute phase response to injury and infection,” *Res. Monogr. Cell Tissue Physiol.*, vol. 10, 1985, Accessed: Feb. 21, 2020. [Online]. Available: https://ci.nii.ac.jp/naid/10008639154/.

[11] E. Gruys, M. J. M. Toussaint, T. A. Niewold, and S. J. Koopmans, “Acute phase reaction and acute phase proteins,” *J. Zhejiang Univ. Sci. B*, vol. 6, no. 11, pp. 1045–1056, Nov. 2005, doi: 10.1631/jzus.2005.B1045.

[12] B. Almog *et al.*, “Enhanced Erythrocyte Aggregation in Clinically Diagnosed Pelvic Inflammatory Disease,” *Sex. Transm. Dis.*, vol. 32, no. 8, pp. 484–486, Aug. 2005, doi: 10.1097/01.olq.0000161183.43732.53.

[13] N. Lebensohn, A. Re, L. Carrera, L. Barberenna, M. D’Arrigo, and P. Foresto, “Serum sialic acid, cellular anionic charge and erythrocyte aggregation in diabetic and hypertensive patients - Abstract - Europe PMC,” *Medicina*, Dec. 2008, Accessed: Feb. 21, 2020. [Online]. Available: https://europepmc.org/article/med/19622482.

[14] G. Cicco and A. Pirrelli, “Red blood cell (RBC) deformability, RBC aggregability and tissue oxygenation in hypertension,” *Clin. Hemorheol. Microcirc.*, vol. 21, no. 3,4, pp. 169–177, Jan. 1999, Accessed: Feb. 21, 2020. [Online]. Available: https://content.iospress.com/articles/clinical-hemorheology-and-microcirculation/ch231.

[15] R. de Monchy, B. Chayer, G. Cloutier, and E. Franceschini, “Effective Medium Theory combined with a polydisperse Structure Factor Model for characterizing red blood cell aggregation,” in *2016 IEEE International Ultrasonics Symposium (IUS)*, Tours, France, Sep. 2016, pp. 1–4, doi: 10.1109/ULTSYM.2016.7728606.

[16] P. Beard, “Biomedical photoacoustic imaging,” *R. Soc. Publ.*, vol. 1, no. 4, May 2011, doi: https://doi.org/10.1098/rsfs.2011.0028.

[17] D. Sonker, “Photoacoustic signal computation from different erythrocytes,” Thesis, Indian Institute of Information Technology Allahabad, 2018.

[18] K. Chandran, S. Rittgers, and A. Yoganathan, *Biofluid Mechanics The Human Circulation*, 2nd ed. Taylor and Francis Group, 2012.

[19] P. B. Canham and D. R. Parkinson, “The area and volume of single human erythrocytes during gradual osmotic swelling to hemolysis,” *Can. J. Physiol. Pharmacol.*, vol. 48, no. 6, pp. 369–376, Jun. 1970, doi: 10.1139/y70-059.

[20] E. Evans and Y.-C. Fung, “Improved measurements of the erythrocyte geometry,” *Microvasc. Res.*, vol. 4, no. 4, pp. 335–347, Oct. 1972, doi: 10.1016/0026-2862(72)90069-6.

[21] V. Kumar, A. K. Abbas, N. Fausto, and J. C. Aster, *Robbins and Cotran Pathologic Basis of Disease, Professional Edition E-Book*. Elsevier Health Sciences, 2014.

[22] G. J. Brewer and J. W. Eaton, “Erythrocyte Metabolism: Interaction with Oxygen Transport,” *Science*, vol. 171, no. 3977, pp. 1205–1211, Mar. 1971, doi: 10.1126/science.171.3977.1205.

[23] T. C. Page, W. R. Light, C. B. McKay, and J. D. Hellums, “Oxygen Transport by Erythrocyte/Hemoglobin Solution Mixtures in anin VitroCapillary as a Model of Hemoglobin-Based Oxygen Carrier Performance,” *Microvasc. Res.*, vol. 55, no. 1, pp. 54–64, Jan. 1998, doi: 10.1006/mvre.1997.2055.

[24] T. C. Page, W. R. Light, and J. D. Hellums, “Prediction of Microcirculatory Oxygen Transport by Erythrocyte/Hemoglobin Solution Mixtures,” *Microvasc. Res.*, vol. 56, no. 2, pp. 113–126, Sep. 1998, doi: 10.1006/mvre.1998.2088.

[25] N. Mohandas and P. G. Gallagher, “Red cell membrane: past, present, and future,” *ASH Publ.*, vol. 112, no. 10, pp. 3939–3948, Nov. 2008, doi: 10.1182/blood-2008-07-161166.

[26] C. Vera, R. Skelton, F. Bossens, and L. A. Sung, “3-D Nanomechanics of an Erythrocyte Junctional Complex in Equibiaxial and Anisotropic Deformations,” *Ann. Biomed. Eng.*, vol. 33, no. 10, pp. 1387–1404, Oct. 2005, doi: 10.1007/s10439-005-4698-y.

[27] N. Mohandas and P. G. Gallagher, “Red cell membrane: past, present, and future,” *ASH Publ.*, vol. 112, no. 10, Nov. 2008, doi: 10.1182/blood-2008-07-161166.

[28] E. A. Evans and R. M. Hochmuth, “Membrane viscoelasticity,” *Biophysical Journal*, vol. 16, 1976, doi: 10.1016/S0006-3495(76)85658-5.

[29] S. Chien, K. L. Sung, R. Skalak, S. Usami, and A. Tozeren, “Theoretical and experimental studies on viscoelastic properties of erythrocyte membrane.,” *Biophys. J.*, vol. 24, 1978, doi: 10.1016/S0006-3495(78)85395-8.

[30] R. Fåhraeus, “The suspension stability of the blood,” *Physiol. Rev.*, vol. 9, no. 2, pp. 241–274, Apr. 1929, doi: 10.1152/physrev.1929.9.2.241.

[31] M. H. Knisely, “A method of illuminating living structures for microscopic study,” *Anat. Rec.*, vol. 64, no. 4, pp. 499–524, 1936, doi: 10.1002/ar.1090640406.

[32] M. H. Knisely, E. H. Bloch, T. S. Eliot, and L. Warner, “Sludged Blood,” *Science*, vol. 106, no. 2758, pp. 431–440, Nov. 1947, doi: 10.1126/science.106.2758.431.

[33] M. H. Knisely, T. S. Eliot, and E. H. Bloch, “Sludged Blood in Traumatic Shock: I. Microscopic Observations of the precipitation and agglutination of blood flowing through vessels in crushed tissues,” *Arch. Surg.*, vol. 51, no. 4, pp. 220–236, Nov. 1945, doi: 10.1001/archsurg.1945.01230040229002.

[34] M. W. Rampling, H. J. Meiselman, B. Neu, and O. K. Baskurt, “Influence of cell-specific factors on red blood cell aggregation,” *Biorheology*, vol. 41, no. 2, pp. 91–112, Jan. 2004, Accessed: Feb. 24, 2020. [Online]. Available: https://content.iospress.com/articles/biorheology/bir290.

[35] H. Hammi, P. Perrotin, R. Guillet, and M. Boynard, “Determination of red blood cell aggregation in young and elderly subjects evaluated by ultrasound,” *Clin. Hemorheol. Microcirc.*, vol. 14, no. 1, pp. 117–126, Jan. 1994, doi: 10.3233/CH-1994-14115.

[36] E. Piva, M. C. Sanzari, G. Servidio, and M. Plebani, “Length of Sedimentation Reaction in Undiluted Blood (Erythrocyte Sedimentation Rate): Variations with Sex and Age and Reference Limits,” *Clin. Chem. Lab. Med.*, vol. 39, no. 5, pp. 451–454, 2005, doi: 10.1515/CCLM.2001.071.

[37] A. Huisman, J. G. Aarnoudse, M. Krans, H. J. Huisjes, V. Fidler, and W. G. Zijlstra, “Red cell aggregation during normal pregnancy,” *Br. J. Haematol.*, vol. 68, no. 1, pp. 121–124, 1988, doi: 10.1111/j.1365-2141.1988.tb04189.x.

[38] F. C. Mokken, F. J. M. van der Waart, C. P. Henny, P. T. Goedhart, and A. W. Gelb, “Differences in peripheral arterial and venous hemorheologic parameters,” *Ann. Hematol.*, vol. 73, no. 3, pp. 135–137, Sep. 1996, doi: 10.1007/s002770050214.

[39] I. A. Tikhomirova, A. V. Muravyov, and V. N. Levin, “Major alterations in body fluid status and blood rheology,” *Clin. Hemorheol. Microcirc.*, vol. 26, no. 3, pp. 195–198, Jan. 2002, Accessed: Feb. 24, 2020. [Online]. Available: https://content.iospress.com/articles/clinical-hemorheology-and-microcirculation/ch495.

[40] A. Vayá *et al.*, “Menopause, hormone replacement therapy and hemorheology,” *Clin. Hemorheol. Microcirc.*, vol. 30, no. 3,4, pp. 277–281, Jan. 2004, Accessed: Feb. 24, 2020. [Online]. Available: https://content.iospress.com/articles/clinical-hemorheology-and-microcirculation/ch680.

[41] D. E. Brooks, “Mechanism of Red Cell Aggregation,” in *Blood Cells, Rheology, and Aging*, D. Platt, Ed. Berlin, Heidelberg: Springer Berlin Heidelberg, 1988, pp. 158–162.

[42] B. Hans, B. Neu, R. Mitlohner, R. Georgieva, H. J. Meiselman, and H. Kiesewetter, “Electrophoretic and aggregation behavior of bovine, horse and human red blood cells in plasma and in polymer solutions,” *Biorheology*, vol. 38, no. 1, 2001, Accessed: Feb. 08, 2020. [Online]. Available: https://content.iospress.com/articles/biorheology/bir088.

[43] H. Baumler, E. Donath, A. Krabi, W. Knippel, A. Budde, and H. Kiesewetter, “Electrophoresis of human red blood cells and platelets. Evidence for depletion of dextran - ScienceDirect,” *Biorheology*, vol. 33, no. 4–5, 1996, Accessed: Feb. 08, 2020. [Online]. Available: https://doi.org/10.1016/0006-355X(96)00026-1.

[44] O. K. Baskurt, M. R. Hardeman, M. W. Rampling, and H. J. Meiselman, *Handbook of Hemorheology and Hemodynamics*, vol. 69. IOS Press, 2007.

[45] I. Cicha, Y. Suzuki, N. Tateishi, and N. Maeda, “Changes of RBC aggregation in oxygenation-deoxygenation: pH dependency and cell morphology,” *Am. Physiol. Soc.*, vol. 286, no. 6, 2003, Accessed: Feb. 08, 2020. [Online]. Available: https://doi.org/10.1152/ajpheart.01030.2002.

[46] W. H. Reinhart, A. Singh, and P. W. Straub, “Red blood cell aggregation and sedimentation: the role of the cell shape,” *British Journal of Haematology*, vol. 73, no. 4, 1986, Accessed: Feb. 08, 2020. [Online]. Available: https://doi.org/10.1111/j.1365-2141.1989.tb00296.x.

[47] H. J. Meiselman, “Red blood cell aggregation: 45 years being curious,” *Biorheology*, vol. 46, no. 1, 2009, doi: 10.3233/BIR-2009-0522.

[48] R. Agosti, A. Clivati, M. D’Ettorre, F. Ferraini, R. Somazzi, and E. Longhini, “Hematocrit dependence of erythrocyte aggregation,” *IOS Press*, vol. 8, no. 6, 1988, doi: 10.3233/CH-1988-8612.

[49] S. Chien and K. Jan, “Ultrastructural basis of the mechanism of rouleaux formation,” *Microvascular Research*, vol. 5, no. 2, 1973, doi: 10.1016/0026-2862(73)90068-X.

[50] G. Barshtein, T. Ilana, and S. Yedgar, “Red blood cell rouleaux formation in dextran solution: dependence on polymer conformation,” *Eur Biophys J*, vol. 27, 1988, doi: https://doi.org/10.1007/s002490050124.

[51] A. Pribush, D. Zilberman-Kravits, and N. Meyerstein, “The mechanism of the dextran-induced red blood cell aggregation,” *Eur Biophys J*, vol. 36, 2007, doi: https://doi.org/10.1007/s00249-006-0107-1.

[52] B. Neu, R. Wenby, and H. J. Meiselman, “Effects of Dextran Molecular Weight on Red Blood Cell Aggregation,” *Biophysical Journal*, vol. 95, no. 6, 2008, doi: https://doi.org/10.1529/biophysj.108.130328.

[53] J. K. Armstrong, R. B. Wenby, H. J. Meiselman, and T. C. Fisher, “The Hydrodynamic Radii of Macromolecules and Their Effect on Red Blood Cell Aggregation,” *Biophysical Journal*, vol. 87, no. 6, 2004, doi: https://doi.org/10.1529/biophysj.104.047746.

[54] H. J. Meiselman and B. Neu, “Depletion-Mediated Red Blood Cell Aggregation in Polymer Solutions,” *Biophysical Journal*, vol. 83, no. 5, 2002, doi: https://doi.org/10.1016/S0006-3495(02)75259-4.

[55] G. B. Nash, R. B. Wenby, S. O. Sowemimo-Coker, and H. J. Meiselman, “Influence of cellular properties on red cell aggregation,” *Clinical Hemorheology and Microcirculation*, vol. 7, no. 1, 1987, doi: 10.3233/CH-1987-7109.

[56] M. Boynard and J. C. Lelievre, “Size determination of red blood cell aggregates induced by dextran using ultrasound backscattering phenomenon,” *IOS Press*, vol. 27, no. 1, 1990, doi: 10.3233/BIR-1990-27104.

[57] H. L. Goldsmith, “The Microrheology of Red Blood Cell Suspensions,” *Rockefeller Univ. Press*, vol. 52, no. 1, 1968, doi: https://doi.org/10.1085/jgp.52.1.5.

[58] E. Biernacki, “Weitere Beobachtungen über die spontane Blutsedimentirung.,” *Hoppe-Seyler´s Z. Für Physiol. Chem.*, vol. 23, no. 4–5, pp. 368–398, 2009, doi: 10.1515/bchm2.1897.23.4-5.368.

[59] A. Grzybowski and J. Sak, “Edmund Biernacki (1866-1911): Discoverer of the erythrocyte sedimentation rate. On the 100th anniversary of his death,” *Clin. Dermatol.*, vol. 29, no. 6, pp. 697–703, Nov. 2011, doi: 10.1016/j.clindermatol.2011.08.033.

[60] R. Fahraeus, “The Suspernsion stability of the blood,” *Am. Physiol. Soc.*, vol. 19, no. 2, 1929, doi: https://doi.org/10.1152/physrev.1929.9.2.241.

[61] C. S. Crowson, M. U. Rahman, and E. L. Matteson, “Which Measure of Inflammation to Use? A Comparison of Erythrocyte Sedimentation Rate and C-Reactive Protein Measurements from Randomized Clinical Trials of Golimumab in Rheumatoid Arthritis,” *J. Rheumatol.*, vol. 36, no. 8, pp. 1606–1610, Aug. 2009, doi: 10.3899/jrheum.081188.

[62] S. B. Menees, C. Powell, J. Kurlander, A. Goel, and W. D. Chey, “A Meta-Analysis of the Utility of C-Reactive Protein, Erythrocyte Sedimentation Rate, Fecal Calprotectin, and Fecal Lactoferrin to Exclude Inflammatory Bowel Disease in Adults With IBS,” *Am. J. Gastroenterol.*, vol. 110, no. 3, pp. 444–454, Mar. 2015, doi: 10.1038/ajg.2015.6.

[63] S. Chien and K. Jan, “Ultrastructural basis of the mechanism of rouleaux formation,” *Microvasc. Res.*, vol. 5, no. 2, pp. 155–166, Mar. 1973, doi: 10.1016/0026-2862(73)90068-X.

[64] J. Engeset, D. Dhall, and N. Matheson, “Measurement of red cell aggregation and dispersion.,” *Bibl. Anat.*, vol. 10, pp. 80–84, Jan. 1969, Accessed: Feb. 24, 2020. [Online]. Available: https://europepmc.org/article/med/5407425.

[65] R. Mehri, E. Niazi, C. Mavriplis, and M. Fenech, “An automated method for dynamic red blood cell aggregate detection in microfluidic flow,” *Physiol. Meas.*, vol. 39, no. 1, p. 01NT02, Jan. 2018, doi: 10.1088/1361-6579/aaa0ad.

[66] E. Niazi, J. G. McDonald, and M. Fenech, “An automated method for size and velocity distribution measurement in a particle-laden flow,” *Adv. Eng. Softw.*, vol. 134, pp. 10–21, Aug. 2019, doi: 10.1016/j.advengsoft.2019.05.002.

[67] J. Mamou and M. L. Oelze, *Quantitative Ultrasound in Soft Tissues*. Springer, Dordrecht, 2013.

[68] J. W. S. Rayleigh, *The Theory of Sound*, 2nd ed., vol. 2. Dover, 1945.

[69] K. T. Dussik, “The possibility of using high-frequency mechanical vibrations as a diagnostic tool,” *Journal of Entire Neurology and Psychiatry*, vol. 174, 1942, doi: https://doi.org/10.1007/BF02877929.

[70] V. Chan and A. Perlas, *Basics of Ultrasound Imaging*. New York: Springer, 2010.

[71] K. T. Dussik *et al.*, “Measurements of Articular tissue with ultrasound,” *PubMed*, vol. 37, no. 3, 1958, Accessed: Feb. 20, 2020. [Online]. Available: https://journals.lww.com/ajpmr/Citation/1958/06000/Measurements_of_Articular_Tissues_With_Ultrasound.13.aspx.

[72] F. A. Firestone, “Flaw detecting device and measuring instrument,” US2280226A, Apr. 21, 1942.

[73] F. A. Firestone, “Measuring thickness of dielectric materials,” US2285152A, Jun. 02, 1942.

[74] F. A. Firestone and J. R. Frederick, “Refinements in Supersonic Reflectoscopy. Polarized Sound,” *ASA Publ.*, vol. 18, no. 1, 1946, doi: https://doi.org/10.1121/1.1916359.

[75] V. Twersky, “Low-frequency scattering by correlated distributions of randomly oriented particles,” *ASA Publ.*, vol. 81, no. 5, 1987, doi: https://doi.org/10.1121/1.394513.

[76] D. Savery and G. Cloutier, “A point process approach to assess the frequency dependence of ultrasound backscattering by aggregating red blood cells,” *ASA Publ.*, vol. 110, no. 6, 2001, doi: https://doi.org/10.1121/1.1419092.

[77] G. T. Kuster and M. N. Toksoz, “Velocity and Attenuation of seismic waves in two-phase media: Part I. Theroretical Formulations,” *Soc. Explor. Geophys.*, vol. 39, no. 5, 1974, doi: https://doi.org/10.1190/1.1440450.

[78] G. T. Kuster and M. N. Toksoz, “Velocity and Attenuation of seismic waves in two-phase media: Part II. Experimental Results,” *Soc. Explor. Geophys.*, vol. 39, no. 5, 1974, doi: https://doi.org/10.1190/1.1440451.

[79] E. Franceschini, B. Metzger, and G. Cloutier, “Forward Problem Study of an Effective Medium Model for Ultrasound Blood Characterization,” *IEEE Transactions on Ultrasonics, Ferroelectrics, and Frequency Control*, vol. 58, no. 12, 2011, doi: 10.1109/TUFFC.2011.2129.

[80] E. Franceschini, R. K. Saha, and G. Cloutier, “Comparison of three scattering models for ultrasound blood characterization,” *IEEE Transactions on Ultrasonics, Ferroelectrics, and Frequency Control*, vol. 60, no. 11, 2013, doi: 10.1109/TUFFC.2013.6644736.

[81] E. Franceschini, F. T. H. Yu, and G. Cloutier, “Simultaneous estimation of attenuation and structure parameters of aggregated red blood cells from backscatter measurements,” *J. Acoust. Soc. Am.*, vol. 123, no. 4, pp. EL85–EL91, Mar. 2008, doi: 10.1121/1.2896115.

[82] E. Franceschini, F. T. H. Yu, F. Destrempes, and G. Cloutier, “Ultrasound characterization of red blood cell aggregation with intervening attenuating tissue-mimicking phantoms,” *J. Acoust. Soc. Am.*, vol. 127, no. 2, pp. 1104–1115, Feb. 2010, doi: 10.1121/1.3277200.

[83] M. I. Mohammed, S. Haswell, and I. Gibson, “Lab-on-a-chip or Chip-in-a-lab: Challenges of Commercialization Lost in Translation,” *Procedia Technol.*, vol. 20, pp. 54–59, Jan. 2015, doi: 10.1016/j.protcy.2015.07.010.

[84] T. Bayraktar and S. B. Pidugu, “Characterization of liquid flows in microfluidic systems,” *Int. J. Heat Mass Transf.*, vol. 49, no. 5, pp. 815–824, Mar. 2006, doi: 10.1016/j.ijheatmasstransfer.2005.11.007.

[85] A. Günther and K. F. Jensen, “Multiphase microfluidics: from flow characteristics to chemical and materials synthesis,” *Lab. Chip*, vol. 6, no. 12, pp. 1487–1503, Nov. 2006, doi: 10.1039/B609851G.

[86] J. J. Bishop, A. S. Popel, M. Intaglietta, and P. C. Johnson, “Effect of aggregation and shear rate on the dispersion of red blood cells flowing in venules,” *Am. J. Physiol.-Heart Circ. Physiol.*, vol. 283, no. 5, pp. H1985–H1996, Nov. 2002, doi: 10.1152/ajpheart.00888.2001.

[87] J. J. Bishop, A. S. Popel, M. Intaglietta, and P. C. Johnson, “Effects of erythrocyte aggregation and venous network geometry on red blood cell axial migration,” *Am. J. Physiol.-Heart Circ. Physiol.*, vol. 281, no. 2, pp. H939–H950, Aug. 2001, doi: 10.1152/ajpheart.2001.281.2.H939.

[88] J. J. Bishop, P. R. Nance, A. S. Popel, M. Intaglietta, and P. C. Johnson, “Relationship between erythrocyte aggregate size and flow rate in skeletal muscle venules,” *Am. J. Physiol.-Heart Circ. Physiol.*, vol. 286, no. 1, pp. H113–H120, Jan. 2004, doi: 10.1152/ajpheart.00587.2003.

[89] E. Kaliviotis, J. Dusting, and S. Balabani, “Spatial variation of blood viscosity: Modelling using shear fields measured by a μPIV based technique,” *Med. Eng. Phys.*, vol. 33, no. 7, pp. 824–831, Sep. 2011, doi: 10.1016/j.medengphy.2010.09.004.

[90] R. Mehri, C. Mavriplis, and M. Fenech, “Controlled Microfluidic Environment for Dynamic Investigation of Red Blood Cell Aggregation,” *JoVE J. Vis. Exp.*, no. 100, p. e52719, Jun. 2015, doi: 10.3791/52719.

[91] R. Mehri, “Micro PIV and numerical investigation of a micro-Couette blood flow,” M.A.Sc., University of Ottawa (Canada), Canada, 2012.

[92] R. Mehri, J. Laplante, C. Mavriplis, and M. Fenech, “Blood Flow Analysis and Red Blood Cell Aggregation Investigation,” *CMBES Proc.*, vol. 36, May 2013, Accessed: Feb. 18, 2020. [Online]. Available: https://proceedings.cmbes.ca/index.php/proceedings/article/view/381.

[93] J. C. McDonald and G. M. Whitesides, “Poly(dimethylsiloxane) as a material for fabricating microfluidic devices,” *Acc. Chem. Res.*, vol. 35, no. 7, pp. 491–499, Jul. 2002.

[94] M. W. Toepke and D. J. Beebe, “PDMS absorption of small molecules and consequences in microfluidic applications,” *Lab. Chip*, vol. 6, no. 12, pp. 1484–1486, Nov. 2006, doi: 10.1039/B612140C.

[95] B. S. Hardy, K. Uechi, J. Zhen, and H. P. Kavehpour, “The deformation of flexible PDMS microchannels under a pressure driven flow,” *Lab. Chip*, vol. 9, no. 7, pp. 935–938, Apr. 2009, doi: 10.1039/B813061B.

[96] T. Gervais, J. El-Ali, A. Günther, and K. F. Jensen, “Flow-induced deformation of shallow microfluidic channels,” *Lab. Chip*, vol. 6, no. 4, pp. 500–507, Apr. 2006, doi: 10.1039/b513524a.

[97] K. S. Lee and R. J. Ram, “Plastic–PDMS bonding for high pressure hydrolytically stable active microfluidics,” *Lab. Chip*, vol. 9, no. 11, pp. 1618–1624, 2009, doi: 10.1039/B820924C.

[98] M. Liu, J. Sun, Y. Sun, C. Bock, and Q. Chen, “Thickness-dependent mechanical properties of polydimethylsiloxane membranes,” *J. Micromechanics Microengineering*, vol. 19, no. 3, p. 035028, Feb. 2009, doi: 10.1088/0960-1317/19/3/035028.

[99] J. H. Sim, H. J. Moon, Y. H. Roh, H. W. Jung, and K. W. Bong, “Fabrication of NOA microfluidic devices based on sequential replica molding,” *Korean J. Chem. Eng.*, vol. 34, no. 5, pp. 1495–1499, May 2017, doi: 10.1007/s11814-017-0041-1.

[100] E. P. Dupont, R. Luisier, and M. A. M. Gijs, “NOA 63 as a UV-curable material for fabrication of microfluidic channels with native hydrophilicity,” *Microelectron. Eng.*, vol. 87, no. 5, pp. 1253–1255, May 2010, doi: 10.1016/j.mee.2009.11.084.

[101] S. H. Kim *et al.*, “Simple Route to Hydrophilic Microfluidic Chip Fabrication Using an Ultraviolet (UV)-Cured Polymer,” *Adv. Funct. Mater.*, vol. 17, no. 17, pp. 3493–3498, 2007, doi: 10.1002/adfm.200601203.

[102] E. Sollier, C. Murray, P. Maoddi, and D. D. Carlo, “Rapid prototyping polymers for microfluidic devices and high pressure injections,” *Lab. Chip*, vol. 11, no. 22, pp. 3752–3765, Oct. 2011, doi: 10.1039/C1LC20514E.

[103] D. Bartolo, G. Degré, P. Nghe, and V. Studer, “Microfluidic stickers,” *Lab. Chip*, vol. 8, no. 2, pp. 274–279, 2008, doi: 10.1039/B712368J.

[104] Ph. Wägli, A. Homsy, and N. F. de Rooij, “Norland optical adhesive (NOA81) microchannels with adjustable wetting behavior and high chemical resistance against a range of mid-infrared-transparent organic solvents,” *Sens. Actuators B Chem.*, vol. 156, no. 2, pp. 994–1001, Aug. 2011, doi: 10.1016/j.snb.2011.02.005.

[105] P. Wägli, A. Homsy, and N. F. de Rooij, “Norland optical adhesive (NOA81) microchannels with adjustable surface properties and high chemical resistance against IR-transparent organic solvents,” *Procedia Eng.*, vol. 5, pp. 460–463, Jan. 2010, doi: 10.1016/j.proeng.2010.09.146.

[106] C. Willert and J. Kompenhans, “PIV Analysis of Ludwig Prandtl’s Historic Flow Visualization Films,” *Phys. Fluids*, Oct. 2010, Accessed: Feb. 24, 2020. [Online]. Available: http://arxiv.org/abs/1010.3149.

[107] B. Wieneke, “PIV uncertainty quantification from correlation statistics,” *Meas. Sci. Technol.*, vol. 26, no. 7, p. 074002, Jun. 2015, doi: 10.1088/0957-0233/26/7/074002.

[108] R. D. Keane and R. J. Adrian, “Theory of cross-correlation analysis of PIV images,” *Appl. Sci. Res.*, vol. 49, no. 3, pp. 191–215, Jul. 1992, doi: 10.1007/BF00384623.

[109] R. J. Adrian, “Twenty years of particle image velocimetry,” *Exp. Fluids*, vol. 39, no. 2, pp. 159–169, Aug. 2005, doi: 10.1007/s00348-005-0991-7.

[110] M. Raffel, C. E. Willert, F. Scarano, C. J. Kähler, S. T. Wereley, and J. Kompenhans, *Particle Image Velocimetry: A Practical Guide*. 2018.

[111] S. Wereley, C. Meinhart, and J. Santiago, “Microfluidic PIV: Algorithms and Experiments,” p. AC.04, Nov. 1998, Accessed: Feb. 19, 2020. [Online]. Available: http://adsabs.harvard.edu/abs/1998APS..DFD..AC04W.

[112] C. D. Meinhart, S. T. Wereley, and M. H. B. Gray, “Volume illumination for two-dimensional particle image velocimetry,” 2000, doi: 10.1088/0957-0233/11/6/326.

[113] J. G. Santiago, S. T. Wereley, C. D. Meinhart, D. J. Beebe, and R. J. Adrian, “A particle image velocimetry system for microfluidics,” 1998, doi: 10.1007/s003480050235.

[114] L. Bitsch, L. H. Olesen, C. H. Westergaard, H. Bruus, H. Klank, and J. P. Kutter, “Micro particle-image velocimetry of bead suspensions and blood flows,” *Exp. Fluids*, vol. 39, no. 3, pp. 507–513, Sep. 2005, doi: 10.1007/s00348-005-0967-7.

[115] M. G. Olsen and R. J. Adrian, “Brownian motion and correlation in particle image velocimetry,” *Opt. Laser Technol.*, vol. 32, no. 7, pp. 621–627, Oct. 2000, doi: 10.1016/S0030-3992(00)00119-5.

[116] K. L. Pitts and M. Fenech, “Micro-particle Image Velocimetry for Velocity Profile Measurements of Micro Blood Flows,” *J. Vis. Exp. JoVE*, no. 74, Apr. 2013, doi: 10.3791/50314.

[117] Y. Sugii, S. Nishio, and K. Okamoto, “PIV Measurement of Red Blood Cell Velocity Field in Microvessels,” *J. Vis. Inf. Soc.*, vol. 22, no. 1Supplement, pp. 25–28, 2002, doi: 10.3154/jvs.22.1Supplement_25.

[118] A. Nakano, Y. Sugii, M. Minamiyama, and H. Niimi, “Measurement of red cell velocity in microvessels using particle image velocimetry (PIV),” *Clin. Hemorheol. Microcirc.*, vol. 29, no. 3,4, pp. 445–455, Jan. 2003, Accessed: Feb. 19, 2020. [Online]. Available: https://content.iospress.com/articles/clinical-hemorheology-and-microcirculation/ch623.

[119] Y. Sugii, R. Okuda, K. Okamoto, and H. Madarame, “Velocity measurement of both red blood cells and plasma ofin vitroblood flow using high-speed micro PIV technique,” *Meas. Sci. Technol.*, vol. 16, no. 5, pp. 1126–1130, Mar. 2005, doi: 10.1088/0957-0233/16/5/011.

[120] Y. Sugii and K. Okamoto, “Quantitative visualization of micro-tube flow using micro-PIV,” *J. Vis.*, vol. 7, no. 1, pp. 9–16, Mar. 2004, doi: 10.1007/BF03181480.

[121] L. Bitsch, “Micro PIV on blood flow in a microchannel,” *Proc. Seventh Int. Conf. Miniaturized Chem. Biochem. Anal. Syst. Mtas 2003*, pp. 825–828, 2003.

[122] "Rheological and velocity profile measurements of blood in microflow using micro-particle image velocimetry - ProQuest." https://search.proquest.com/docview/1354473495?pq-origsite=gscholar (accessed Feb. 21, 2020).

[123] K. L. Pitts and M. Fenech, "An Analytic Study on the Effect of Alginate on the Velocity Profiles of Blood in Rectangular Microchannels Using Microparticle Image Velocimetry," *NCBI*, vol. 8, no. 8, 2013, doi: 10.1371/journal.pone.0072909.

[124] R. Mehri, E. Niazi, C. Mavriplis, and M. Fenech, "An automated method for dynamic red blood cell aggregate detection in microfluidic flow," *Physiol. Meas.*, vol. 39, no. 1, p. 01NT02, Jan. 2018, doi: 10.1088/1361-6579/aaa0ad.

[125] R. de Monchy, J. Rouyer, F. Destrempes, B. Chayer, G. Cloutier, and E. Franceschini, "Estimation of polydispersity in aggregating red blood cells by quantitative ultrasound backscatter analysis," *J. Acoust. Soc. Am.*, vol. 143, no. 4, pp. 2207–2216, Apr. 2018, doi: 10.1121/1.5031121.

[126] K. Khanafer, A. Duprey, M. Schlicht, and R. Berguer, "Effects of strain rate, mixing ratio, and stress–strain definition on the mechanical behavior of the polydimethylsiloxane (PDMS) material as related to its biological applications," *Biomed. Microdevices*, vol. 11, no. 2, p. 503, Dec. 2008, doi: 10.1007/s10544-008-9256-6.

[127] X. Ye, H. Liu, Y. Ding, H. Li, and B. Lu, "Research on the cast molding process for high quality PDMS molds," *Microelectron. Eng.*, vol. 86, no. 3, pp. 310–313, Mar. 2009, doi: 10.1016/j.mee.2008.10.011.

[128] I. D. Johnston, D. K. McCluskey, C. K. L. Tan, and M. C. Tracey, "Mechanical characterization of bulk Sylgard 184 for microfluidics and microengineering," *J. Micromechanics Microengineering*, vol. 24, no. 3, p. 035017, Feb. 2014, doi: 10.1088/0960-1317/24/3/035017.

[129] G. Zhuang and J. P. Kutter, "Anti-stiction coating of PDMS moulds for rapid microchannel fabrication by double replica moulding," *J. Micromechanics Microengineering*, vol. 21, no. 10, p. 105020, Sep. 2011, doi: 10.1088/0960-1317/21/10/105020.

[130] S. Tavoularis, *Measurement in Fluid Mechanics*. Cambridge University Press, 2005.

[131] H. J. Meiselman and B. Neu, “Depletion-Mediated Red Blood Cell Aggregation in Polymer Solutions,” *Biophysical Journal*, vol. 83, no. 5, 2002, doi: https://doi.org/10.1016/S0006-3495(02)75259-4.

[132] J. Kim, J. F. Antaki, and M. Massoudi, “Computational study of blood flow in microchannels,” *Journal of Computational and Applied Mathmatics*, vol. 292, 2016, doi: https://doi.org/10.1016/j.cam.2015.06.017.

[133] H. L. Goldsmith, “The Microrheology of Red Blood Cell Suspensions,” *J. Gen. Physiol.*, vol. 52, no. 1, pp. 5–28, Jul. 1968, doi: 10.1085/jgp.52.1.5.

[134] H. L. Goldsmith, J. Marlow, and F. C. MacIntosh, “Flow behaviour of erythrocytes - I. Rotation and deformation in dilute suspensions,” *Proc. R. Soc. Lond. B Biol. Sci.*, vol. 182, no. 1068, pp. 351–384, Oct. 1972, doi: 10.1098/rspb.1972.0084.

[135] C. Minetti, V. Audemar, T. Podgorski, and G. Coupier, “Dynamics of a large population of red blood cells under shear flow,” *J. Fluid Mech.*, vol. 864, pp. 408–448, Apr. 2019, doi: 10.1017/jfm.2019.42.

[136] S. Xie, J. Wu, B. Tang, G. Zhou, M. Jin, and L. Shui, “Large-Area and High-Throughput PDMS Microfluidic Chip Fabrication Assisted by Vacuum Airbag Laminator,” *Micromachines*, vol. 8, no. 7, Jul. 2017, doi: 10.3390/mi8070218.

[137] C. Roh, J. Lee, and C. Kang, “The Deformation of Polydimethylsiloxane (PDMS) Microfluidic Channels Filled with Embedded Circular Obstacles under Certain Circumstances,” *Molecules*, vol. 21, no. 6, Jun. 2016, doi: 10.3390/molecules21060798.

[138] C. Kang, C. Roh, and R. A. Overfelt, “Pressure-driven deformation with soft polydimethylsiloxane (PDMS) by a regular syringe pump: challenge to the classical fluid dynamics by comparison of experimental and theoretical results,” *RSC Adv.*, vol. 4, no. 7, pp. 3102–3112, Dec. 2013, doi: 10.1039/C3RA46708B.

[139] Z. Li, S. Y. Mak, A. Sauret, and H. C. Shum, “Syringe-pump-induced fluctuation in all-aqueous microfluidic system implications for flow rate accuracy,” *Lab. Chip*, vol. 14, no. 4, pp. 744–749, Jan. 2014, doi: 10.1039/C3LC51176F.

[140] W. Zeng, S. Li, and Z. Wang, “Characterization of syringe-pump-driven versus pressure-driven microfluidic flows,” in *2015 International Conference on Fluid Power and Mechatronics (FPM)*, Aug. 2015, pp. 711–715, doi: 10.1109/FPM.2015.7337207.

[141] O. R. Gliah, “In Vitro Investigation of Cell-Free Layer Formation in Microchannels: Dependency on the Red Blood Cell Aggregation and Field of Shear,” Thesis, Université d’Ottawa / University of Ottawa, 2018.

[142] P. K. Ong, B. Namgung, P. C. Johnson, and S. Kim, “Effect of erythrocyte aggregation and flow rate on cell-free layer formation in arterioles,” *Am. J. Physiol.-Heart Circ. Physiol.*, vol. 298, no. 6, pp. H1870–H1878, Jun. 2010, doi: 10.1152/ajpheart.01182.2009.

[143] D. Flormann, K. Schirra, T. Podgorski, and C. Wagner, “On the rheology of red blood cell suspensions with different amounts of dextran: separating the effect of aggregation and increase in viscosity of the suspending phase,” *Rheol. Acta*, vol. 55, no. 6, pp. 477–483, Jun. 2016, doi: 10.1007/s00397-015-0882-7.